THE UNIVERSITY OF CHICAGO

USING HIGGS BOSON TO SEARCH FOR DARK MATTER WITH THE ATLAS DETECTOR

A DISSERTATION SUBMITTED TO
THE FACULTY OF THE DIVISION OF THE PHYSICAL SCIENCES
IN CANDIDACY FOR THE DEGREE OF
DOCTOR OF PHILOSOPHY

DEPARTMENT OF PHYSICS

BY
RUI ZOU

CHICAGO, ILLINOIS
MARCH 2020

To my parents for giving me the freedom of choice.

致我的父母感谢他们给予我自由选择人生的能力和权利。

If I could remember the names of all these particles, I'd be a botanist.

— Enrico Fermi

TABLE OF CONTENTS

LIST OF FIGURES

*Unless otherwise noted, all figures in this thesis are the author's own work.

LIST OF TABLES

ACKNOWLEDGMENTS

I would like to thank my advisor, Young-Kee Kim, for the tremendous amount of support and valuable advice. You are the best role model that I will always look up to. I would also like to thank Mel Shochet for great mentorship throughout my time on FTK.

Thank you to Doug Schaefer for teaching me your brilliant ideas and leading me to the success of my thesis project. Thank you to Ben Carlson for mentoring me and working with me on VBF H→Invisible and development of a new MET trigger. Thank you to Jamie Saxon for helping me get into FTK and track fitting and introducing me to H→Invisible.

I also want to thank all my friends that supported and encouraged me throughout my PhD journey. Thank you Max and Tova for mentoring and taking care of me at CERN. Thank you to all the current and former UChicago crew. Thank you to the whole VBF H→Invisible team and the FTK team for being such supportive teams. I have had a great pleasure to work with all of you and hope to see a lot of you again at CERN.

And to Mark. You make me happy. I love you.

ABSTRACT

This thesis presents a search for the Higgs boson decaying into invisible particles, such as dark matter particles, using proton-proton collision data. Although the invisible decay channel is very small in the Standard Model of particle physics (SM), it is highly motivated by some of new physics models including Higgs portal dark matter models. In addition, the present experimental measurements of Higgs boson decays allow non-SM decays as large as O(30%). The data for this thesis were collected with the ATLAS detector at the LHC in 2015-2016 at a center-of-mass energy of 13 TeV, corresponding to an integrated luminosity of 36.1 fb^{-1}. The search uses the production of a Higgs boson via the vector boson fusion mode, which has the second largest cross section among Higgs boson production processes and drives the sensitivity for this search thus far. The data are found to be in agreement with the background contributions from SM processes. The first analysis places an observed (expected) upper limit of 0.37 (0.28), at 95% confidence level, on the branching fraction of the Higgs boson decay to invisible particles, assuming a Higgs boson mass of 125 GeV. It is also interpreted in the context of Higgs portal dark matter models and compared to direct dark matter searches. After the publication of this result, a second analysis was performed with significant improvements, resulting in an observed (expected) upper limit of 0.20 (0.20), at 95% confidence level, on the branching fraction of the Higgs boson decay to invisible particles.

CHAPTER 1

INTRODUCTION

The Standard Model of particle physics describes three of the four known forces with high precision. It has been shown to accurately predict particle interactions at high energies in particle colliders. In 2012, the Higgs Boson, a central particle to the theory and the only fundamental particle yet to be observed, was found at the Large Hadron Collider. The Higgs Boson is a scalar particle that breaks electroweak symmetry and gives mass to the elementary particles. Its discovery raised many questions around its properties such as the hierarchy problem: why Higgs mass is found to be at 125 GeV, orders of magnitudes lower than the Plank scale. Since the discovery in 2012, major decay modes of Higgs have been explored and constantly updated. The most recent results combined put a constraint on the Higgs decay width at O(30%).

Since the Standard Model has been successful describing ordinary matter it is well motivated to think that Dark Matter is composed of particles. Since the Higgs field couples to fermion masses through Yukawa couplings and corrections to the Higgs self-coupling are needed, it seems plausible that the Higgs field also couples to the mass of Dark Matter particles. Although Dark Matter particles are invisible to the detectors at the LHC, it is possible to search for such a coupling using momentum conservation in the plane transverse to the beam line. Such a search is called a search for Higgs to Invisible particles. Searches for Higgs to Invisible were performed in three of the four Higgs production modes in the first run (2009-2013) of the LHC [20, 37, 29]. The most sensitive search was the Vector Boson Fusion (VBF) production mode.

In 2015, after a three-year shutdown, the LHC nearly doubled the center-of-mass energy of its collisions. This allowed possibilities to improve the sensitivity of the search but also brings in new challenges for analyzers as the Standard Model backgrounds are increased. This thesis presents the search of VBF Higgs to Invisible using the first set of ATLAS Run 2 data (36.1 fb^{-1}) [38] and a reoptimized search using the same dataset.

This thesis is organized as the following. Chapter 2 gives a brief overview of our current theoretical understanding of the relevant physics. Chapter 3 describes the experimental setup used to gather the data, including the LHC and the ATLAS detectors and triggers. Chapter 4 describes the first analysis, including the overall strategy, methods used to reconstruct the various objects produced in LHC collisions, modeling the signal, understanding the backgrounds, event selection criteria, background estimates, systematic uncertainties, and results. The re-optimized analysis is presented in Chapter 5. This thesis ends with a conclusive summary and presents an outlook for future searches in Chapter 6.

CHAPTER 2

THEORETICAL BACKGROUND

2.1 Standard Model

The Standard Model has been developed over a number of decades and detailed descriptions have long been available [54, 49]. This is a brief account of few details needed to motivate this work.

The Standard Model (SM) is a theoretical framework that describes the elementary particles and three of the four fundamental forces (strong, electromagnetism, weak, and gravitational) by which they interact with each other. The three fundamental forces in SM describe all natural phenomena besides gravity. Electromagnetism describes the the interaction of electrons with the nuclei. The strong force describes the interactions within the nucleus. The weak force describes radioactivity and nuclear fusion. The SM uses a math formalism known as the quantum field theory. The fundamental particles are states of quantized fields in quantum field theory. Matter is constituted by quarks and leptons, both with fields of half integer spin, and referred to as fermionic fields. There are three generations of quarks and leptons, each with a left-handed doublet and two right-handed singlets:

$$\begin{pmatrix} u \\ d \end{pmatrix}_L, u_R, d_R \text{ and } \begin{pmatrix} \nu \\ e^- \end{pmatrix}_L, e_R^-, \nu_R \tag{2.1}$$

Figure 2.1 lists all the fermions that constitute matter and the force carrier bosons. The SM Lagrangian is invariant under local transformations of the gauge group $SU(3)_c \times SU(2)_L \times U(1)_Y$, where c is color, L is the left-handedness of the $SU(2)$ coupling and Y is the weak hypercharge. This is referred to as gauge invariance and is crucial to renormalizability of the theory, which is necessary for consistency. Local gauge invariance is preserved through the introduction of additional quantum fields, known as spin one gauge fields. The excitations of the gauge fields correspond to particles known as gauge bosons. There are twelve gauge

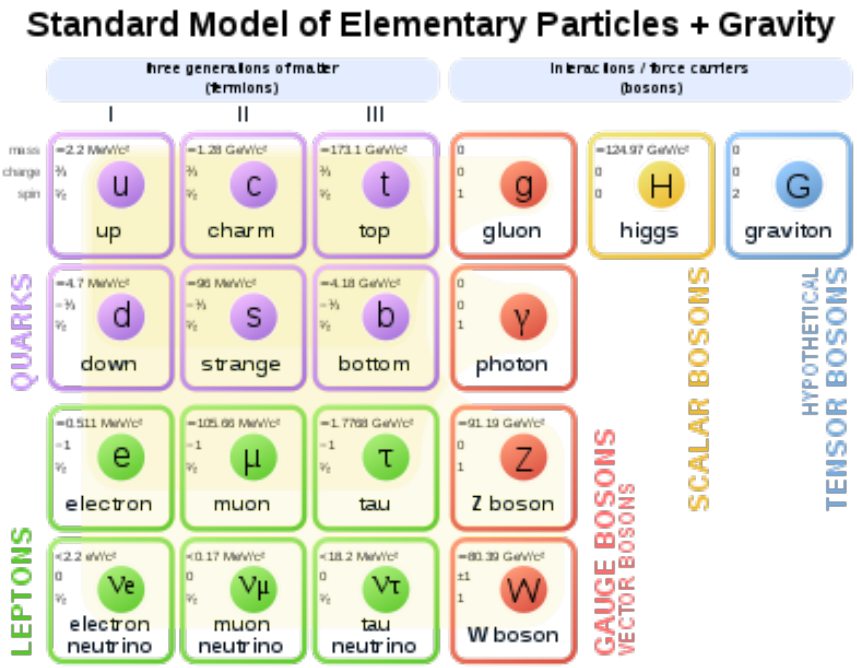

Figure 2.1: Table of fundamental particles in the SM.

fields in the SM, eight for the generators of $SU(3)$, three for the generators of $SU(2)$, and one for the generator of $U(1)$. This corresponds to an octet of colored gluons, $W^{\pm}$ and Z^0 bosons and the photon, respectively.

While the $SU(3)$ gauge symmetry correctly describes the strong interactions, the part of the SM governed by the $SU(2) \times U(1)$ symmetry has a problem. The gauge bosons have to be massless in order to preserve gauge invariance just like the gluons. However, the $W^{\pm}$ and Z^0 bosons have large masses, seemingly contradictory to the prediction. Another problem is the masses of the quarks and leptons. The weak interaction violates parity and the left and right-handed fermions are treated differently in SM. Gauge invariance would imply that the fermions should be massless as well, which again is contradictory to observations.

These problems are solved by adding additional quantum field to couple to the $SU(2) \times U(1)$ gauge fields, known as spontaneous symmetry breaking. The additional field is a scalar field. In order for it to be included in a way that preserves the gauge invariance and respects the symmetry, it is added so that the zero values of the field is not the lowest

energy state. Thus, the Lagrangian preserves gauge invariance while the particular state is not $SU(2) \times U(1)$ symmetric. Thus this symmetry is spontaneously broken.

One of the consequences of the spontaneous symmetry breaking is the prediction of a massive scalar particle. This field should be a neutral massive scalar boson, known as the Higgs boson. The mass of the Higgs boson depends on an arbitrary parameter associated to the symmetry breaking and is thus unpredictable. The couplings to gauge bosons are fixed by the gauge couplings, and the couplings to fermions are fixed by the fermion masses; the Higgs boson couples to fermions proportionally to their mass. Gauge couplings and fermion masses are constrained by measurements which determine the interactions between fundamental particles and the Higgs boson within the SM. The Higgs boson has been observed experimentally by the ATLAS and CMS experiments at the LHC in 2012. A more detailed description of the mechanism is in Section 2.2.

While the discovery of the Higgs boson adds another item in the long list of successful predictions by the SM. There are lots of fundamental questions the SM cannot answer. The hierarchy problem, for example, arises as we found the Higgs at a mass of 125 GeV. The quantum corrections to the Higgs mass should make the mass inevitably huge unless there is some fine-tuned cancellations between the corrections and the bare mass, which seems unnatural. The free parameters in the model that are only known from measurements, such as the particle masses, also invite questions on the origins of their values or relationships among them. SM is not capable of explaining all the natural phenomena either. Explanation for phenomena such as the nonzero neutrino masses observed from neutrino oscillation experiments or Dark Matter which is strongly suggested by cosmological observations (see Section 2.4 for details) are completely missing. Additions to the SM theory can be made to address some of the issues such as more complex arrangements of scalar fields or additional particles such as Dark Matter particles.

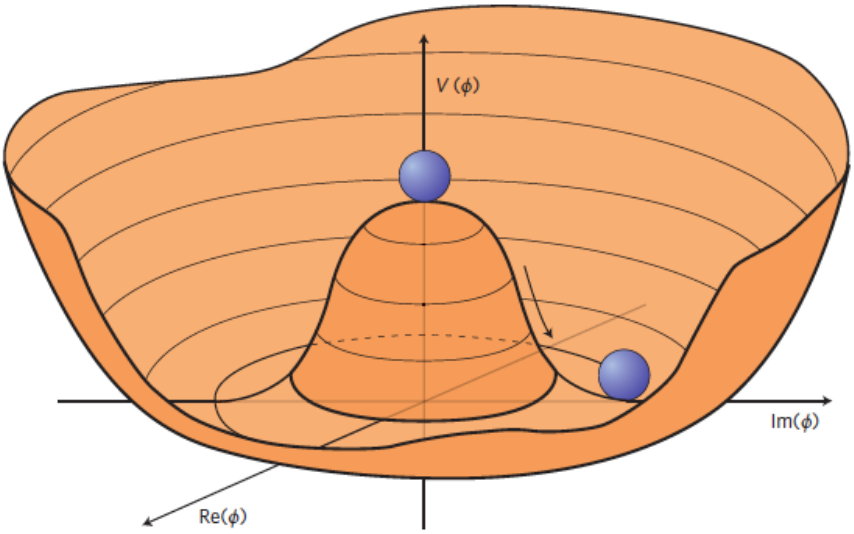

Figure 2.2: The Higgs potential $V(\Phi)$ illustration where $\lambda > 0$ and $\mu^2 < 0$. Any point at the bottom of the potential spontaneously breaks the U(1) symmetry.

2.2 Higgs Mechanism

The SM Lagrangian may be separated into four parts

$$\mathcal{L}_{\text{SM}} = \mathcal{L}_{\text{gauge}} + \mathcal{L}_f + \mathcal{L}_\Phi + \mathcal{L}_{\text{Yukawa}}. \tag{2.2}$$

L_{gauge} describes the kinetic energies and interactions of the gauge bosons. L_f describes the kinetic energies of the fermions and their interactions with the gauge bosons. L_Φ describes the kinetic energies and potential of the Higgs field. L_{Yukawa} describe the interactions between the Higgs field and the fermions.

To preserve gauge invariance, we introduce a doublet of complex scalar fields Φ. Associate it with the invariant scalar potential under $SU(2) \times U(1)$:

$$V(\Phi) = \mu^2 \Phi^\dagger \Phi + \lambda (\Phi^\dagger \Phi)^2. \tag{2.3}$$

When $\lambda > 0$ and $\mu^2 < 0$, the minimum of the potential $V(\Phi)$ is $\nu = \sqrt{-\mu^2/\lambda}$, which is known as the non-zero vacuum expectation value (vev). An illustration of $V(\Phi)$ is shown in

Figure 2.2.

$$\Phi_0 = \frac{1}{\sqrt{2}} \begin{pmatrix} 0 \\ \nu \end{pmatrix} \tag{2.4}$$

The Lagrangian $\mathcal{L}_\Phi$ is

$$\mathcal{L}_\phi = (D_\mu \Phi)^\dagger (D_\mu \Phi) - \mu^2 (\Phi^\dagger \Phi) - \lambda (\Phi^\dagger \Phi)^2. \tag{2.5}$$

$D_\mu \Phi$ is the covariant derivative, $D_\mu \Phi = (\partial_\mu + ig\boldsymbol{\tau} \cdot \boldsymbol{W}_\mu/2 + ig' Z_\mu/2)\Phi$. $\boldsymbol{W}$ and Z are the $SU(2)$ and $U(1)$ gauge bosons. Using $\Phi \to \nu + h$ to expand $\mathcal{L}_\Phi$, we get

$$\mathcal{L}_\Phi = (\partial_\mu h)^2/2 + m_W^2 W_\mu^+ W^{-\mu}(1+\frac{h}{\nu})^2 + m_Z^2 Z_\mu Z^\mu (1+\frac{h}{\nu})^2 + \frac{\mu^4}{4\lambda} + \mu^2 h^2 + \lambda\nu h^3 + \frac{\lambda}{4} h^4. \tag{2.6}$$

The masses of the W and Z appear as couplings to the Higgs potential. The coupling of the Higgs boson with W and Z bosons is proportional to the square of their masses.

Similar for the fermions, before symmetry breaking, the interactions between Higgs and fermions are

$$\mathcal{L}_{\text{Yukawa}} = -\sum (\Gamma^\mu_{mn} \bar{q}_{mL} \tilde{\Phi} u_{nR} + \Gamma^d_{mn} \bar{q}_{mL} \Phi e_{nR} + \Gamma^e_{mn} \bar{l}_{mL} \tilde{\Phi} \nu_{nR}). \tag{2.7}$$

where $\tilde{\Phi}$ breaks into

$$\tilde{\Phi} \to \frac{1}{\sqrt{2}} \begin{pmatrix} \nu + h \\ 0 \end{pmatrix}. \tag{2.8}$$

The matrices Γ^i_{mn} are arbitrary but proportional to a mass matrix. After symmetry breaking, defining $M_{mn} = \nu \Gamma_{mn}/\sqrt{2}$, the Yukawa Lagrangian becomes:

$$\mathcal{L}_{\text{Yukawa}} = -\bar{l}_{mL} M^e_{mn} (1 + gh/2m_W) e_{nR}/\sqrt{2} + ... \tag{2.9}$$

Thus the resultant masses of fermions are proportional to the coupling of the Higgs boson

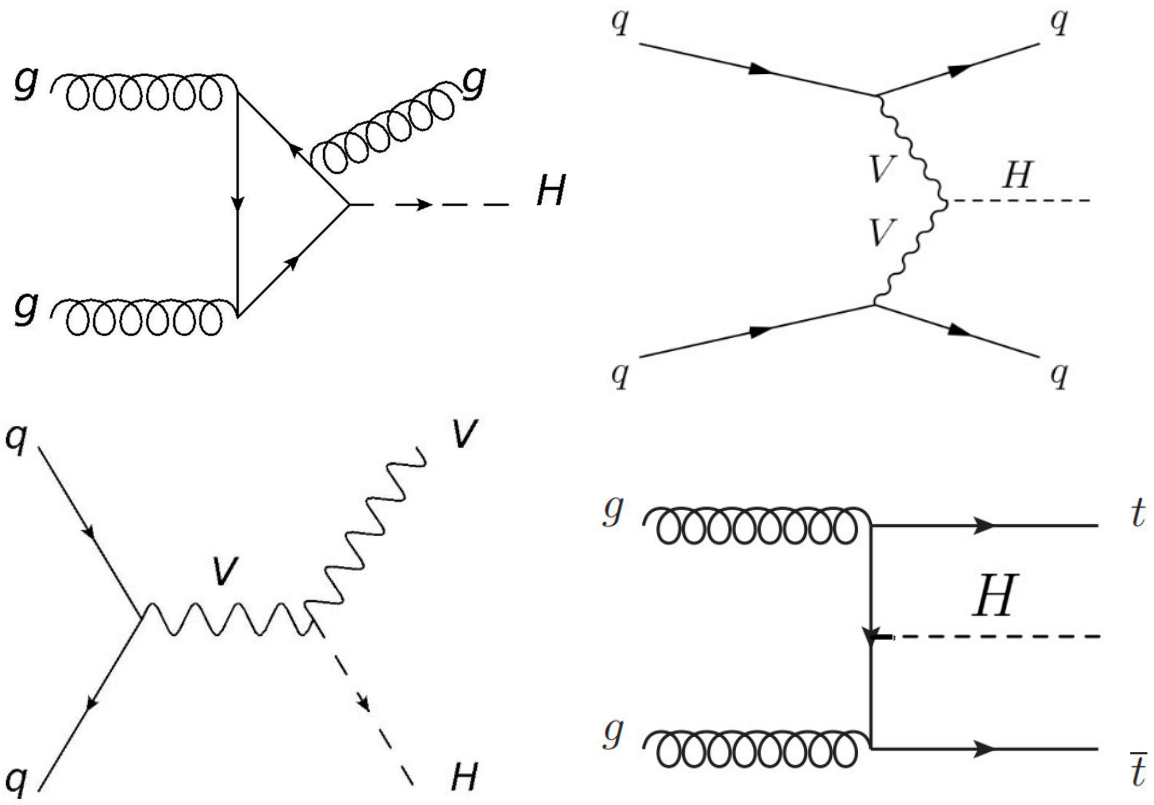

Figure 2.3: Leading order diagrams for Higgs production at the LHC. The gluon gluon Fusion (ggF) produces the Higgs via a top quark loop. The Vector Boson Fusion (VBF) where vector boson can be either $W^{\pm}$ or Z^0 boson produces the Higgs with two energetic jets. The VH diagram produces the Higgs with a $W^{\pm}$ or Z^0 boson. The ttH diagram produces the Higgs with a pari of top quarks.

with the fermions. More details of the Higgs mechanism can e found in [43, 47].

2.3 Higgs Production at the LHC

Since the Higgs boson couples to fermions proportionally to their mass and particles in colliders either have small mass or do not couple to the Higgs boson directly, Higgs boson production is a rare process (one in a million collisions at the LHC). The main goal of the LHC was to discover the Higgs boson as large data sets of high energy collisions of protons provide sensitivity to Higgs production in relevant mass range.

There are four ways to produce a Higgs boson at the LHC as shown in Figure 2.3. The

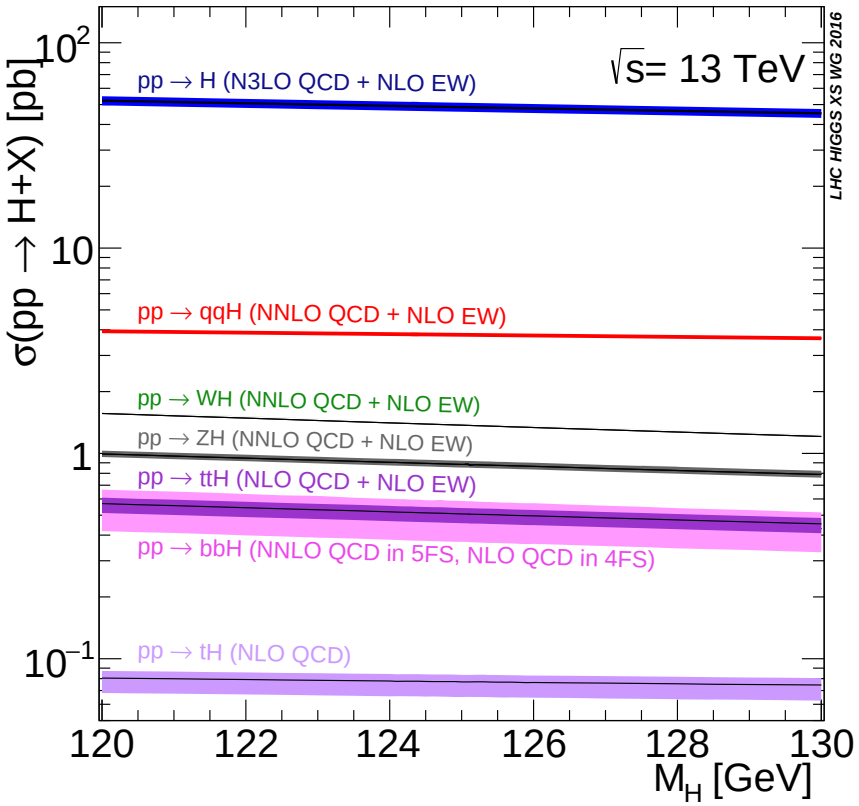

Figure 2.4: Cross sections of Higgs boson for all the productions in Standard Model. ggH process is colored blue. VBF process is colored red. VH process is colored green for $W^{\pm}$ boson and black for Z^0 boson. ttH is colored purple.

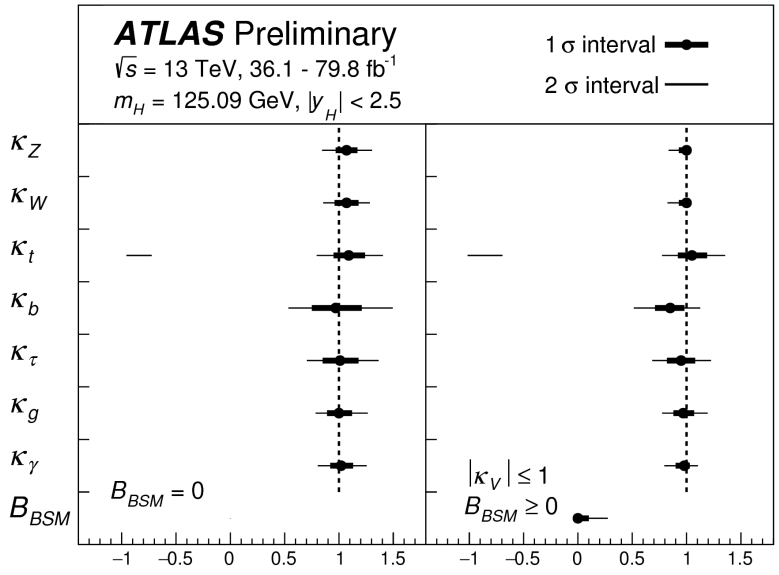

Figure 2.5: Best-fit values and uncertainties of Higgs boson coupling modifiers κ per particle type either allowing no Beyond Standard Model (BSM) coupling (left), or allowing BSM coupling as a free parameter (right). The SM corresponds to $B_{\mathrm{BSM}} = 0$ and all κ set to unity. All parameters except κ_t are assumed to be positive. When BSM is allowed, the conditions $\kappa_{W,Z} < 1$ are also applied.

corresponding cross sections at the LHC are shown in Figure 2.4. This thesis will focus on the production mode with second largest cross section, Vector Boson Fusion. It has a production cross section of 3766 fb for $m_h = 125$ GeV at $\sqrt{s} = 13$ TeV.

Great progress has made towards measuring Higgs boson production cross sections and branching fractions. Figure 2.5 shows the coupling modifiers per particle type, i.e. deviations from SM, after a combined likelihood fit. Constraints from visible channels put a 26% constraint on BSM decay width of Higgs boson, assuming SM like couplings [16].

2.4 Astrophysical evidence for Dark Matter

Dark matter is a form of matter that makes up 85% matter of the universe. There are a variety of astrophysical observations that can be explained by the existence of such matter.

The history of the idea of Dark Matter goes back to 1884 when Lord Kelvin showed in a talk an inconsistency between the mass of the visible stars and the estimation of the

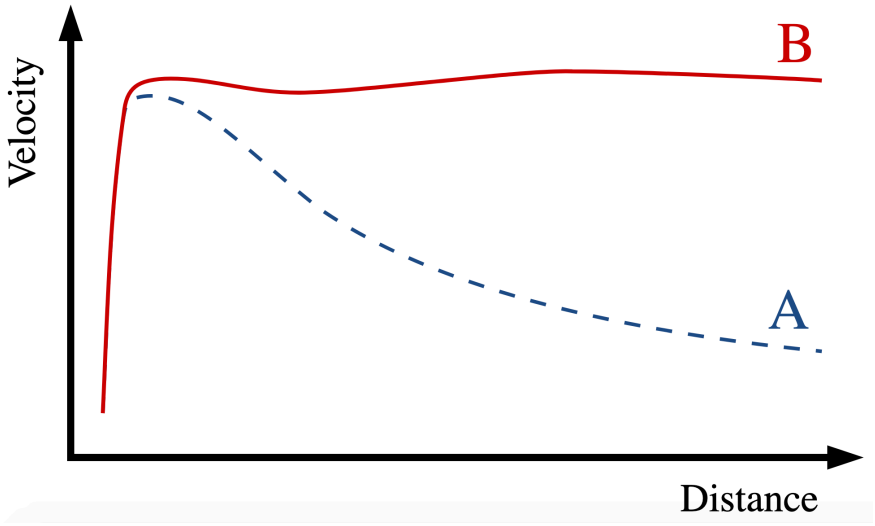

Figure 2.6: A cartoon of the observed galaxy rotation curve (B) and the predicted galaxy rotation curve by visible mass only (A).

mass of the galaxy based on measurements of the velocity dispersion of the orbiting stars. Suggestion of the existence of dark matter was raised by Jacobus Kapteyn, Jan Oort and Fritz Zwicky in early 20 century. In the 1970s, galaxy rotation curves provided stronger evidence of such claims. Galaxy rotation curve is a plot of the speed of the visible parts of a galaxy versus their distance from the center of the galaxy. The observed curve has a significant discrepancy from the predicted curve based on visible matters in the galaxy [53]. Figure 2.6 shows a cartoon of the shape of the curves. Existence of Dark Matter can be used to explain such discrepancy.

Since then, a variety of other cosmological observations have been made that further confirm the existence of Dark Matter, such as gravitational lensing. Gravitational lensing is a consequence of General Relativity where massive objects act like a lens between an observer and a distant light source. Mass of the massive objects can be calculated based on distortion of the background galaxies. Bigger mass results in more lensing. Distribution and dynamics of Dark Matter can be deduced [61, 52].

Alternative theories attempt to explain the observed discrepancies using modified gravity. However, the observation of the bullet cluster challenges these theories while further

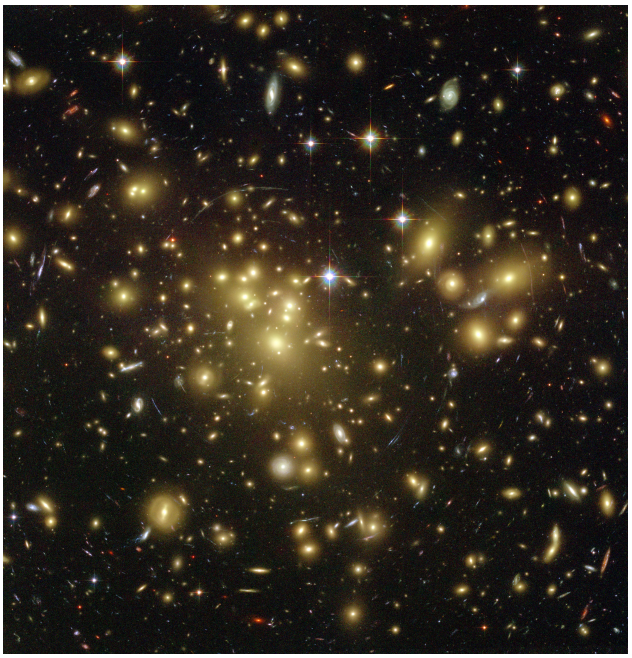

Figure 2.7: An enlarged image observed by the Hubble Space Telescope in Abell 1689 showing strong gravitational lensing.

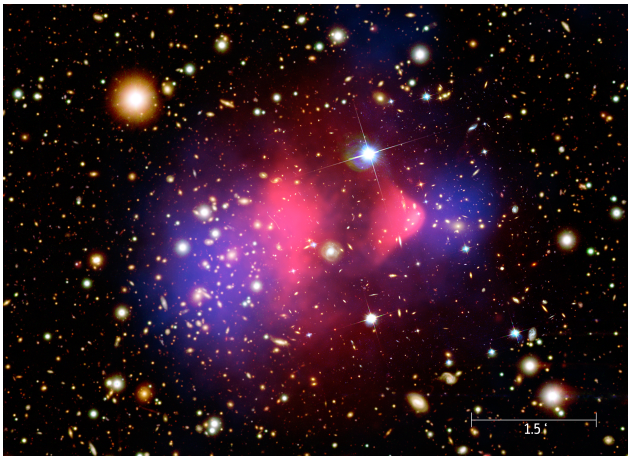

Figure 2.8: X-ray photo of a bullet cluster by Chandra X-ray Observatory (shown in pink) and the mass distribution of the clusters calculated from gravitational lens effects (shown in blue).

confirming the existence of Dark Matter and its potential weakly interacting property. A Bullet Cluster, as pictured in Figure 2.8, is a result of a collision between two galaxy clusters. Its center of mass is found to be far from the the center of mass of visible matter [35]. This can be explained by some cold non-interacting DM smoothly passing through while visible matter slowed down due to electromagnetic interactions. Thus tensions between the visible objects and the mass distribution were observed. This is indication that there is a matter that is very weakly interacting that is dominating the clusters mass.

2.5 Using Higgs to Search For Dark Matter

According to observational evidence, Dark Matter candidates must satisfy several conditions. It interacts almost solely gravitationally. Its other effective couplings to SM are zero or small. It has to be cosmologically stable and approximately cold or non-relativistic. A good candidate is the Weakly Interacting Massive Particles (WIMP) which are Dark Matter particles that weakly interact with SM particles, thus detectable in laboratories on earth.

Since the Higgs boson couples to the mass of fermion and $W^{\pm}$ and Z bosons, it is natural to think the Higgs boson might couple to the mass of Dark Matter particles as well. The simplest model that incorporates this idea is the Higgs Portal model [42]. Consider three forms of dark matter, scalar S, fermion χ and vector boson V. The stability of the DM particle is ensured by a model dependent Z_2 parity. The relevant terms in the Lagrangians are then

$$\begin{aligned}
\Delta\mathcal{L}_S &= -\frac{1}{2}m_S^2 S^2 - \frac{1}{4}\lambda_S S^4 - \frac{1}{4}\lambda_{hSS} H^\dagger H S^2, \\
\Delta\mathcal{L}_V &= \frac{1}{2}m_V^2 V_\mu V^\mu + \frac{1}{4}\lambda_V (V_\mu V^\mu)^2 + \frac{1}{4}\lambda_{hVV} H^\dagger H V_\mu V^\mu, \\
\Delta\mathcal{L}_f &= -\frac{1}{2}m_f \bar{\xi}\xi - \frac{1}{4}\frac{\lambda_{hff}}{\Lambda} H^\dagger H \bar{\xi}\xi.
\end{aligned} \tag{2.10}$$

DM particles will appear as invisible decay products of the Higgs when their mass is lighter than half of the Higgs mass. The decay width can be calculated as a function of the

mass of the DM particle,

$$\begin{aligned}
\Gamma^{\rm inv}_{h\to SS} &= \frac{\lambda^2_{hSS}\nu^2\beta_S}{64\pi m_h}, \\
\Gamma^{\rm inv}_{h\to VV} &= \frac{\lambda^2_{hVV}\nu^2 m_h^3\beta_V}{256\pi M_V^4}(1-4\frac{M_V^2}{m_h^2}+12\frac{M_V^4}{m_h^4}), \\
\Gamma^{\rm inv}_{h\to \xi\xi} &= \frac{\lambda^2_{hff}\nu^2 m_h\beta_f^3}{32\pi\Lambda^2},
\end{aligned} \tag{2.11}$$

where $\beta_\xi = \sqrt{1-4M_\xi^2/m_h^2}$.

CHAPTER 3

EXPERIMENTAL SETUP

3.1 Large Hadron Collider

The Large Hadron Collider (LHC) is a super-conducting accelerator in a 27 kilometers long circular tunnel buried 100 meters underground [55, 44, 51]. Originally constructed for the electron-position collider LEP [50], the tunnel is located in the French-Swiss border out side of Geneva (see Figure 3.1). There are seven experiments installed at the LHC: ALICE, ATLAS, CMS, LHCb, LHCf, TOTEM and MoEDAL. They analyze the myriad of particles produced by collisions in the accelerator for different purposes. Inside the LHC, two beams of protons traveling in opposing directions in separate beam pipes are guided by strong magnetic field generated by super-conducting magnets. The beams of protons are met for head-on collisions with a center of mass energy at $\sqrt{s} = 13$ TeV at two locations, the ALTAS detector and the CMS detector.

The protons, generated from hydrogen atoms, go through several stages of acceleration before they enter the LHC tunnel for final acceleration and collisions as shown in Figure 3.2. They start in a linear collider called Linac2 and get accelerated to 50 MeV, then they get injected into the Booster and accelerated further to 1.4 GeV. They then go through two synchrotrons called Proton Synchrotron (PS) and Super Proton Synchrotron (SPS). The protons are accelerated to 26 GeV in PS and then to 450 GeV in SPS. In the end, the proton beams enter the LHC tunnel and get accelerated to 7 TeV. The beams can circulate inside the LHC ring for hours before a beam dump.

Because of the acceleration scheme, the proton beams come in bunches with each bunch containing 10^{11} protons. A cartoon demonstration of the bunches are shown in Figure 3.3. The proton bunches come in bunch trains. Bunch inside a bunch train has a constant spacing of 25 nanoseconds during normal operation and bunches are crossed at 40 MHz. During each bunch crossing many pp interactions occur. The number of simultaneous interactions seen

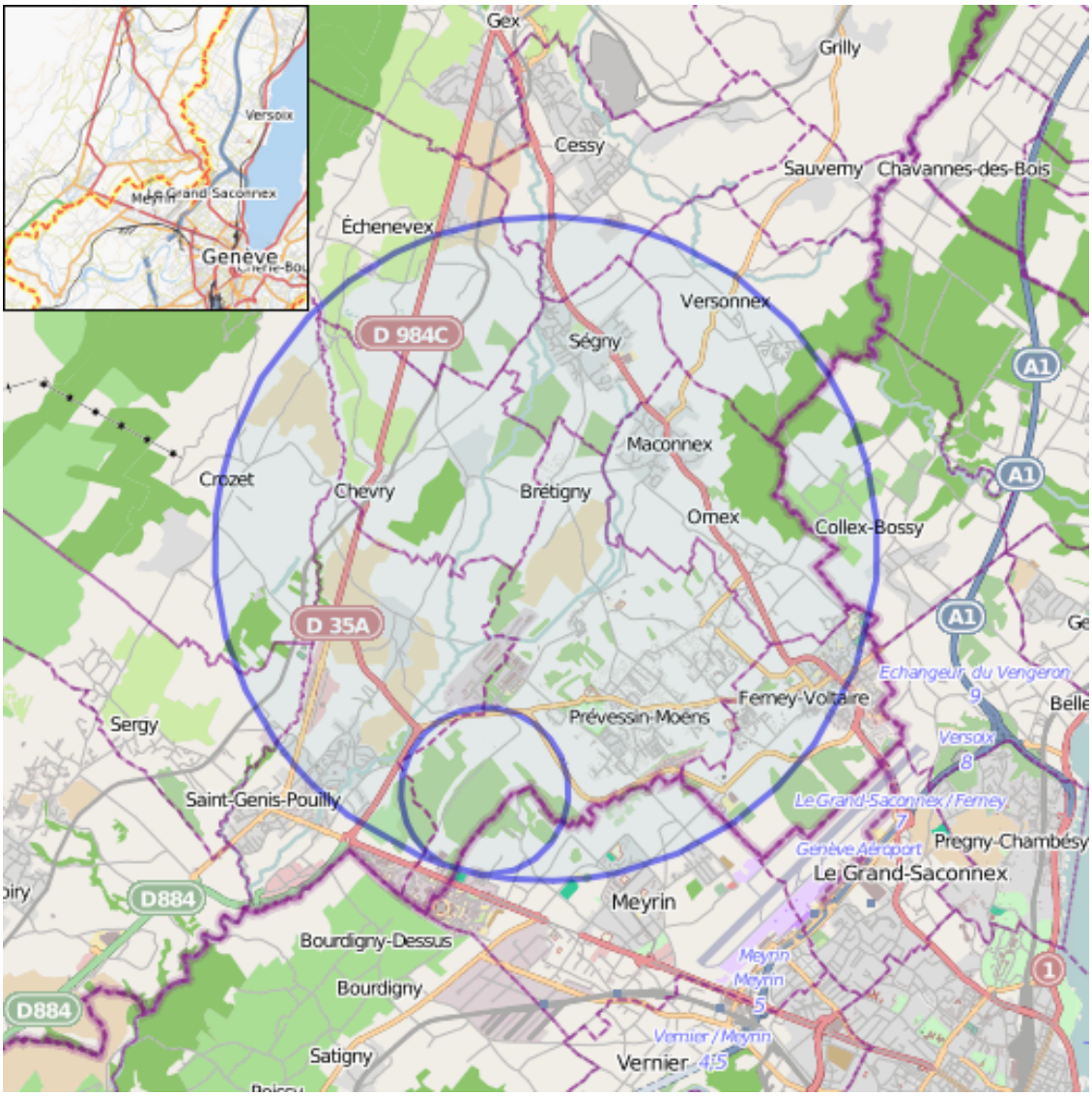

Figure 3.1: LHC tunnels on a map.

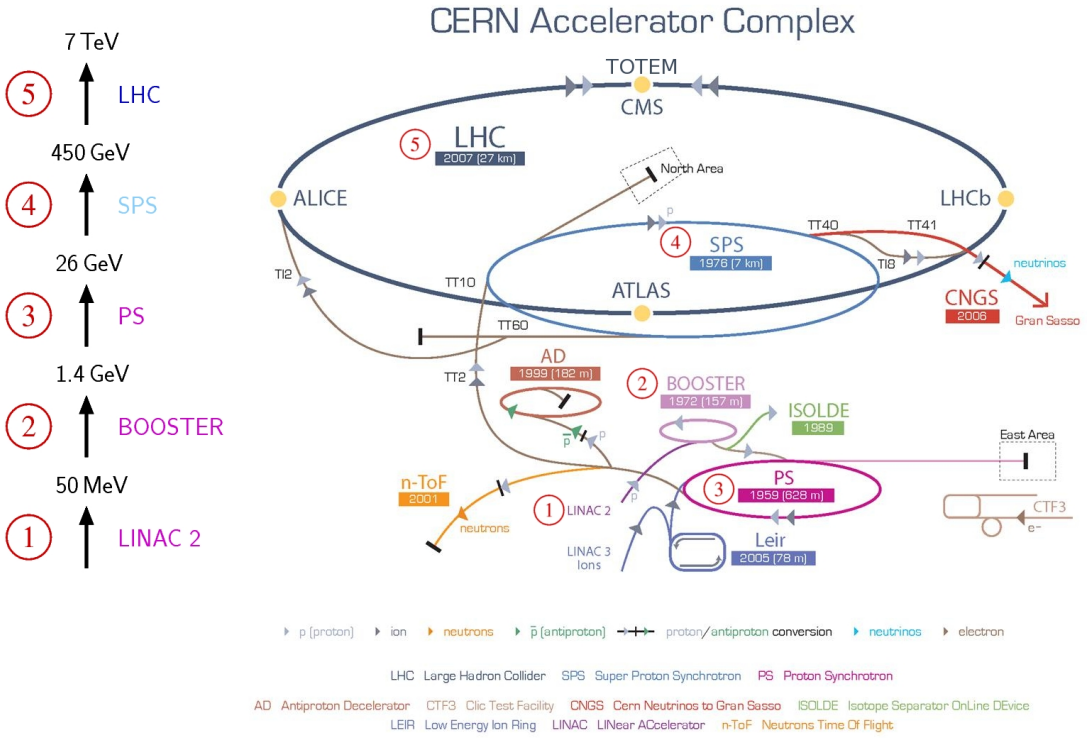

Figure 3.2: CERN accelerator complex. Stages of acceleration the beams go through are labelled with numbers.

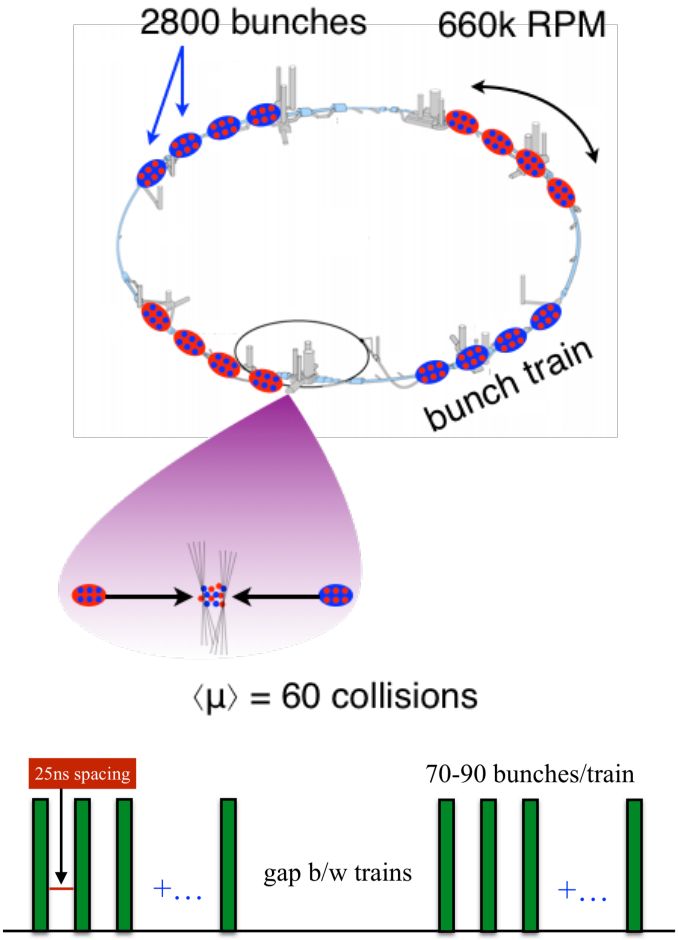

Figure 3.3: Protons come in bunches inside the LHC tunnel. During normal operation, each proton beam contains 2800 bunches. The crossing rate of the bunches is 40 MHz.

by the detector is called pileup.

3.2 ATLAS detector

The ATLAS (A Toroidal LHC ApparatuS) detector is one of the two general purpose detectors sitting in the LHC tunnel. It searches for signature of new physics by measuring the momentum, energy and charge of particles produced in the LHC collisions. The momentum and charge are determined by tracking the particle's path in a magnetic field. The energy is estimated by sampling the particle's energy propagation through layers of absorbing material. The detector consists of three major components, the Inner Detector, the Calorimeters and the Muon Spectrometer. Signal from the detector is read out selectively by the Trigger and Data AcQuisition (TDAQ) system. This chapter gives a brief overview of each component.

3.2.1 Overview

The ATLAS detector [21] is approximately cylindrically symmetric along the beam line. The standard ATLAS coordinate system has its origin at the interaction point (IP), the x-axis pointing from IP toward the center of the LHC ring, and the y-axis pointing upward. Following the right-hand rule, the z-axis points along the beam line, counter-clockwise around the LHC ring when looking downwards. The total momenta of particles from the collisions are not well determined (they are described by Parton Distribution Functions (PDFs)). However, since momentum is conserved in the plane transverse to the beam line, i.e. the $x-y$ plane, we can study the momenta projected into this plane, i.e. transverse momenta. In the transverse plane cylindrical coordinates are used (R, ϕ); ϕ is used to denote the azimuthal angle around the beam line. Pseudorapidity, $\eta \equiv -\ln[\tan(\theta/2)]$, is usually preferred over the polar angle θ because it is well-defined in the detector frame, i.e. independent of the particle mass.

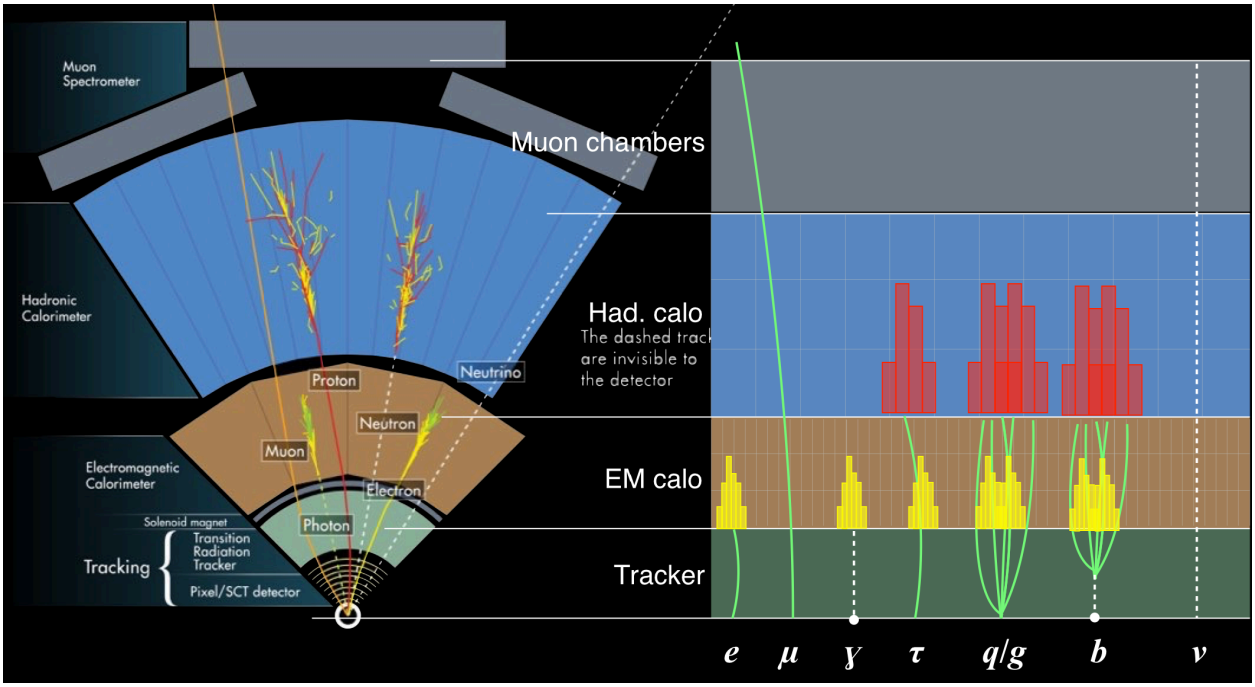

Figure 3.4: A slice of ATLAS detector with cartoon showing what each type of particle would look like in different component.

Figure 3.4 shows how each type of SM particles interact with the components of the detector. Particles coming out of the collisions first hit the Inner Detector (ID), where trajectories of charged particles are bent by a uniform longitudinal magnetic field created by the solenoid magnets so that momentum and charge can be measured. Then electrons and photons are annihilated in the Electromagnetic (EM) Calorimeter so that their energies can be measured. Hadrons are able to reach the Hadronic Calorimeter where their energies are measured. Muons, almost unaffected by the previous components, will have their trajectories further bent by the toroidal magnetic and get their properties measured by the Muon Spectrometer (MS). Strongly coupled particles like quarks and gluons with high energy form collimated cones of hadrons before they hit the detector. These cones are called jets. Neutrinos or dark matter particles are invisible to the detector; however we can "detect" if invisible particles are produced in a collision by momentum conservation on the plane transverse to the beam line and measure their momentum on the transverse plane by detecting the momenta of all visible particles. While the momenta of charged particles are

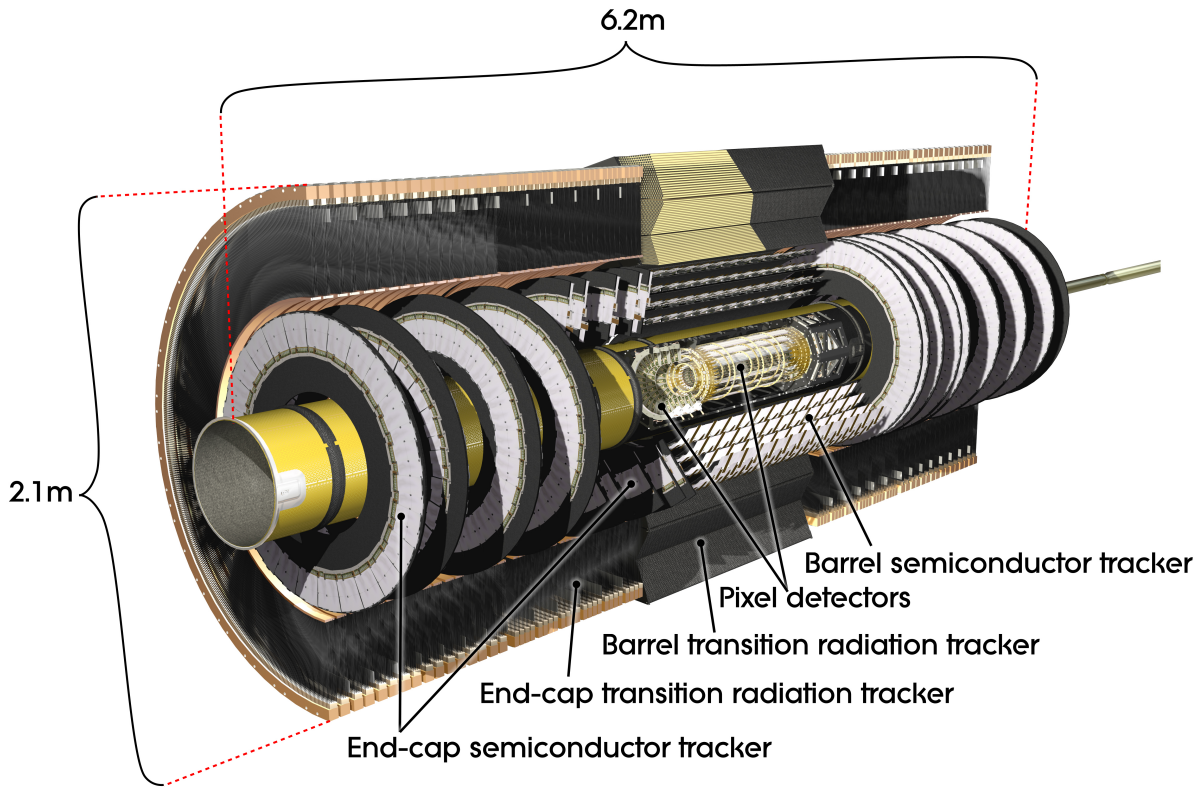

Figure 3.5: ATLAS inner detector. The system is split into barrel and end-cap. The barrel regions consist of concentric cylinders while the end-cap regions consist of disks. The ideal geometry will be such that the angle of incidence of tracks is normal to the surface of the detector. The barrel/end-cap geometry provides a compromise considering the feasibility with flat components.

measured by ID and MS, the momenta of neutral particles can be inferred from the direction and energy of their shower in the calorimeters. Many particles decay before they reach the detector, so their properties must be inferred from the properties of their decay products using conservation laws.

3.2.2 Inner Detector

The ID measures the position, momentum and origin of charged particles [22, 23]. It consists of three components as shown in Figure 3.5: pixel detector, semiconductor tracker (SCT) and the transitional radiation tracker (TRT). A solenoid magnet wrapping around the ID provides a uniform 2 T magnetic field parallel to the beam line so that charged particles are

bent and momenta can be measured.

Both the pixel detector and the SCT use silicon pixels and microstrips. When a charged particle passes through material it usually excites some electrons in the material. When the material is silicon the difference in Fermi energies on either side of an interface between the two different semiconductors can create a region with no free charge carriers. When a charged particle passes through, the charges will not recombine immediately due to the lack of free charge carriers. The ID applies to silicon pixels and microstrips a bias voltage between 100-300 V so that the electron-hole pairs can be separated and measured and the region void of free charge carriers are enlarged.

Pixel detector is closest to the beam line. It consists of four layers of small rectangular silicon detectors. A charged particle can excite electrons in multiple pixels. The amount of charge in nearby pixels and the shape formed by hit pixels are used to calculate the 2D coordinate information of the particle.

Further from the beam line is the SCT. It consists of long silicon microstrips arranged in four layers in R and nine layers in z, covering region up to $|\eta|$ <2.5. Each layer consists of two sub-layers where the microstrips are at a 40 mrad angle so that 2D coordinate information can be inferred with a great resolution in ϕ.

Surrounding the SCT is the TRT. It is a straw tracker with layers of 4 mm diameter straws filled with xenon gas and gold wires in the center. A bias voltages in the range 1400-2000 V is applied between the inner walls of the straw and gold wires. When a charged particle passes through the straw, it ionizes the gas. The electrons drift towards the wire and induce an amplified signal. TRT provides tracking up to $|\eta| < 2.0$. It is also used to identify particles via transition radiation. Polypropylene-polyethylene felt mats interleaved with the straws induce transition radiation by incident particles which is then absorbed by xenon gas and leads to cluster of electron shower. This allows for an estimate of the charged particle mass.

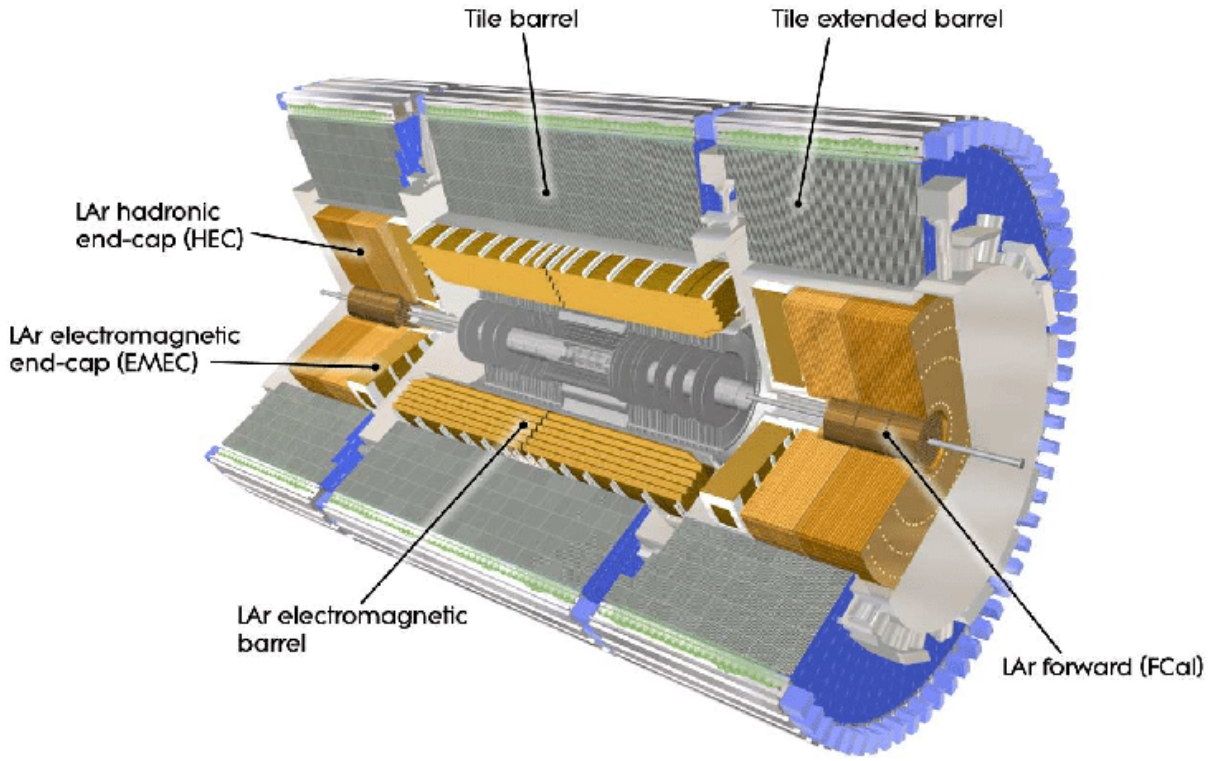

Figure 3.6: ATLAS calorimeters.

3.2.3 Calorimetry

The ATLAS calorimeter consists of electromagnetic calorimeter and hadronic calorimeter as shown in Figure 3.6. Calorimeters used by ATLAS generally consist of alternating layers of absorber material and sampling material. When particles pass through the absorber material they scatter and produce showers of particles, either electromagnetically or hadronically. If the energy of particles fall below the threshold of electron-positron pair production, the particles are fully absorbed. Otherwise the particles make it through the absorber material and reach the next part. When the particles pass through the sampling material, ionization or Cherenkov radiation occurs or scintillating molecules are excited. If ionization occurs a bias voltage is applied to drift the charge carriers to electrodes. If Cherenkov radiation occurs or scintillating molecules are excited, photons are produced and measured by photomultiplier tubes (PMTs).

Liquid Argon (LAr) Electromagnetic Calorimeter

The LAr Calorimeter is the innermost calorimeter [24]. While all SM particles except neutrinos and muons deposit significant percentage of their energy in LAr, photons and electrons are likely to deposit all their energy here. The LAr detector has a specialized geometry that provides uniform and extensive ϕ coverage and fast readout. It has three radial sections with different η-ϕ granularities.

Tile Calorimeter

The tile calorimeter measures the energy of hadrons in the range $|\eta| < 1.7$ [26]. It consists of steel absorbers and plastic scintillators broken into $\Delta\eta \times \Delta\phi = 0.1 \times 0.1$ tiles. When the shower hits the scintillators, photons are produced and guided to PMTs via wavelength shifting fibers for better detection efficiency.

Hadronic Endcap Calorimeter

The hadronic endcap calorimeter measures the energy of hadrons for $1.7 < |\eta| < 3.2$. Liquid argon with copper absorbers are used.

Forward Calorimeter

The forward calorimeter measures energy of hadrons for $3.1 < |\eta| < 4.95$. It consists of Liquid argon and one copper layer and two tungsten layers.

3.2.4 Muon Spectrometer

The MS is designed to measure the transverse momentum of muons to within a few percent uncertainties [25]. Muons' trajectories are first bent in the transverse plane by 2 T magnetic field of the solenoid magnet and then bent in the longitudinal plane by 0.5 T magnetic

field of the large toroidal magnet for a larger total path deflection. The MS consists of two tracking systems and two trigger systems.

The Monitored Drift Tubes (MDTs) and the Cathode Strip Chambers (CSCs) are used for precision tracking. MDTs consist of long aluminum tubes ranging from 0.7 to 6.3 m with 50 μm gold-coated tungsten wires in the center. The tubes are filled with a mixture gas consisting of 91 % argon, 5 % methane and 4 % nitrogen. A bias voltage of 3300 V is applied between the tube and the wire. MDTs are arranged such that muons are sampled up to six times. The positions of the panels are monitored using optical alignment. CSCs are used in regions where occupancy is too high for MDTs, i.e. at low $|z|$ and high $|\eta|$ region. They consist of chambers with tungsten wires perpendicular to cathode readout strips in a mixture gas of 30 % argon, 50 % CO_2 and 20 % CF_4.

The Resistive Plate Chambers (RPCs) and Thin Gap Chambers (TGCs) are designed for high efficiency trigger (99% efficiency) and fast decision making as it needs to make decision within each bunch crossing (25 ns, see Section 3.1). RPCs consist of pairs of resistive plates separated by $C_2H_2F_4$ filled narrow region (2 mm). Charges from gas ionized by muons are enlarged by 8900 V potential between plates and are read out via orthogonal read-out strips. TGCs consist of gold-plated tungsten wires in a mixture gas of CO_2 and n-pentane. Charges from gas ionized by muons are read out via both strips and wires. RPCs and TGCs are also used for position estimate in direction perpendicular to MDTs and CSCs.

3.2.5 Trigger System

While 40 million crossings/events per second happen at the LHC, we only have disk space to store about 1000 events. A dedicated trigger system is needed to optimize physics output. The ATLAS trigger system consists of two parts: hardware based Level 1 (L1) trigger and software based High Level Trigger (HLT).

The L1 trigger makes fast decisions and selects approximately 1 in 400 events by searching for large localized energy deposits in the calorimeters or angular coincidence detections in

the muon spectrometer. It reduces the event rate from 40 MHz to 100kHz. About one third of that rate is used by the muon trigger, another third by the EM calorimeter trigger, and the rest is for hadronic calorimeter triggers or combined objects. Constant efforts are made to balance between inclusive trigger used by many analysis and dedicated triggers maximizing the efficiency for a single analysis.

The events selected by the L1 trigger are then passed on to the HLT, which selects about 1 in 100 events. The HLT consists of a large computing farm with more than 20,000 processors. The HLT is the first stage where tracking can be done based on information from the ID. This allows for electron/photon discrimination, jet flavor tagging, track based $E_{\mathrm{T}}^{\mathrm{miss}}$ terms, global sequential jet calibration and more. Track reconstruction is either done in small Regions of Interest (ROIs) near the corresponding calorimeter activity or globally depending on the needs of the specific trigger type.

The data used in this thesis are events either recorded by a $E_{\mathrm{T}}^{\mathrm{miss}}$ trigger or lepton triggers. The $E_{\mathrm{T}}^{\mathrm{miss}}$ trigger algorithm used in HLT during 2015-2016 data taking calculated the $E_{\mathrm{T}}^{\mathrm{miss}}$ by taking the magnitude of the vector sum of all jet p_{T}s. It was replaced by the Pileup FITting (PuFIT) algorithm by the end of 2016 to cope with higher pileup. The lepton trigger algorithms resemble algorithms used in offline reconstruction.

CHAPTER 4

SEARCH FOR H → INVISIBLE

This chapter presents the search for invisible decays of a Higgs boson with the integrated luminosity of 36.1 fb^{-1} at 13 TeV, which was published in 2019 [38]. The primary contribution comes from a Higgs boson produced via the Vector Boson Fusion (VBF) mechanism (see Figure 4.1). A secondary but non-negligible contribution to the signal comes from gluon figure (ggF+2jets) as shown Figure 4.2). Both VBF and ggF are treated as signal, with no interference between the two production modes considered[1]. The analysis was performed using 36.1 fb^{-1} of $\sqrt(s) = 13$ TeV data collected during the first part of Run 2 (2015-2016). This is the first published ATLAS results on this search in Run 2.

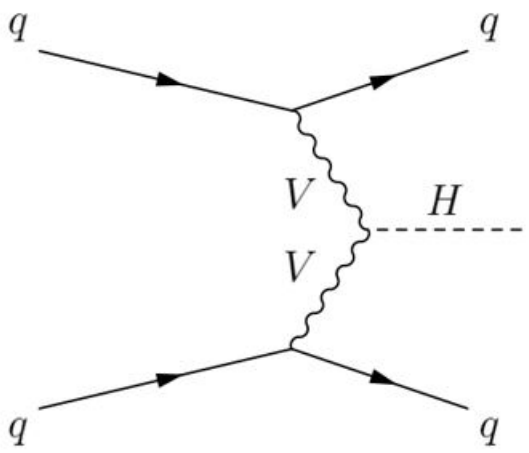

Figure 4.1: Higgs production via Vector-Boson Fusion.

The same search was initially performed in Run 1 by both ATLAS [20] and CMS [34]. In Run 1, ATLAS placed an observed (expected) upper limit at 0.28 observed (0.31 expected) using VBF production of Higgs with integrated luminosities of 4.7 and 20.3 fb^{-1} at 7 and 8 TeV respectively.

The major backgrounds of this search is $W \to \ell\nu$+jet sand $Z \to \nu\nu$+jets. There are two leading productions of W and Z (see Figure 4.3). One involves quark gluon interactions

1. The interference is small.

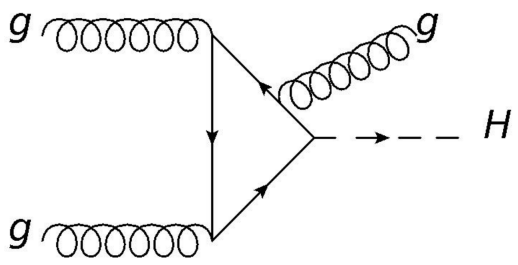

Figure 4.2: Higgs production via gluon-gluon Fusion.

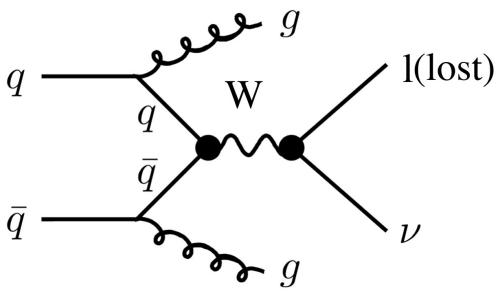

(a) $W \to \ell_{\text{lost}}\nu$ Strong.

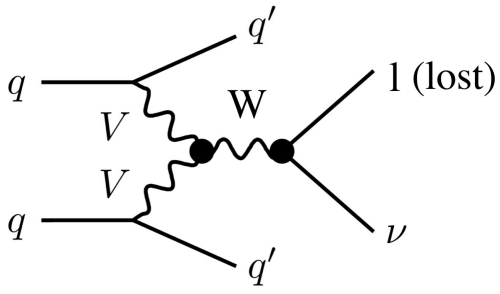

(b) $W \to \ell_{\text{lost}}\nu$ EWK.

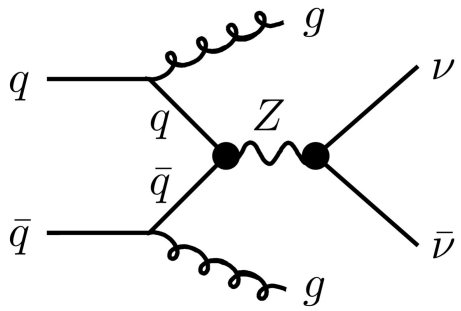

(c) $Z \to \nu\nu$ Strong.

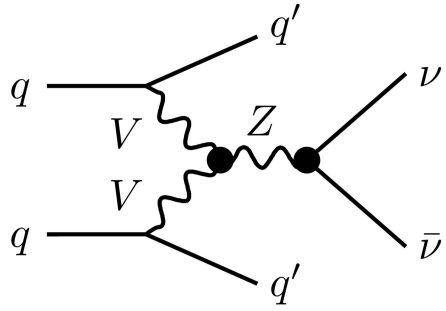

(d) $Z \to \nu\nu$ EWK.

Figure 4.3: Leading diagrams for $W \to \ell_{\text{lost}}\nu$ and $Z \to \nu\nu$ background.

and we call it the Strong component of W/Z background; the other involves quark quark interactions and we call it the Electroweak (EWK) component of W/Z background. The Strong component has different kinematic distribution from the VBF signal. The EWK component has exactly the same kinematic distribution as the VBF signal. As the LHC increased its energy, the cross section of the Strong component went up more than that of the EWK component/VBF signal.

The chapter is organized as follows: Section 4.1 describes the data sets and the Monte Carlo (MC) samples used to model the signal and backgrounds. Section 4.2 describes the cor-

Table 4.1: $E_{\mathrm{T}}^{\mathrm{miss}}$ triggers used for 2015-2016 data taking. The years and run numbers where thresholds were changed are noted.

Period	Trigger
All 2015	HLT_xe70_mht
2016, Runs $\leq$ 304008	HLT_xe90_mht_L1XE50
2016, Runs $>$ 304008	HLT_xe110_mht_L1XE50
All	HLT_noalg_J400

Table 4.2: List of single lepton triggers.

Period	Electron	Muon
All 2015	HLT_e24_lhmedium_L1EM20VH HLT_e60_lhmedium HLT_e120_lhloose	HLT_mu20_iloose_L1MU15 HLT_mu50
2016 Runs $\leq$ 304008	HLT_e24_lhtight_nod0_ivarloose HLT_e60_lhmedium_nod0 HLT_e140_lhloose_nod0	HLT_mu50 HLT_mu26_ivarmedium
2016 Runs $>$ 304008	HLT_e26_lhtight_nod0_ivarloose HLT_e60_lhmedium_nod0 HLT_e140_lhloose_nod0	HLT_mu50 HLT_mu26_ivarmedium

rections applied to MC samples. Section 4.3 describes the event selection used in the various channels. Section 4.4 presents the background estimation process. Section 4.5 describes the main sources of experimental systematic uncertainty and theoretical systematic uncertainty respectively. Section 4.6 describes the fitting procedure and the statistical model. Section 4.7 and 4.8 present the results, interpretations and conclusions.

4.1 Data and Monte Carlo simulations

4.1.1 Dataset

The analysis is performed using ATLAS data collected in 2015 and 2016, when the LHC delivered proton-proton collisions at $\sqrt{s} = 13$TeV. The total integrated luminosity is 36.1 fb^{-1}. Only events recorded during stable beam conditions and with all ATLAS sub-systems fully operational are considered. The data used in this analysis were recorded with either a $E_{\mathrm{T}}^{\mathrm{miss}}$ trigger (Table 4.1) or a single lepton trigger (Table 4.2).

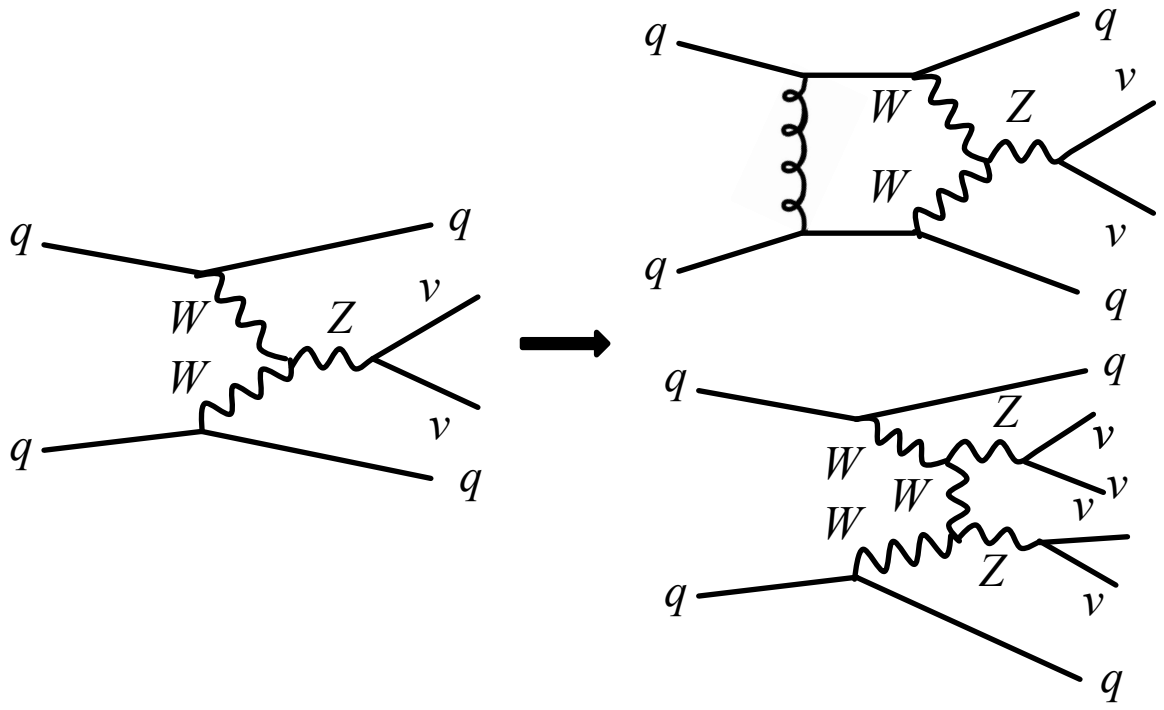

Figure 4.4: Example of higher order diagram for $Z \to \nu\nu$ in α_S and α_{EW}.

4.1.2 MC samples

Background MC samples

The major background processes ($Z \to \nu\nu$+jets and $W \to \ell\nu$+jets), as well as $Z \to \ell\ell$+jets, are modeled using Sherpa 2.2.1 [45]. The calculations use the Comix [46] and OpenLoops [33] matrix element generators, merged with the Sherpa parton shower [57] using the ME+PS@NLO prescription [48]. The NNPDF3.0 NNLO PDF set [28] is used with dedicated parton shower developed by the Sherpa authors.

The W/Z+jets simulation consists of two components based on the order in the electroweak coupling constant α_{EW}: the Strong component (α_{EW}^2) and the electroweak (EWK) component (α_{EW}^4). The Strong component is normalized to Next Next Leading Order (NNLO) cross sections. The EWK component uses generator cross section.

Matrix elements for the Strong component are calculated at Next Leading Order (NLO)

Order	α_{EW}^{2}	α_{EW}^{3}	α_{EW}^{4}	α_{EW}^{5}
α_{S}^{0}	Sherpa 2.2	N/A	Sherpa 2.2	Negligible
α_{S}^{1}	Sherpa 2.2	MadGraph 5	Scale Variation	Negligible
α_{S}^{2}	Sherpa 2.2	Negligible	Scale Variation	Negligible
α_{S}^{3}	Sherpa 2.2	Negligible	Scale Variation	Higher Order
α_{S}^{4}	Scale Variation	Negligible	Higher Order	Higher Order

Table 4.3: Table of all the W/Z components simulated. Scale variation means the process is covered by the scale variation systematics (see Section 4.5).

in α_S for up to 2 final-state partons, and Leading Order (LO) for up to 4 partons. These events are normalized to the Next Next Leading Order (NNLO) cross sections. Examples of higher order diagrams are shown in Figure 4.4. The EWK component is split into two parts: the diboson diagrams (two s-channel bosons (on-shell only, off-shell considered negligible)) and the VBF diagrams (t-channel propagators). The interference between these two diagram types is assumed to be negligible. Matrix elements for the VBF part are calculated at LO in α_S for up to 3 final-state partons. Matrix elements for the diboson part are calculated at NLO in α_S for for up to 3 final-state partons and and LO for up to 5 partons.

In addition term of order α_{EW}^{3} from interference between the strong and electroweak production modes is modeled using MadGraph5_aMC@NLO [4], the NNPDF3.0 NNLO PDF set with parton showering done by Pythia 8 [59].

Table 4.3 summarizes the corresponding generator for each component of the W/Z background discussed above.

Additional backgrounds in the SR from top processes and QCD multijets are very small compared to W/Z backgrounds. Both pair production and single-top backgrounds are simulated using Powheg, interfaced with Pythia for hadronization and showering and EvtGen for the b decays. The QCD multijet background is estimated using data driven method (see Section 4.4).

Signal MC samples

Both ggF and VBF $H \rightarrow$invisible processes are simulated up to NLO in α_S by Powheg interfaced with Pythia for hadronization and showering. The decay of Higgs to invisible particles is simulated as its decay to two Z bosons, which then decay to neutrinos. The difference between this SM process and other BSM decays is negligible, as the Higgs is always produced on-shell for any scenarios we are sensitive to. NLO electroweak corrections are computed separately using HAWK [41].The Higgs production cross sections are taken from [40, 56].

VBF samples with heavier scalar masses were also generated for heavy scalar mediator interpretations of the results. The production of these samples is exactly the same as that of the main signal sample; the only difference is the scalar mass.

4.2 MC corrections

This section describes the correction factors applied to MC samples to correct for pileup effects, trigger efficiencies and vetoing leptons.

4.2.1 Pileup reweighting

The MC samples are generated with a fixed pileup (μ) distribution, which is different from the actual distribution in data. To correct for this, a pileup reweighting procedure is performed. A set of weights is derived from the data and MC distributions as a function of μ, and then applied to MC on event level[30, 13]. The total normalization of the sample is preserved after the reweighting process.

A pileup reweighting systematic is introduced to cover the uncertainty on the ratio between the predicted and measured inelastic cross-section in the fiducial volume defined by $M_X > 13$ GeV, where M_X is the mass of the hadronic system [1].

This reweighting is essential because the analysis is pileup dependent. Figure 4.5 shows

Figure 4.5: Cut efficiency as a function of pileup $< \mu >$. Red line shows the distribution with all the analysis selection. Blue line shows the distribution with all the analysis selection except the third jet veto.

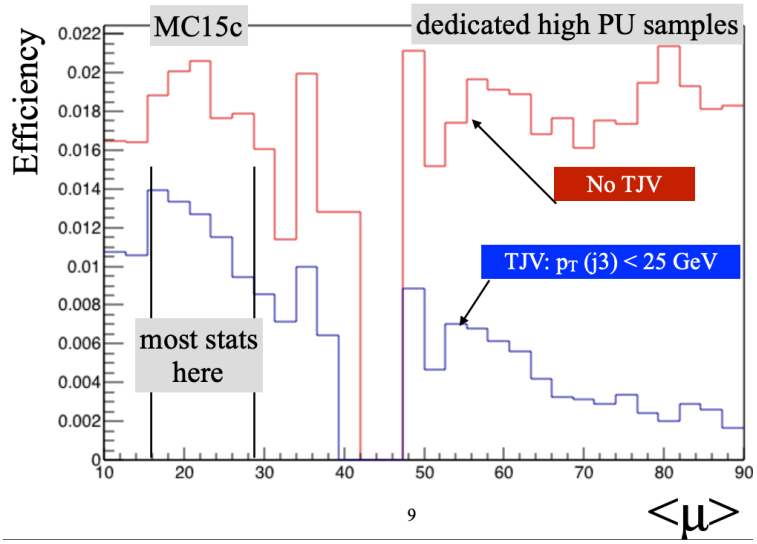

the cut efficiency (ratio of number of events passing analysis selection to total number of events) as a function of pileup with all the analysis selection and that excluding a specific requirement which is a veto on any event with a third jet. This requirement rejects lots of QCD background, but it makes our analysis more pileup dependent.

4.2.2 E_T^{miss} trigger scale factor

To account for systematic mismodelling of trigger efficiency in MC, we apply a trigger scale factor to MC events, defined as the ratio of the efficiency in data divided by the efficiency in MC simulation. The $E_{\mathrm{T}}^{\mathrm{miss}}$ trigger efficiency is measured in data using a single muon trigger as a reference trigger. Figure 4.6 shows that the MC simulation tends to overestimate the efficiency by around 5% for $E_{\mathrm{T}}^{\mathrm{miss}} > 150$ GeV.

Figure 4.7 compares the scale factors between two different trigger thresholds that were operational in 2016 and bewteen electrons and muons. The difference between the thresholds is less significant than the difference between the electron and muon selections. We assign a 1% uncertainty on the scale factor, which covers both the difference between the corrections

evaluated for electrons and muons, and the difference between the nominal and largest corrected value. This makes a negligible impact on the analysis sensitivity.

To simplify implementation and smooth statistical fluctuations, the scale factor is fit to the function:

$$\frac{1}{2} \cdot [1 + Erf((E_{\mathrm{T}}^{\mathrm{miss}} - p_0)/\sqrt{2 \cdot p_1})]. \tag{4.1}$$

4.2.3 Lepton veto scale factors

The SR selection vetos events with any reconstructed leptons. Since scale factors for leptons are corrected based on observed leptons, these have to be inverted to cover the leptons lost due to reconstruction effects. Since the effects for electrons are larger than for muons, we only consider electrons. Figure 4.8 shows the η vs. p_{T} distribution of the anti-ID scale factors to correct for the electron identification, at low p_{T}.

The scale factors are applied for all events MC events that pass the SR selection, and have a truth electron that could have been reconstructed, that is with $p_{\mathrm{T}} > 7$ GeVand $|\eta| < 2.47$. The correction factor, accounting for identification, reconstruction and isolation is 1.06 $\pm$ 0.20.

4.3 Event selection

This section provides detailed descriptions on the selection and requirement on the physics objects used in the analysis.

4.3.1 Object selection

This section provides detailed descriptions on the physics objects used in the analysis.

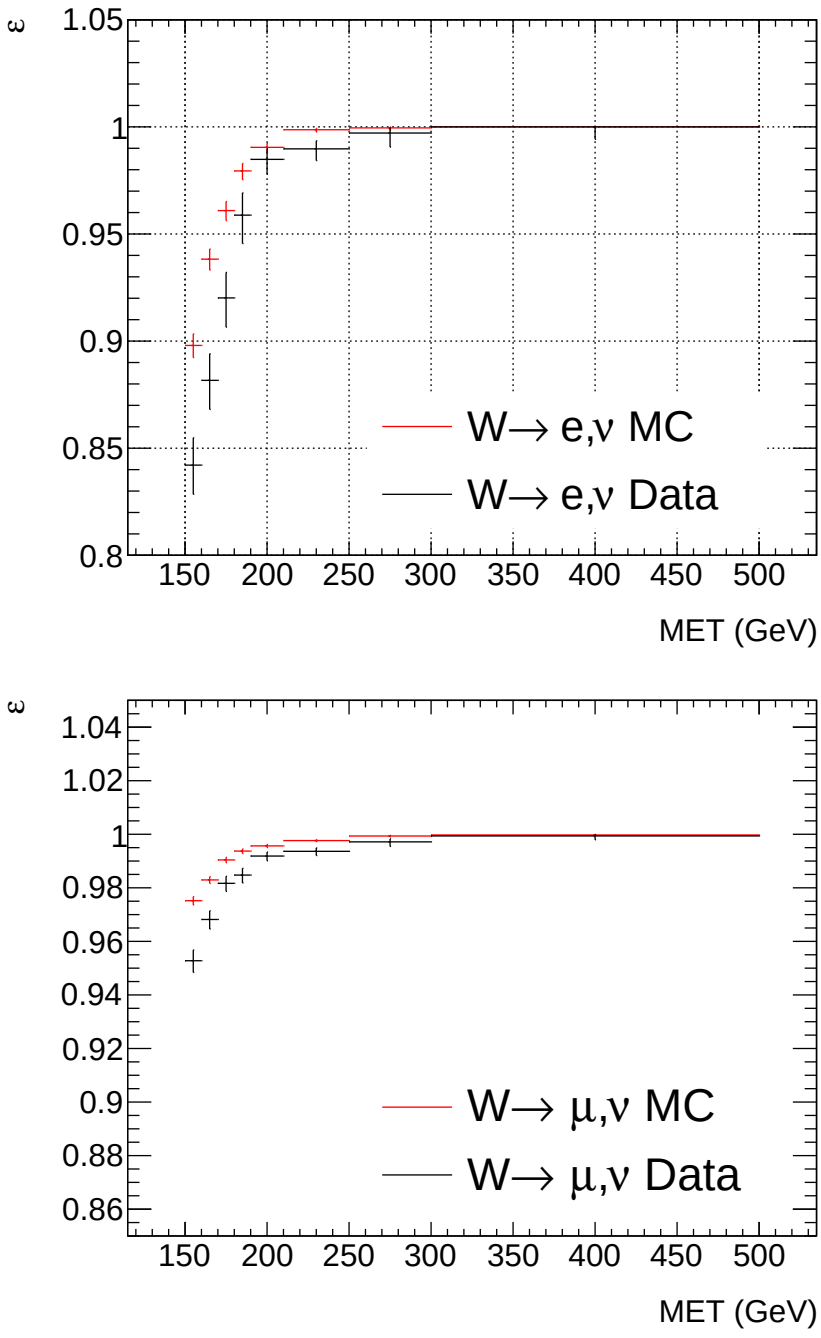

Figure 4.6: The trigger efficiency for the logical or of the two triggers: triggers HLT_xe90_mht_L1XE50 and HLT_xe110_mht_L1XE50, computed with respect to offline $E_{\mathrm{T}}^{\mathrm{miss}}$, shown for signal and $W \to \ell\nu$ MC simulation.

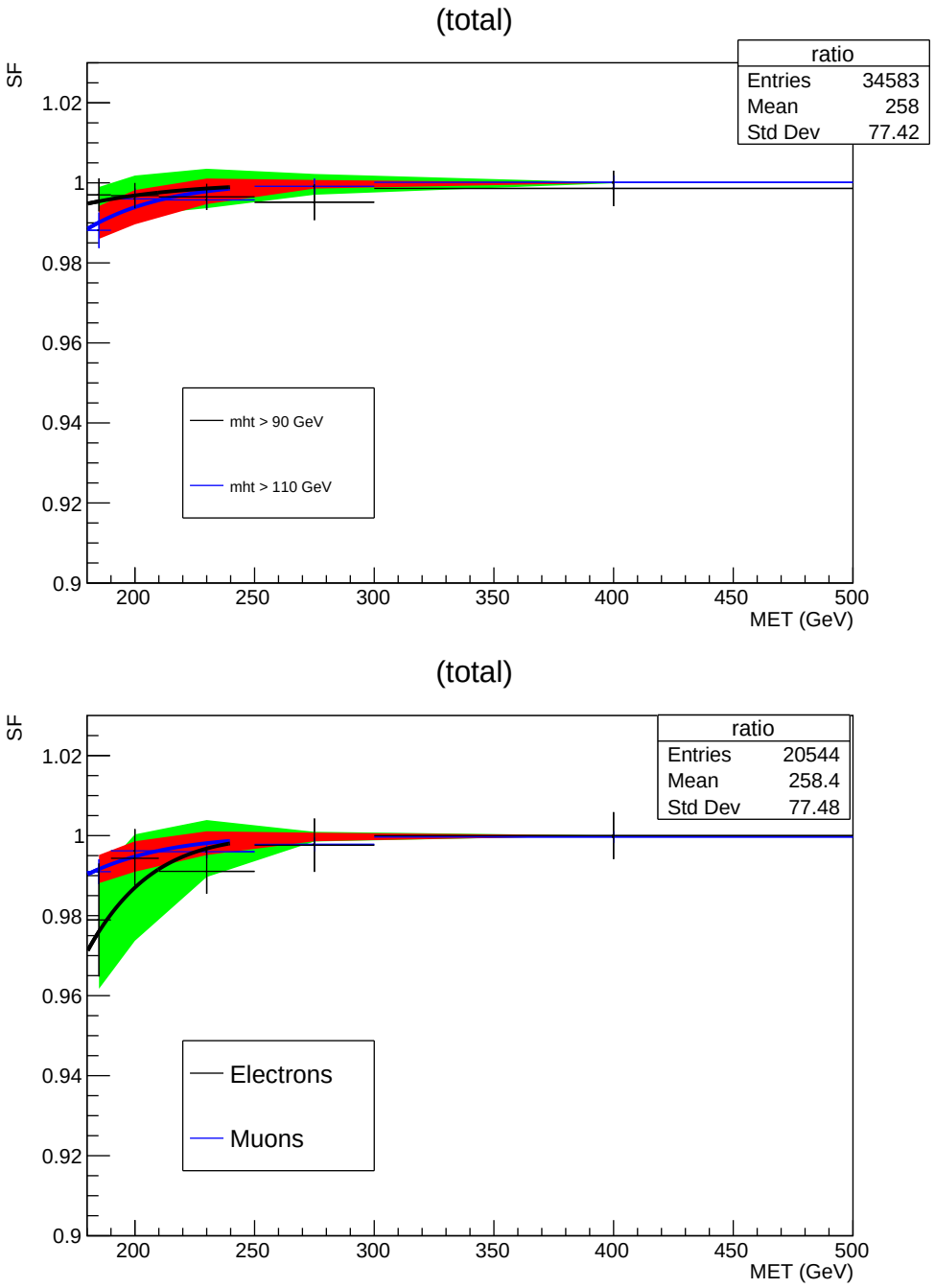

Figure 4.7: The ratio of the efficiency computed in data divided by the efficiency computed in MC, or the trigger MC scale factor. Left: the comparison of the two triggers: HLT_xe90_mht_L1XE50 and HLT_xe110_mht_L1XE50. Right: comparison of the trigger SF computed using an electron and muon selection.

Figure 4.8: Anti-ID scale factor for the identification component, at low p_{T}.

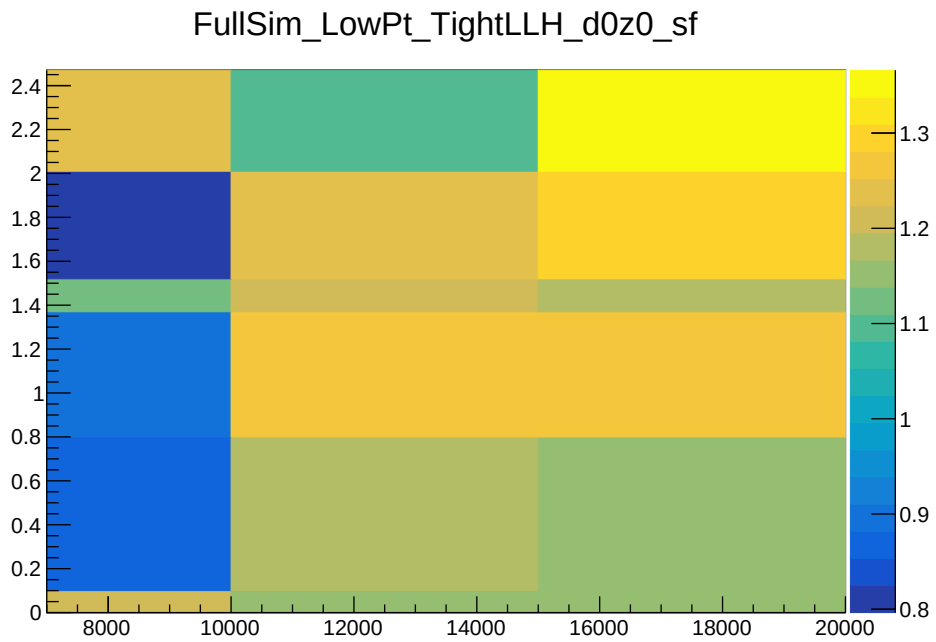

Primary vertex

The primary vertex with the largest Σp_{T}^2 is taken to be the location of the hard-scatter interaction. Only events with a primary vertex with at least two associated tracks with transverse momenta $p_{\mathrm{T}} > 400\mathrm{MeV}$ are selected. This requirement is imposed even if no selected electron, muon, or jet lies within the tracking volume.

Electrons

Electron candidates are reconstructed by matching clustered energy deposits in the electromagnetic calorimeter to tracks reconstructed in the inner detector. To be considered in the analysis, electrons are required to have $p_{\mathrm{T}} > 7\mathrm{GeV}$ and to be within $|\eta| < 2.47$, but not within the transition regions between barrel and endcap EM calorimeters at $1.37 < |\eta| < 1.52$. They must also satisfy object quality requirements encoded in the EGamma BADCLUSELECTRON bitmask and pass the "tight" likelihood based identification criteria. Furthermore, "Gradient" isolation criteria with an efficiency of 90% for true electrons with $p_{\mathrm{T}} > 25\,\mathrm{GeV}$

and 99% for true electrons with $p_{\mathrm{T}} > 60$GeV are applied. In addition, a longitudinal impact parameter requirement of $|z_0 \times \sin\theta| < 0.5$mm as well as a transverse impact parameter requirement of $|d_0|/\sigma(d_0) < 5$ is applied to ensure that the electron track is consistent with having originated at the primary vertex [7].

Muons

Muon candidates are required to contain matching inner-detector and muon-spectrometer tracks. To be considered in the analysis, muons are required to have $p_{\mathrm{T}} > 7$GeV and to be within $|\eta| < 2.5$. They must also pass a set of "medium" track quality criteria. Furthermore, "Gradient" isolation criteria with an efficiency of 90% for true muons with $p_{\mathrm{T}} > 25$GeV and 99% for true muons with $p_{\mathrm{T}} > 60$GeV are applied. In addition, a longitudinal impact parameter requirement of $|z_0 \times \sin\theta| < 0.5$mm as well as a transverse impact parameter requirement of $|d_0|/\sigma(d_0) < 3$ is applied to ensure that the muon track is consistent with having originated at the primary vertex [2, 12].

Jets

Jets are reconstructed from topological clusters in the calorimeters [18, 17] using the anti-k_T algorithm [31] with a size parameter value of $R = 0.4$. Jets are calibrated [8] the latest recommendations, using the configuration file:

- JES_data2016_data2015_Recommendation_Dec2016.config

To be considered in the analysis, jets are required to have $p_{\mathrm{T}} > 25$GeV, with $|\eta| < 4.5$. The Jet Vertex Tagger (JVT) discriminant is used to identify jets originating from the hard-scatter interaction through the use of tracking and vertexing information. Jets with $p_{\mathrm{T}} < 60$GeV and $|\eta| < 2.4$ are required to satisfy the requirement JVT > 0.59, corresponding to a selection efficiency for non-pile-up jets of about 92% [11].

Event cleaning using jets

Jets are "cleaned" to remove events that do not originate from proton-proton collisions, such as non-collision background [14, 58, 15]. Any event where at least one jet fails the jet cleaning requirements after overlap removal and JVT is removed from the selection. The "Tight" working point is used.

$E_{\mathrm{T}}^{\mathrm{miss}}$ and MHT

In the Run 1 analysis [20], the $E_{\mathrm{T}}^{\mathrm{miss}}$ quantity was used as a selection variable. It is defined as the magnitude of the negative vectorial sum of the transverse momenta of all selected electrons, muons, and jets, as well as tracks compatible with the primary vertex but not matched to any of those objects. Jets are only included in the $E_{\mathrm{T}}^{\mathrm{miss}}$ definition if they have $p_{\mathrm{T}} > 20$ GeVand satisfy the medium JVT working point, as recommended by the JetEtMiss group.

$E_{\mathrm{T}}^{\mathrm{miss}}$ is corrected separately in each control sample for the presence of visible leptons, as will be described in the following sections.

To suppress events where "fake" $E_{\mathrm{T}}^{\mathrm{miss}}$ is introduced by the removal one of a pair of pileup jets from the JVT requirement, we define another event-level energy sum denoted MHT, which is the magnitude of the vector sum of the p_{T} of all jets with $p_{\mathrm{T}} > 20$GeV regardless of the JVT requirement. Note that leptons are not included in this definition.

4.3.2 Signal and Control Region selection

This analysis uses Signal Region (SR) and Control Region (CR). CR is used to estimate W/Z backgrounds in the SR (see Section 4.4) and has exactly the same selection and bins as the SR except the trigger and lepton requirements. While events triggered by $E_{\mathrm{T}}^{\mathrm{miss}}$ trigger are selected in SR, events triggered by single lepton trigger are selected.

Signal Regions

We need to select events with the VBF+$E_{\mathrm{T}}^{\mathrm{miss}}$ topology in SR. This means that we should select events triggered by the $E_{\mathrm{T}}^{\mathrm{miss}}$ trigger, with two VBF-like jets (i.e. close in ϕ, largely separated in η) and a large $E_{\mathrm{T}}^{\mathrm{miss}}$. As the results of optimization, the following requirements are applied:

- The event contains no electrons or muons.
- The leading jet has $p_{\mathrm{T}} > 80$GeV.
- The sub-leading jet has $p_{\mathrm{T}} > 50$GeV.
- The event contains exactly two jets, no additional jets with $p_{\mathrm{T}} > 25$GeV.
- The two jets are not back-to-back: $|\Delta\Phi(jj)| < 1.8$.
- The two jets are well separated in η: $|\Delta\eta(jj)| > 4.8$.
- The dijet system has a large invariant mass: $m_{\mathrm{jj}} > 1$TeV.
- The event has $E_{\mathrm{T}}^{\mathrm{miss}} > 180$GeV.
- The event has MHT > 150GeV.
- The two jets are well separated from the $E_{\mathrm{T}}^{\mathrm{miss}}$: $\Delta\Phi(j_1, E_T^{miss}) > 1$ and $\Delta\Phi(j_2, E_T^{miss}) > 1$.

The selected events are then split into three bins of different signal purity according to the invariant mass of the dijet system: SR1 ($1\text{TeV} < m_{\mathrm{jj}} < 1.5\text{TeV}$), SR2: ($1.5\text{TeV} < m_{\mathrm{jj}} < 2\text{TeV}$), and SR3 ($2\text{TeV} < m_{\mathrm{jj}}$).

$W \to \ell\nu$ Control Regions

For each of SR1, SR2, SR3; corresponding $W \to e^{+}\nu$, $W \to e^{-}\nu$, $W \to \mu^{+}\nu$, and $W \to \mu^{-}\nu$ CRs are defined by replacing the $E_{\mathrm{T}}^{\mathrm{miss}}$ trigger with a single lepton trigger and replacing

the lepton veto with a requirement of exactly one electron (electron triggered events) or exactly one muon (muon triggered events). The lepton must have $p_{\mathrm{T}} > 30$GeV in order to be on the single lepton trigger efficiency plateau. A distinction is made between positively and negatively charged leptons in order to discriminate the approximately charge-symmetric multijet background from the charge asymmetric $W + jets$ production in pp collisions (see Section 4.4).

The jet cuts are kept exactly the same as for the events with zero leptons. To make the $E_{\mathrm{T}}^{\mathrm{miss}}$ spectrum similar to the definition in the 0 lepton SR, the $E_{\mathrm{T}}^{\mathrm{miss}}$ is corrected by vectorially adding the lepton p_{T}. The corrected $E_{\mathrm{T}}^{\mathrm{miss}}$ is also used for the requirements $\Delta\Phi(E_T^{miss}, j_1) > 1$ and $\Delta\Phi(E_T^{miss}, j_2) > 1$.

$W \to e\nu$ Control Region

To suppress the contribution from misidentified leptons, in the $W \to e\nu$ we add an additional requirement that the $E_{\mathrm{T}}^{\mathrm{miss}}$ sig $> 4.0\sqrt{\mathrm{GeV}}$, where $E_{\mathrm{T}}^{\mathrm{miss}}$ sig is defined as:

$$E_{\mathrm{T}}^{\mathrm{miss}} \text{ sig} = \frac{E_{\mathrm{T}}^{\mathrm{miss}}}{\sqrt{p_{\mathrm{T}}(j1) + p_{\mathrm{T}}(j2) + p_{\mathrm{T}}(el)}}. \tag{4.2}$$

The denominator of this expression contains the p_{T} of the two VBF tag jets and the electron p_{T}, and the variable is designed to remove events that have large $E_{\mathrm{T}}^{\mathrm{miss}}$ as a result of a jet that is misidentified as an electron. Note that in eq. 4.2, the $E_{\mathrm{T}}^{\mathrm{miss}}$ value in the numerator is the $E_{\mathrm{T}}^{\mathrm{miss}}$ before correcting using the visible lepton. The $E_{\mathrm{T}}^{\mathrm{miss}}$ significance distribution in $W \to e\nu$ events and $E_{\mathrm{T}}^{\mathrm{miss}}$ distribution before and after $E_{\mathrm{T}}^{\mathrm{miss}}$ significance> 4 cut are shown in figure 4.9. We can see that the $E_{\mathrm{T}}^{\mathrm{miss}}$ significance $> 4\sqrt{\mathrm{GeV}}$ removes the misidentified electron contribution. Data are well modeled by the MC simulation after the misidentified lepton background is removed.

Figure 4.9: The $E_{\mathrm{T}}^{\mathrm{miss}}$ significance distribution in the $W \to e\nu$ CR, before the $E_{\mathrm{T}}^{\mathrm{miss}}$ sig $> 4.0\sqrt{\mathrm{GeV}}$. $E_{\mathrm{T}}^{\mathrm{miss}}$ distribution in $W \to e\nu$ CR before and after $E_{\mathrm{T}}^{\mathrm{miss}}$ significance $> 4\sqrt{\mathrm{GeV}}$ cut. (for 2016 data, $\sim$33 fb^{-1}).

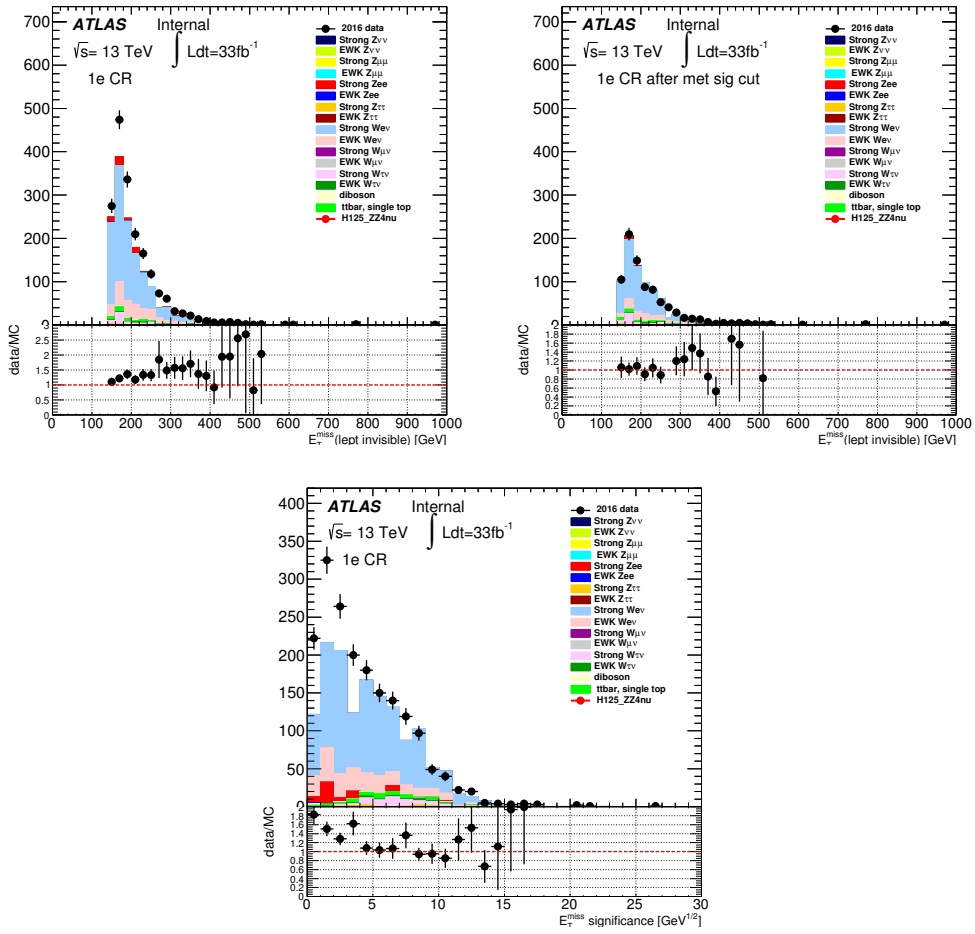

Table 4.4: List of all selection criteria for SRs and CRs

Cut	*inv.*	$W \to e^-\nu$	$W \to e^+\nu$	$W \to \mu^-\nu$	$W \to \mu^+\nu$	$Z \to e^-e^+$	$Z \to \mu^-\mu^+$
Trigger	$E_{\mathrm{T}}^{\mathrm{miss}}$	Single lepton					
Leptons	0	e^-	e^+	μ^-	μ^+	e^-, e^+	μ^-, μ^+
$p_{\mathrm{T}}(\ell_1)$	–	> 30GeV	> 30GeV	> 30GeV	> 30GeV	> 30GeV	> 30GeV
ℓ_1	–	Tight	Tight	Medium	Medium	Tight	Medium
$p_{\mathrm{T}}(\ell_2)$	–	–	–	–	–	> 18GeV	> 7GeV
$\lvert M_{\ell\ell} - M_Z \rvert$	–	–	–	–	–	< 25GeV	< 25GeV
$E_{\mathrm{T}}^{\mathrm{miss}}$	> 180 GeV	> 180 GeV (leptons invisible)					
	Loose						
MHT	> 150 GeV						
e/μ veto	$p_{\mathrm{T}} < 7(7)$ GeV						
Jet p_{T}	$> 80(50)$ GeV						
$\Delta\Phi_{\mathrm{j}E_{\mathrm{T}}^{\mathrm{miss}}}$	> 1.0						
$\Delta\eta_{\mathrm{jj}}$	> 4.8						
Njets	$= 2$ (3rd < 25 GeV)						
$\Delta\Phi_{\mathrm{jj}}$	< 1.8						
m_{jj}	$1 - 1.15, 1.5 - 2, > 2$ TeV						

$Z \to \ell\ell$ Control Regions

For each m_{jj} bin of SRs, corresponding $Z \to ee$ and $Z \to \mu\mu$ CRs are defined by replacing the $E_{\mathrm{T}}^{\mathrm{miss}}$ trigger requirement with a single lepton trigger and replacing the lepton veto with a requirement of exactly two electrons (electron triggered events) or exactly two muons (muon triggered events). The leading lepton must have $p_{\mathrm{T}} > 30$GeV in order to be on the single lepton trigger efficiency plateau. The two selected leptons must have an opposite electric charge and an invariant mass within 25GeV of the Z boson mass, 91.2GeV. Furthermore, the subleading electron must have $p_{\mathrm{T}} > 18$ GeV due to a bug in the derivation which only affects the $Z \to ee$ CR.

The jet cuts are kept exactly the same as for the events with zero leptons. To make the $E_{\mathrm{T}}^{\mathrm{miss}}$ definition similar to the definition in the 0 lepton SR, the $E_{\mathrm{T}}^{\mathrm{miss}}$ is corrected by vectorially adding the p_{T} of both leptons. The corrected $E_{\mathrm{T}}^{\mathrm{miss}}$ is also used for the requirements $\Delta\Phi(E_T^{miss}, j_1) > 1$ and $\Delta\Phi(E_T^{miss}, j_2) > 1$.

Table 4.4 summarizes the selection criteria of both SRs and CRs.

4.4 Background estimation

This section provides a conceptual overview of the background estimation procedure, including the major W/Z background, multijet background and the fake lepton background in $W \to e\nu$ CR.pre-fit distributions in each control sample.

4.4.1 $Z \to \nu\nu$ and $W \to \ell_{lost}\nu$

The major backgrounds in the SRs are $Z \to \nu\nu$+jets and $W \to \ell_{\text{lost}}\nu$+jets events, where ℓ_{lost} indicates a charged lepton not present as a reconstructed lepton passing the object selection described in Section 4.3.1. Leptons are "lost" either because they fall outside of the p_{T} or η acceptance or because they failed to be detected due to the reconstruction or detector efficiency.

Modeling the major backgrounds, $Z \to \nu\nu$ and $W \to \ell\nu$, with MC simulation alone would give too large a theoretical uncertainty as well as a significant detector modeling uncertainty (such as the jet energy scale); therefore, in order to estimate these backgrounds, we use Control Regions (CR) consisting of $Z \to \ell\ell$ or $W \to \ell\nu$ events ($\ell = e/\mu$). In each of these CRs, the same jet and $E_{\text{T}}^{\text{miss}}$ requirements as the SRs are placed with different lepton requirements. Leptons are treated as invisible in $E_{\text{T}}^{\text{miss}}$ calculation in CRs to resemble the W/Z backgrounds in SR. See Section 4.3.1 for detailed selection criteria in each CR. In $W \to e\nu$ CR, the background from jets misidentified as electrons is not negligible. This background, which we all the fake lepton background, is normalized using a fit that takes advantage of the distinctive shape of the $E_{\text{T}}^{\text{miss}}$ significance, and the charge asymmetry in W^+/W^- events.

In order to use the CRs rather than the MC predictions for setting the W+jets and Z+jets background normalizations, the MC predictions in each of the three m_{jj} bins in the corresponding W/Z CRs are scaled by free parameters $k_{i,W}$ ($k_{i,Z}$), where i refers to the index of three m_{jj} bins. The corrections are calculated separately for each bin of m_{jj}, as well

as for W and Z. The W/Z background normalizations are summarized in the expression below, where the m_{jj} indices have been dropped. The scale factors ks are determined from the maximum profile likelihood fit described in Section 4.6. The $Z(\to \ell\ell)$+jets and the $W(\to \ell\nu)$+jets MC predictions affect the final estimates of $Z(\to \nu\nu)$+jets and $W(\to \ell\nu)$+jets in the signal region through an implicit dependence on the MC ratio $Z_{\mathrm{SR}}/Z_{\mathrm{CR}}$ and $W_{\mathrm{SR}}/W_{\mathrm{CR}}$:

$$
\begin{aligned}
Z_{\mathrm{SR}} &\sim \frac{Z_{\mathrm{SR}}^{\mathrm{MC}}}{Z_{\mathrm{CR}}^{\mathrm{MC}}} \times Z_{\mathrm{CR}}^{\mathrm{data}} = \frac{Z_{\mathrm{CR}}^{\mathrm{data}}}{Z_{\mathrm{CR}}^{\mathrm{MC}}} \times Z_{\mathrm{SR}}^{\mathrm{MC}} = k_Z \times Z_{\mathrm{SR}}^{\mathrm{MC}}, \\
W_{\mathrm{SR}} &\sim \frac{W_{\mathrm{SR}}^{\mathrm{MC}}}{W_{\mathrm{CR}}^{\mathrm{MC}}} \times W_{\mathrm{CR}}^{\mathrm{data}} = \frac{W_{\mathrm{CR}}^{\mathrm{data}}}{W_{\mathrm{CR}}^{\mathrm{MC}}} \times W_{\mathrm{SR}}^{\mathrm{MC}} = k_W \times W_{\mathrm{SR}}^{\mathrm{MC}}.
\end{aligned} \tag{4.3}
$$

The technical procedure is performed using a simultaneous fit of the k parameters in all regions (see Section 4.6). Using bins of m_{jj} and $\Delta\phi(j,j)$ adds sensitivity and robustness to the analysis as the signal-to-background ratio (S/B) varies significantly over the m_{jj} and $\Delta\phi(j,j)$ distribution. Individual normalization factors are applied to each m_{jj} selection, hence no assumption on the correctness of neither the absolute normalization nor the m_{jj} shape in the simulated events is made.

4.5 Systematic uncertainties

This section describes the systematics included in the analysis, both the experimental uncertainties due to mis-measurement of physics objects and theoretical uncertainties due to MC modellings.

4.5.1 Experimental uncertainties

The experimental uncertainties in the analysis are tabulated below.

Jets and $E_{\mathrm{T}}^{\mathrm{miss}}$

The impact of the uncertainties related to jets is accounted for by varying each uncertainty according to the recommendations [9].

The impact of the $E_{\mathrm{T}}^{\mathrm{miss}}$ systematic uncertainty is taken into account by following the recommendations [10].

Since the $E_{\mathrm{T}}^{\mathrm{miss}}$ of an event is calculated as the sum of different terms (Sec. 4.3.1), the uncertainties for the various objects used in the analysis needs to be propagated to the $E_{\mathrm{T}}^{\mathrm{miss}}$: the uncertainties provided for electrons, muons and jets are propagated into their respective $E_{\mathrm{T}}^{\mathrm{miss}}$ terms while the systematic uncertainties for the $E_{\mathrm{T}}^{\mathrm{miss}}$ track soft term are derived separately.

The $E_{\mathrm{T}}^{\mathrm{miss}}$ track soft term uncertainties accounts for the response ($E_{\mathrm{T}}^{\mathrm{miss}}$ scale) and for the $E_{\mathrm{T}}^{\mathrm{miss}}$ resolution arising from the soft term. These uncertainties are evaluated from data-to-MC comparisons of distributions of observables which are sensitive to the balance between the soft term and the hard activity. These observables are the parallel and perpendicular projections of the soft term transverse momentum ($p_{\mathrm{T}}^{\mathrm{soft}}$) onto the transverse momentum of the hadronic recoil system ($p_{\mathrm{T}}^{\mathrm{hard}}$) [10].

- **JET_GroupedNP,JET_EtaIntercalibration_NonClosure**, etc: 29 nuisance parameter set that account for the uncertainty on the knowledge of the jet energy scale (JES).
- **JET_JER_SINGLE_NP**: accounts for the uncertainty on the knowledge of the jet energy resolution.
- **JET_JvtEfficiency**: accounts for the uncertainty on the efficiency of the JVT efficiency.
- **MET_SoftTrk_Scale**: accounts for the $E_{\mathrm{T}}^{\mathrm{miss}}$ track soft term scale uncertainty;

Table 4.5: Cutflow table of cut efficiency with JES and JER uncertainties for $m_{\mathrm{jj}} > 1$ TeV(combining SR1-3) is shown for signal. Table includes: absolute ϵ: absolute cut efficiency: the total number of selected events at each stage of cutflow over initial number of events, relative ϵ: relative cut efficiency: total number of selected events over the number of selected events before the specific cut, and the variations with respect to nominal relative cut efficiency for each systematic. EtaICal: JET_EtaIntercalibration_NonClosure. NP1, NP2, NP3: JET_GroupedNP_1, JET_GroupedNP_2, JET_GroupedNP_3. SNP: JET_JER_SINGLE_NP. While the full limit calculation utilizes all 29 nuisance parameters, here we use the reduced set to simplify the presentation.

Unit: %	absolute ϵ	relative ϵ	EtaICal	NP1	NP2	NP3	SNP
Trigger	30.4 ± 0.2	30.4 ± 0.2	0.0 ± 0.8	0.0 ± 0.8	0.0 ± 0.8	0.0 ± 0.8	0.0 ± 0.8
jet p_Ts	12.9 ± 2.6	50.4 ± 0.4	0.1 ± 0.1	3.5 ± 1.1	0.5 ± 1.0	1.5 ± 1.0	0.2 ± 1.0
$\Delta\eta(j,j) > 4.8$	3.9 ± 0.3	29.9 ± 0.3	0.4 ± 1.7	1.8 ± 1.7	0.4 ± 1.7	2.1 ± 1.7	0.6 ± 1.6
$\eta_{j1} \times \eta_{j2} < 0$	3.9 ± 0.2	100.0 ± 1.8	0.0 ± 2.5	0.0 ± 2.6	0.0 ± 2.5	0.0 ± 2.5	0.0 ± 2.5
$\mathrm{mass}_{jj} > 1$ TeV	3.6 ± 0.2	93.7 ± 1.6	0.4 ± 2.4	0.5 ± 2.5	0.1 ± 2.4	0.3 ± 2.4	0.5 ± 2.5
$\Delta\phi(j,j) < 1.8$	2.5 ± 0.1	67.9 ± 1.0	0.5 ± 2.1	1.2 ± 2.1	0.3 ± 2.1	0.7 ± 2.1	0.0 ± 2.2
j3 $p_T < 25$ GeV	1.6 ± 0.1	63.4 ± 1.9	0.6 ± 2.1	6.8 ± 2.2	1.0 ± 2.1	2.4 ± 2.1	4.5 ± 2.2
$\Delta\phi(j, E^{\mathrm{miss}}) > 1$	1.6 ± 0.1	100.0 ± 2.0	0.0 ± 2.8	0.0 ± 2.8	0.0 ± 2.8	0.0 ± 2.8	0.0 ± 3.1
lepton veto	1.6 ± 0.1	100.0 ± 2.0	0.0 ± 2.8	0.0 ± 2.8	0.0 ± 2.8	0.0 ± 2.8	0.0 ± 3.1
$E^{\mathrm{miss}} > 150$ GeV	1.1 ± 0.0	73.2 ± 1.2	1.1 ± 2.4	1.1 ± 2.4	0.1 ± 2.3	0.3 ± 2.4	0.7 ± 2.6

- **MET_SoftTrk_ResoPara**: accounts for the $E_{\mathrm{T}}^{\mathrm{miss}}$ track soft term resolution uncertainty (evaluated from the soft term projection parallel to the p_{T} of the hadronic recoil system);

- **MET_SoftTrk_ResoPerp**: accounts for the $E_{\mathrm{T}}^{\mathrm{miss}}$ track soft term resolution uncertainty (soft term projection perpendicular to the p_{T} of the hadronic recoil system).

A summary of the impact of the jet uncertainties on signal sample is given in Table 4.5. The third jet veto introduces the largest dependence on the jet related uncertainties in the analysis.

Electrons and muons

- **MUON_EFF_SYS**: accounts for the systematic component on the muon identification scale factors.

- **MUON_EFF_STAT**: accounts for the statistical component on the muon identifi-

cation scale factors.

- **MUON__EFF__TrigStatUncertainty**: accounts for the muon trigger uncertainty.
- **MUON__ID**: accounts for the muon identification uncertainty.
- **MUON__MS**: accounts for the muon spectrometer track associated to the muon.
- **MUON__SCALE**: accounts for the uncertainty on the muon momentum scale.
- **MUON__SAGITTA__RESBIAS**: accounts for the variations in the momentum scale based on residual charge-dependent bias after correction.
- **MUON__SAGITTA__RHO**: accounts for variations in the scale of the momentum based on corrections using the Z.
- **MUON__TTVA__STAT**: accounts for the statistical component of the track-to vertex association uncertainties.
- **MUON__TTVA__SYS**: accounts for the systematic component of the track-to vertex association uncertainties.
- **EG__RESOLUTION__ALL**: accounts for the uncertainty on the knowledge of the electron/photon energy scale.
- **EG__SCALE__ALL**: accounts for the uncertainty on the knowledge of the electron/photon energy scale.
- **EL__EFF__ID__TOTAL__1NPCOR__PLUS__UNCOR**: accounts for the uncertainty on the knowledge of the electron identification efficiency scale factors.
- **EL__EFF__Reco__TOTAL__1NPCOR__PLUS__UNCOR**: accounts for the uncertainty on the knowledge of the electron reconstruction efficiency scale factors.

- **EL_EFF_ISO**:accounts for the uncertainty on the knowledge of the electron isolation efficiency scale factors.

- **EL_EFF_TriggerEff_TOTAL_1NPCOR_PLUS_UNCOR**: accounts for the uncertainty on the knowledge of the trigger efficiency.

These nuisance parameters are used in the fit (described in Sec. 4.6) to take into account the impact of the $E_{\mathrm{T}}^{\mathrm{miss}}$ systematic uncertainties on the signal and background yields in the Signal Region and in the different Control Regions.

Pileup

- **PRW_DATASF**: accounts for the uncertainty on the ratio between the predicted and measured inelastic cross-section in the fiducial volume.

4.5.2 Theoretical Uncertainties on the Backgrounds

In addition to detector systematics, there are uncertainties originating from the finite precision of the MC simulation. These affect the MC predictions of yields for both signal and background processes. These uncertainties arise from fixed scale choices in the event generation, as well as our description of the initial-state PDF and parton shower.

For the W/Z background MC (which is all Sherpa), there are 4 scales which are fixed during event generation: the renormalization, factorization, resummation (sometimes denoted *"qsf"*), and CKKW matching scales. To estimate the uncertainties associated with these choices, events are generated with each of these scales varied up or down by a factor of 2. The CKKW matching scale is an exception; its nominal value is 20 GeV and is varied to 15 and 30 GeV. For the factorization and renormalization scales, these uncertainties can be calculated using on-the-fly varied event weights in the reconstructed Sherpa MC. This results in full statistical correlation between the varied and nominal samples. The corresponding uncertainties are calculated by taking an envelope of the 7-point factorization/renormalization

scale variations (the central value, each scale independently varied up/down, and both scales coherently varied up/down). In most cases, the largest variation comes from both scales being simultaneously varied.

For the resummation and CKKW merging scales, separate varied samples need to be generated. Due to computing resource limitations, these cannot be reconstructed. So, the effect of the variations is determined at truth level and used to define a reweighting which is then applied to the fully-reconstructed nominal sample. These are defined as half the difference between the up- and down-varied yields at truth-level. As such, they are symmetrized, unlike the factorization/renormalization scale variations. Due to statistical limitations, the statistical uncertainty on the size of these variation is sometimes larger than the variation itself. In these cases, the maximum of the two is used as the uncertainty on the yield. The results of the variations for the factorization/renormalization, resummation, and CKKW scales are given in

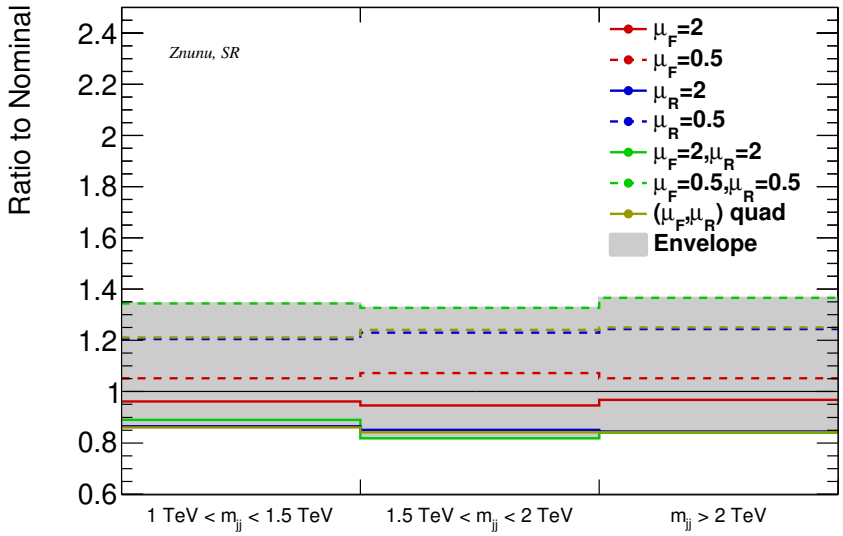

Figure 4.10: Factorization and renormalization scale variations for the strong $Z \to \nu\nu$ process.

For the PDF uncertainties on the W/Z background, we evaluate the background yield predictions with a full ensemble of 100 PDFs within the NNPDF set. The standard deviation

of this set of yields is taken to be the corresponding PDF uncertainty. These uncertainties are evaluated separately in each signal and control region. Since the full ensemble of PDF weights is stored for each event in the main Monte Carlo samples, this procedure can be carried out directly on fully reconstructed simulation. The results are given in Table **??**.

All theoretical uncertainties are assumed to be uncorrelated between strong and electroweak processes. Additionally, no correlation is assumed between W and Z processes (this is in line with using separate normalization factors k_W and k_Z in the fit). No correlation is assumed across m_{jj} bins either; the variations are carried out independently in each one. Full correlation *is* assumed between the signal and control regions for a given process (for example, strong Z+jets in the SR and strong Z+jets in the $2e$ CR). This is what allows the CRs to constrain the background yield in the SR.

4.5.3 Theoretical Uncertainties on the Signal

Higgs parton shower uncertainties

We followed the recommendations in [6] to evaluate the parton shower uncertainties on the signal.

We showered the LHE files using the following variations using Pythia.

- VAR1: corresponds to the parameters used to describe the underlying event and multi-parton interactions.
- VAR2: corresponds to variations of parameters used in the initial and final state showers.
- MPI: Multi-parton interaction cutoff scale.
- Ren: Renormalization scale for the ISR/FSR jet.

In addition, the same events were showered using Herwig. The largest difference from the nominal was taken as the systematic uncertainty.

Table 4.6: Table showing the variations with respect to nominal for each parton shower variation

Generator variation	Difference from nominal configuration
Herwig	-7.7%
RenUp	-0.5%
RenDown	-0.4%
MPIUp	0.1%
MPIDown	-0.1%
Var1Up	-0.1%
Var1Down	0.2%
Var2Up	-0.01%
Var2Down	-0.07%

Table 4.6 shows the difference between variations is dominated by the Herwig to Pythia difference, and assigned as a 7.7% uncertainty on the Higgs signal. Figure 4.11 compares some distributions between Herwig and Pythia.

Figure 4.11: Efficiency per bin, normalized to the number of generated events, comparing the differences between Herwig and Pythia. As expected, there are substantial differences between Herwig and Pythia in all quantities related to jets. On the other hand, the $E_{\mathrm{T}}^{\mathrm{miss}}$ distribution, defined only by the p_{T} of the Higgs independent of the showering used.

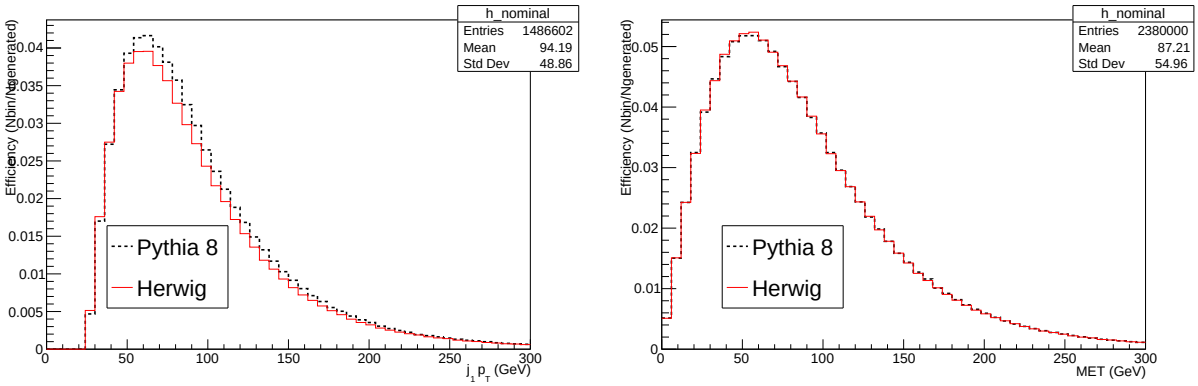

Electroweak corrections to VBF Higgs production

The electroweak corrections to the Higgs Pt distribution were not included when the signal samples were generated. A correction must therefore be evaluated as a function of the transverse momentum of the Higgs. The Monte Carlo integrator program HAWK [41] allows

the calculation of differential EW correction factors that can be applied as reweighting factors to events from a QCD-based generator.

Since, according to the HAWK authors, approximately 10^9 events must be generated to achieve accurate reweighting factors, a multi-threaded version of HAWK was used to reduce execution time. The relevant input parameters to HAWK for VBF Higgs production were set with the same jet Pt, rapidity, and jet-jet invariant mass cuts as applied to select signal events in the analysis.

The results of HAWK, given as a correction factor as a function the Higgs Pt, are shown in Figure 4.12.

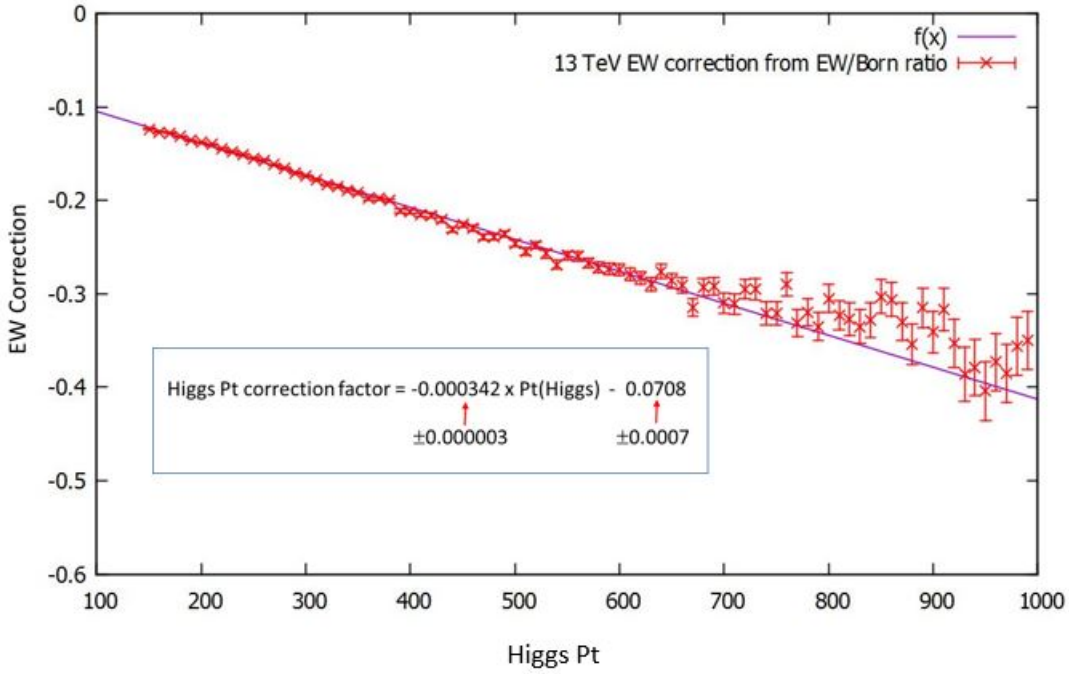

Figure 4.12: Higgs Electroweak correction factor in % for VBF Higgs production.

The data in Figure 4.12 were subjected to a linear fit, resulting in the following formula for the correction:

$$\delta w(\%) = -0.000342(\pm 0.000003) \times p_{\mathrm{T}}(H) - 0.0708(\pm 0.0007). \tag{4.4}$$

Note that in this case, the correction δw is negative. The corrected event weight is then

Table 4.7: The nominal yield after all analysis selections, and the yield after corrections. The difference between the corrected yield and nominal yield, shown in percent, is also shown.

m_{jj}	Nominal yield	Corrected yield	Difference: $\frac{\text{Corrected}-\text{Nominal}}{\text{Corrected}}$
$>$ 1.0 TeV(Inclusive bin)	1063.5	1060.8	-0.26%
1–1.5 TeV	297.0	296.1	-0.30%
1.5–2.0TeV	308.5	307.8	-0.23%
$>$2.0 TeV	458.1	456.9	-0.26%

given by,

$$w_{corrected} = w \cdot (1 + \delta w). \tag{4.5}$$

This factor is applied as a reweighting correction to the nominal VBF signal sample. The impact on the nominal signal yield is shown in Table 4.7.

PDF Uncertainties on the VBF Signal

The evaluation of the uncertainty arising from the use of our chosen PDF set used a sample of 60K signal events generated with Powheg 19.2.5.5 and the NNPDF set NNPDF30_nlo_as_0118, which has 100 replicas. The events were reconstructed in "Truth" mode and the standard signal event selection applied to the Reco derivation output. Approximately 3% of events pass the full selection. The selection efficiency was taken as the ratio of the sum of the weights for events passing the event selection to the sum of the weights for the whole generated event sample. The signal selection efficiency was evaluated for each of the 100 replicas. The distribution of the selection efficiencies and the results of a Gaussian fit are shown in Figure 4.13 for three intervals of $M(jj)$. The final systematic uncertainty on the signal yield is 0.64% for 1.0$<$ m_{jj} $<$ 1.5, 1.02% for 1.5$<$ m_{jj} $<$ 2.0, and 1.53% for m_{jj} $>$ 2.0. These results were evaluated from the sigma over mean of the Gaussian for each plot.

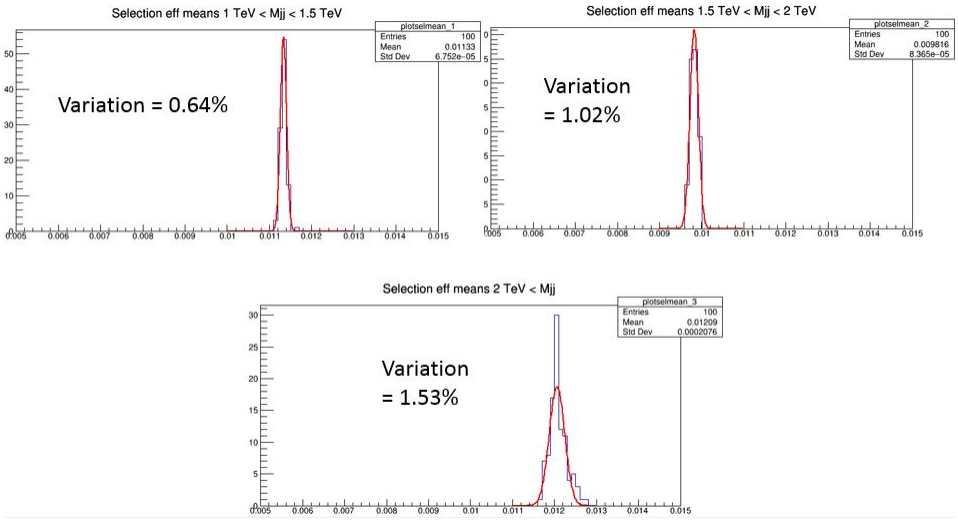

Figure 4.13: VBF signal selection variations for three M(jj) bins (as indicated) with the replicas in the NNPDF nlo pdf set.

Jet Bin Uncertainty on ggF Signal

The Higgs production mechanism in ggF+nJets is sensitive to scale variations. Furthermore, the fraction of the events in ggF+0/1/2 jets is senstive to the cuts applied (jet bin migration). We estimate the jet bin uncertainty on the ggF+2 jets using the Steward-Tackmann(ST) procedure [60]. This procedure typically produces uncertainies larger than the directly scale variation in each jet bin. It also give better estimate of the jet bin uncertainties for the process where the higher order corrections are sizable (the ggF process for example).

We generated ggF+2jets in MCFM [32] using process ID=270. We take the Higgs p_T as missing energy, and we vary the factorization (μ_F) and renormalization (μ_R) scales independently for seven scale settings: the central scale ($\mu_F = \mu_R = m_H$), and 6 independent variations of μ_F and μ_R around the central scale. We applied the VBF selection discussed in Section 4.3. The ST procedure consists of:

- evaluating the uncertainty on the central jet veto at the level of the jet selection. This is done by calculating the inclusive 2-jet cross section and subtracting the 3-jet cross section.

- applying all the cuts including the central jet veto and calcuting the uncerainty due to the additional cuts.

- finally adding the two uncertainties in quadrature.

Table 4.8 shows the jet selection cross sections and the accepances of the all cuts as a function of the scale variaion. The ST procedure leads to uncertainties of 68% on the ggF+2 jets in the VBF selection.

μ_F, μ_R	Jet selection cross section (fb)	Acceptance No 3rd jet veto	Acceptance 3rd jet veto only
m_H, m_H	14.06	2.7×10^{-4}	3.7×10^{-2}
m_H, $0.5 \times m_H$	13.90	3.0×10^{-4}	3.7×10^{-2}
m_H, $2.0 \times m_H$	14.92	3.7×10^{-4}	3.8×10^{-2}
$0.5 \times m_H$, m_H	14.77	3.1×10^{-4}	2.7×10^{-2}
$2.0 \times m_H$, m_H	12.72	3.6×10^{-4}	4.2×10^{-2}
$2.0 \times m_H$, $2.0 \times m_H$	12.69	1.2×10^{-4}	2.3×10^{-2}
$0.5 \times m_H$, $0.5 \times m_H$	12.68	3.4×10^{-4}	4.3×10^{-2}
Uncertainty(%)	9.7	55.6	37.8

Table 4.8: The second column shows the inclusive 2-jet cross section with the 3-jet cross section subtracted, with jet selection cuts. The third colums shows the acceptance of all the cuts (except for the third jet veto cut) as a function of scale variation. The last column showns the acceptance variation for the third jet veto only. To avoid large statistical fluctuations when all the cuts are imposed, the acceptances are computed with and without applying the third jet veto cut as shown in the last two columns of the table. The uncertainty of each column is obtained as the maximum deviation from the central scale. Applying the ST procedure, the jet bin uncertainty $\sqrt{9.7^2 + 55.6^2 + 37.8^2} = 67.8\%$ for the 2-jet bin selection on the ggF process.

4.6 Fit Model

The upper limit on the branching ratio of Higgs boson decaying invisibly is calculated using a maximum profiled likelihood fit. The limit is set at 95% CL using asymptotic formulae for a CLs frequentist approach. The likelihood function is constructed from the observed events in data, the yields of signal and backgrounds taken from MC predictions, scaled by free parameters, and nuisance parameters to account for statistical uncertainty terms as well as the systematic uncertainties (see Section 4.5 for details of major systematics uncertainties). In our analysis there are O(100) nuisance parameters. We assume the value of the Standard Model Higgs production cross section, but no explicit dependence on other Higgs decay branching ratios. The fit estimates the normalization correction factors k_W and k_Z that apply to the W and Z background in the signal region using the control region data, the normalization of the misidentified electron backgrounds in the $W \to e\nu$ control regions and the signal strength μ.

Traditionally, this was done using pseudo-experiments (toys) in which the nuisance parameters/auxiliary measurements were randomized within their uncertainties, and events were generated from the template of the full statistical model. However, this procedure is phenomenally expensive computationally. For large-N datasets, asymptotic methods are used to calculate the number of standard deviations without generating millions of toy datasets. The trick is to define an Asimov dataset that, if used as the estimator for any parameter, yields the true parameter [**Asimov**]. This is effectively a perfect dataset, without any statistical fluctuations. It is then possible to derive the variance on the parameter of interest either by solving for the covariance matrix using the properties of the Asimov dataset and the known properties of the test statistic.

Table 4.9: Table showing the free parameters of the fit model: μ, k_W, k_Z, and β for one bin of m_{jj}. The same fit is repeated for the other two bins.

Region	SR	$Z \to ee$	$Z \to \mu\mu$	$W \to e\nu$	$W \to e\nu$	$W \to \mu\nu$	$W \to \mu\nu$	$W \to e\nu$	$W \to e\nu$
N leptons	0	2	2	1	1	1	1	1	1
lepton charge				+	−	+	−	+	−
$E_{\mathrm{T}}^{\mathrm{miss}}$ sig				$> 4\sqrt{GeV}$	$> 4\sqrt{GeV}$			$< 4\sqrt{GeV}$	$< 4\sqrt{GeV}$
Signal	$\mu \times S_1$	-	-	-	-	-	-		
Z + jets	$k_Z \times B_Z$	$k_Z \times B_Z$	$k_Z \times B_Z$	$k_Z \times B_Z$	$k_Z \times B_Z$	$k_Z \times B_Z$	$k_Z \times B_Z$	$k_Z \times B_Z$	$k_Z \times B_Z$
W + jets	$k_W \times B_W$	$k_W \times B_W$	$k_W \times B_W$	$k_W \times B_W$	$k_W \times B_W$	$k_W \times B_W$	$k_W \times B_W$	$k_W \times B_W$	$k_W \times B_W$
ttbar	from MC	from MC	from MC	from MC	from MC	from MC	from MC	from MC	from MC
multijet/fakes	R+S	-	-	$\beta^{ele,fake}$	$\beta^{ele,fake}$			$R \times \beta^{ele,fake}$	$R \times \beta^{ele,fake}$

4.6.1 General description

The inputs and free parameters are summarized in Table 4.9, where each variable is listed as bullet points below. The table only shows the free parameters for one m_{jj} bin for simplicity, as the same fit model is repeated for the other m_{jj} bins. Note that the one exception to this point is that the same μ applies for all three m_{jj} bins.

- μ: signal strength.
- k_W: W normalization, extracted from the fit.
- k_Z: Z normalization, extracted from the fit.
- B_W: Number of W events in a given bin expected from MC.
- B_Z: Number of Z events in a given bin expected from MC.
- β: Number of expected events from misidentified $W \to e\nu$, determined by the fit.
- R: Ratio of events with high to low $E_{\mathrm{T}}^{\mathrm{miss}}$ sig computed using the anti-ID control sample.
- The multijet background in the signal regions is estimated with the rebalance+smear technique.
- The contributions from ttbar, s- and t-channel single t, and Wt events are taken directly from the simulated events.

By performing a simultaneous fit of simulated $Z \to \ell\ell$ and $Z \to \nu\nu$ events to data, during which the strength of both processes is scaled with a common normalization factor, a data-driven estimate of the $Z \to \nu\nu$ background in the signal regions can be obtained while relying on the simulation to accurately model the effects of the lepton selection.

The number of events with misidentified leptons in the $W \to \ell\nu$ control regions are estimated by fitting to the $E_{\mathrm{T}}^{\mathrm{miss}}$ sig distribution. To accomplish that fit, the $W \to \ell\nu$ control regions are split by the charge of the leptons and adding the low $E_{\mathrm{T}}^{\mathrm{miss}}$ sig $W \to \ell\nu$ control regions (low here to differentiate from the main $W \to \ell\nu$ control regions which satisfy high $E_{\mathrm{T}}^{\mathrm{miss}}$ sig requirement). Free-floating background components representing events with misidentified leptons are included in the fit, with several constraints. Firstly, the contributions to two regions defined by different lepton charges but otherwise identical selection cuts (including lepton flavor) must be equal under the assumption that they (in contrast to actual $W \to \ell\nu$ events) arise from charge symmetric processes. Second and lastly, the contributions in the high and low $E_{\mathrm{T}}^{\mathrm{miss}}$ sig $W \to \ell\nu$ control regions must respect the ratios constrained by MC. Good data/MC agreements in the $W \to \mu\nu$ control regions suggest very negligible misidentified muon contributions there. Thus the addition of low $E_{\mathrm{T}}^{\mathrm{miss}}$ sig $W \to \ell\nu$ control regions are applied only for electron channel. The fitted values here directly correspond to the expected number of events, and does not multiply any prediction from simulation.

4.6.2 Technical implementation

The upper limit on the branching ratio of the invisibly decaying Higgs boson is calculated using a maximum profiled likelihood fit where the likelihood is built using HistFactory. The limit is set at 95% CL using asymptotic formulae for CL_s frequentist approach. The likelihood function is constructed from the observed events in data, the yields of signal and backgrounds taken from Monte Carlo predictions, scaled by the parameters described in Table 4.9, and nuisance parameters to account for statistical uncertainty terms as well as the systematic uncertainties described in section 4.5.

As for the misidentified electron estimate, the charge asymmetry in positively charged and negatively charged W boson in production with jets is exploited. Therefore the $W(\rightarrow \ell\nu)$+jets control region is separated into different flavors and charges, applied also for the low $E_{\mathrm{T}}^{\mathrm{miss}}$ sig $W(\rightarrow e\nu)$+jets control regions. In each bin of m_{jj} distribution, the fake electron contribution has an associated floating normalization factor, after the fit those factors' best fitted values will be their normalizations. On the other hand, the $Z(\rightarrow \ell\ell)$+jets control region is split only by lepton flavors.

All MC stat errors and systematics uncertainties (from Section 4.5) are constrained by Poisson/Gaussian distribution correspondingly. Each systematic uncertainty is represented by a free fit parameter which simultaneously adjusts the normalizations of the signal and backgrounds in all regions. The parameters are dimensionless and defined so that 0 corresponds to the central-value, and ± 1 corresponds to a $\pm 1\sigma$ upward or downward shift. In some cases, there is only either fluctuation then that parameter will be symmetrized to preserve the Gaussian constraint on it. Experimental systematics are treated as correlated among signal and background processes. Scale variation and PDF systematics on W/Z samples (described in Section 4.5.2) are evaluated separately on QCD and EW production. They are treated as uncorrelated among the QCD and EW components and m_{jj} bins.

4.7 Results and Interpretations

To check the consistency of the fit model, we first look at the postfit kinematic distribution with a background only fit, using just the control region data while the signal region is masked. The distributions are shown in Section 4.7.1. Then we unmask the signal region to check for a signal. As there is no signal observed in SR, we proceed to put an upper limit on the Higgs to invisible branching ratio by performing a simultaneous fit to all the control region and signal region data, as shown in Section 4.7.2. The upper limit is then interpreted for heavier Higgs masses and to be compared to direct Dark Matter searches in **??**.

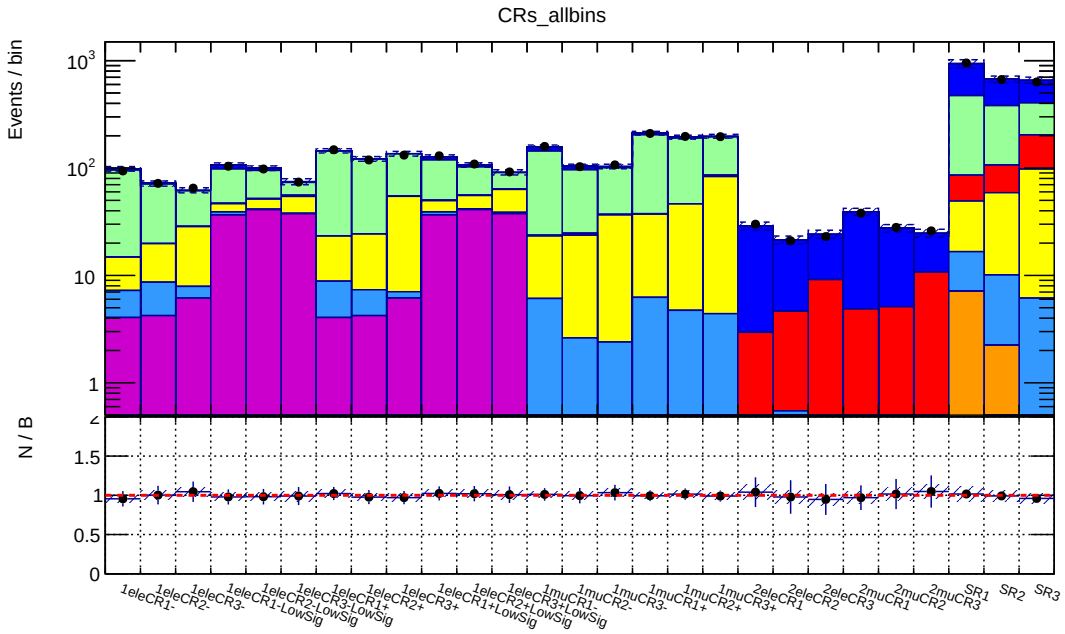

Figure 4.14: Plot showing data/MC comparison for each bin in the control regions and signal regions for 36.1 fb^{-1}. The MC predictions are the post fit results of a background only fit (see sec. 4.7.1). The error bars in the ratio plot include both the statistical uncertainty (both on the MC statistics and the poisson uncertainty from the number of observed events in data) and the systematic uncertainties (both the theoretical systematics on W/Z and the main experimental uncertainties). As a result of the fit also the electron fakes in the $W \to e\nu$ CRs are shown.

4.7.1 Postfit Kinematic Distributions

We first look at the postfit kinematic distribution with background only fit. Control region data are used while the SR is masked in the fit. A summary plot comparing post fit predictions from MC simulation with the number of observed events in each of the control regions and signal region bins is shown in Figure 4.14. The dijet invariant mass (m_{jj}) and $E_{\mathrm{T}}^{\mathrm{miss}}$ (corrected by adding vectorially the lepton p_T) post fit distributions in all the W (Z) control regions merged together are shown in Figure 4.15. The excess in W control regions is due to the fake lepton estimates in $W \to e\nu$ control regions which can't be shown since we only fit the yield and not the shape. Detailed distributions in each control region are shown in Appendix A. Same excess can be seen in the distributions in each $W \to e\nu$ control regions.

As the postfit distribution in control regions look reasonable, we then proceed to unmask

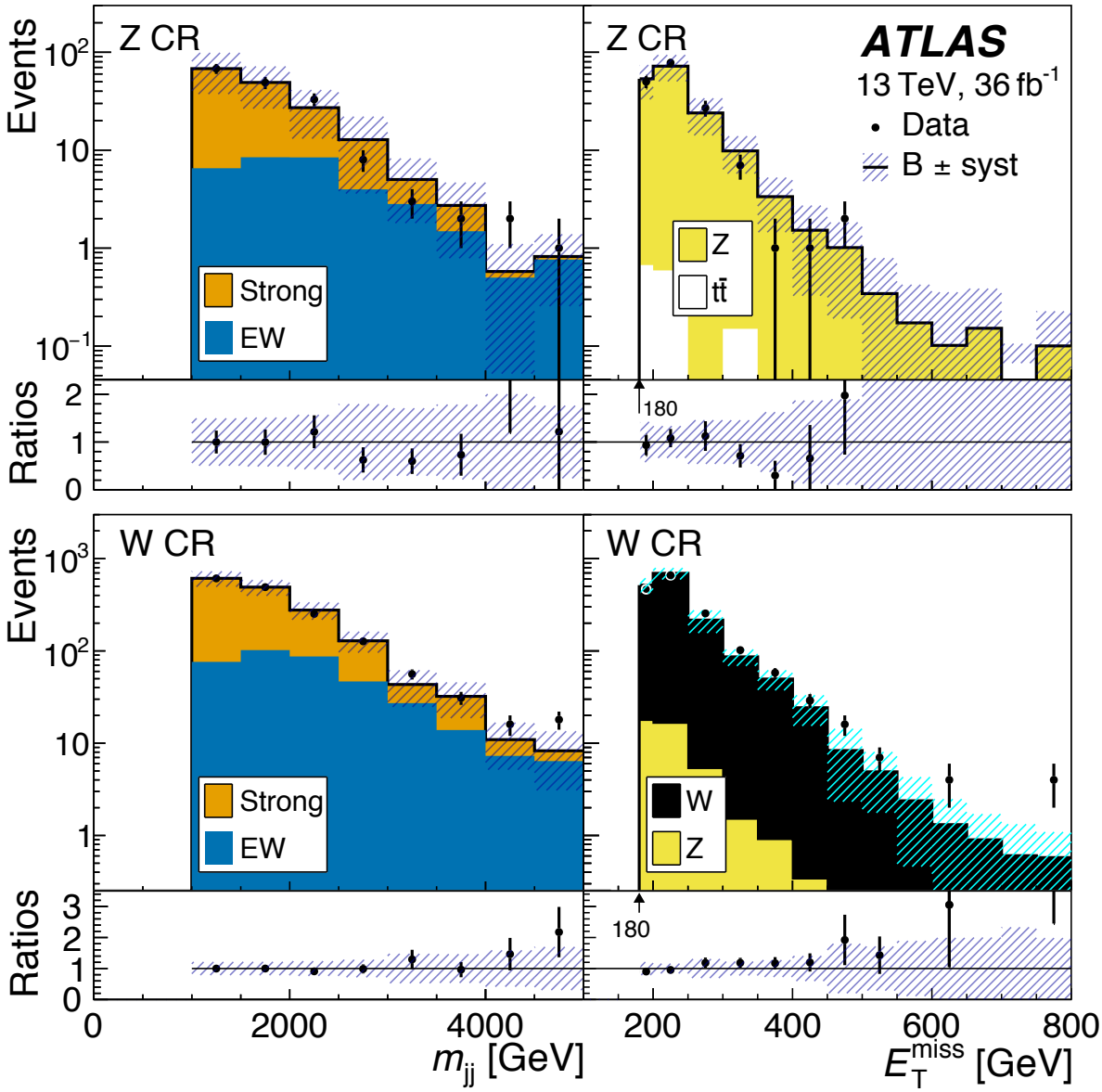

Figure 4.15: Dijet invariant mass (m_{jj}) and $E_{\mathrm{T}}^{\mathrm{miss}}$ post fit distributions for data and simulated events in the W and Z control regions with 3 mjj bins and leptons merged.

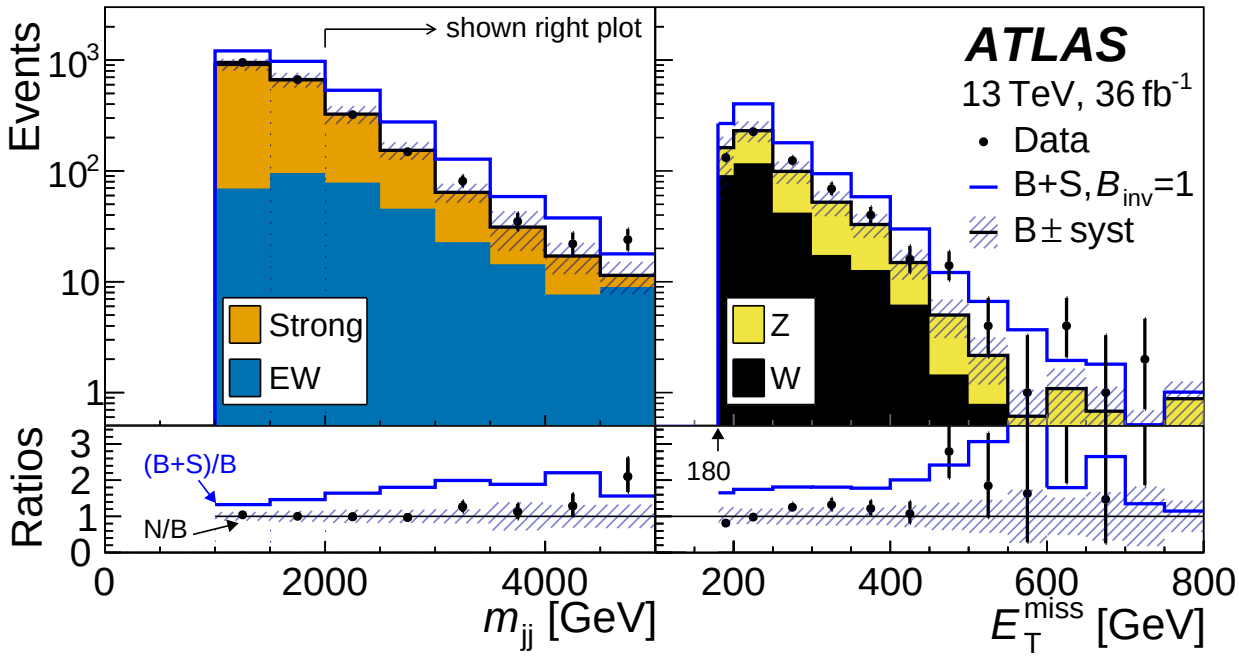

Figure 4.16: Dijet invariant mass (m_{jj}) and $E_{\mathrm{T}}^{\mathrm{miss}}$ post fit distributions for data and simulated events in the signal region with 3 mjj bins merged.

the signal region, the post fit distribution of m_{jj} and $E_{\mathrm{T}}^{\mathrm{miss}}$ in signal region with three m_{jj} bins merged is shown in Figure 4.16. The ratio between signal and background remains flat as $E_{\mathrm{T}}^{\mathrm{miss}}$ goes up while that ratio increases as m_{jj} goes up because the strong W/Z background decreases. Detailed distribution in each m_{jj} bin is shown in Appendix A. As no deviation is observed, we proceed to calculate an upper limit on the Higgs to invisible branching ratio in Section 4.7.2.

4.7.2 Upper Limit on Branching Ratio and Impact of Systematics

Table 4.10: Expected and observed limits, calculated at the 95% C.L.

Expected	Observed	+1 σ	-1 σ	+2 σ	-2 σ
0.28	0.37	0.43	0.22	0.59	0.16

The analysis put an upper limit on the Higgs to invisible branching ratio at 95% CL is 28% (37%) observed (expected). We are observing a less than one sigma deficit (see uncertainties in Table 4.10). The details of the fit results are in Table 4.11.

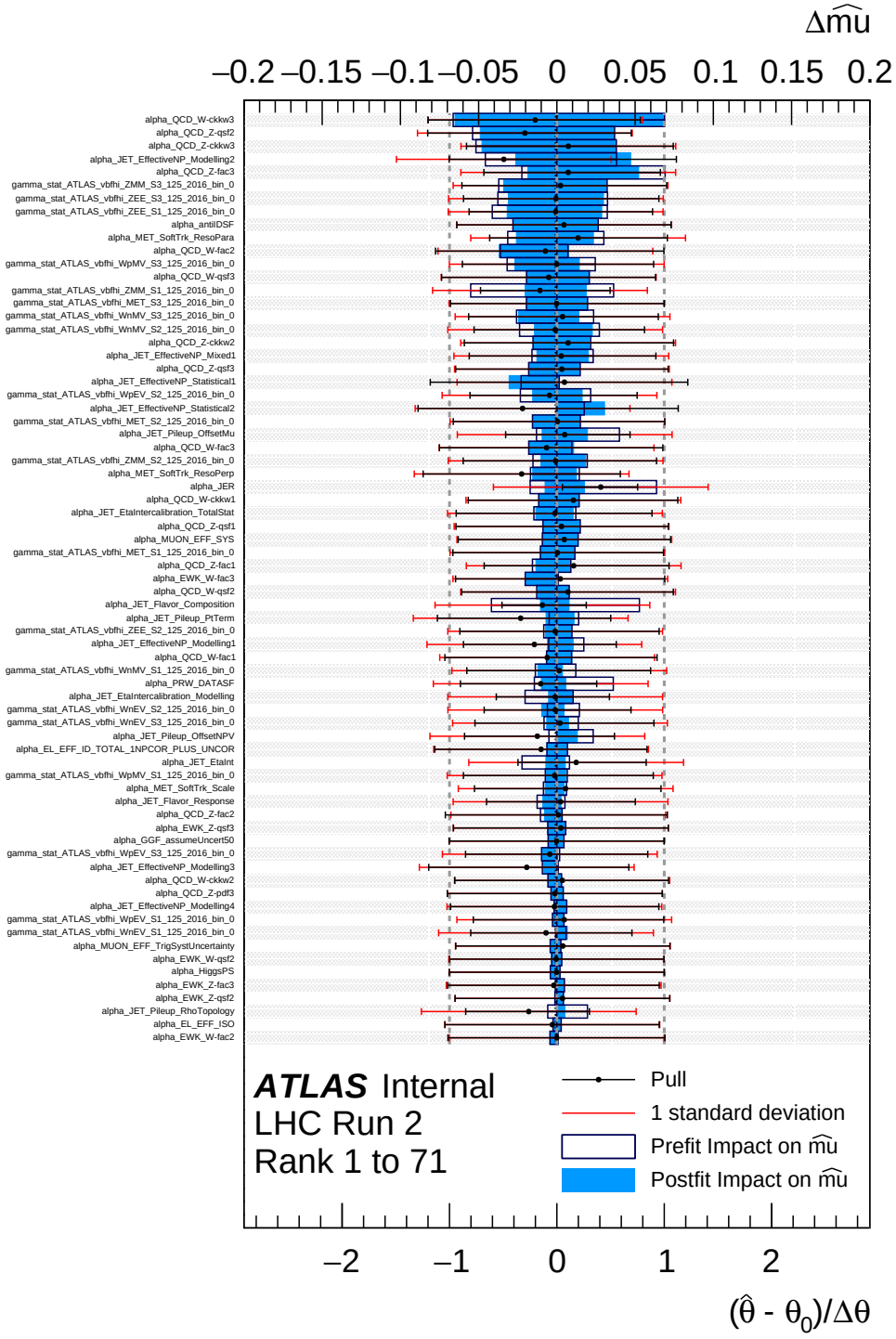

Figure 4.17: Pulls and ranking for impact of different nuisance parameters associated to the systematic uncertainties as well as the MC statistical uncertainties on the signal strength. Fit to control regions data of 36.1 fb^{-1}. This figure represent more than half of the nuisance parameters which have visible impact on the signal strengh.

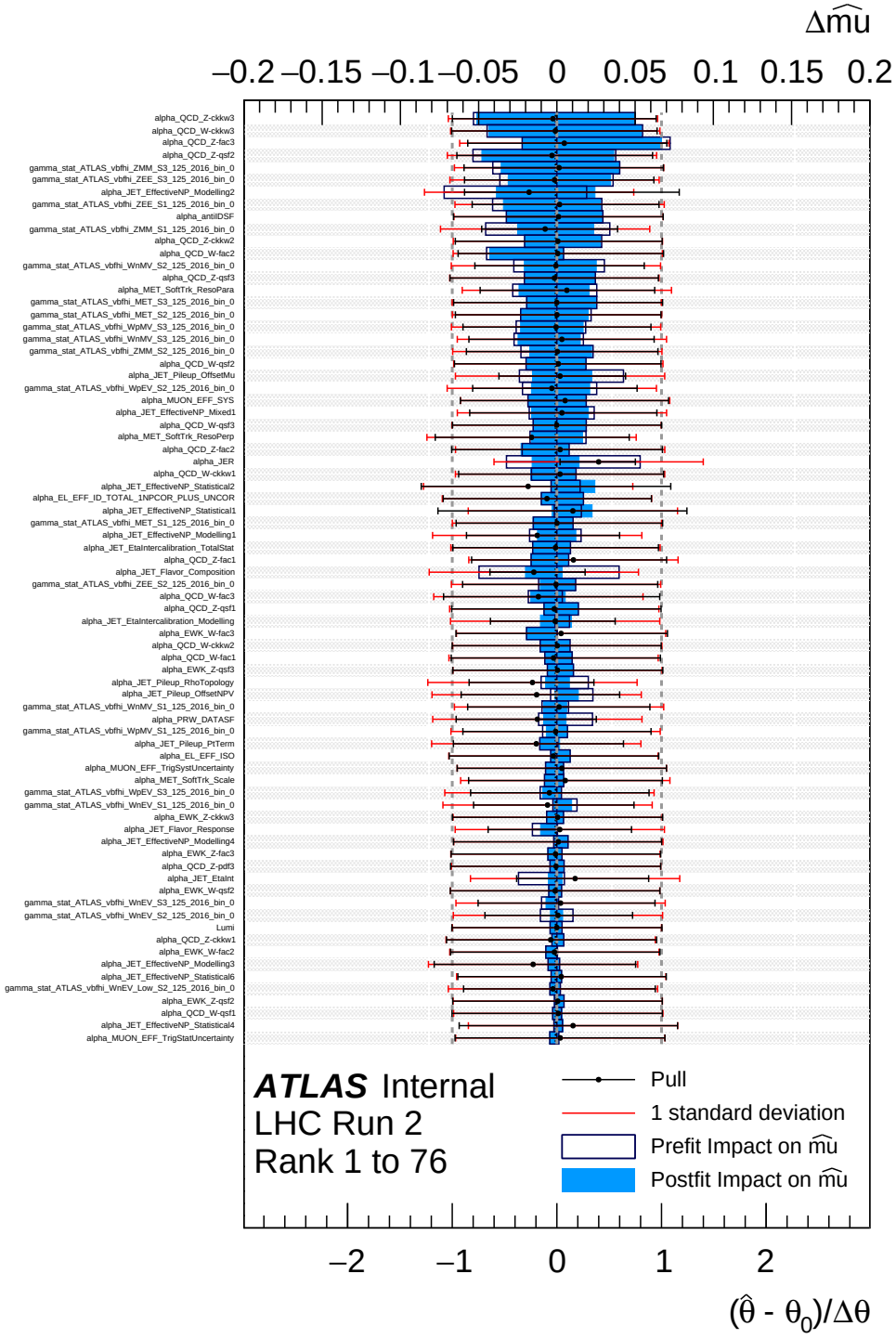

Figure 4.18: Pulls and ranking for impact of different nuisance parameters associated to the systematic uncertainties as well as the MC statistical uncertainties on the signal strength. Fit to all signal and control regions data of 36.1 fb^{-1}. This figure represent more than half of the nuisance parameters which have visible impact on the signal strength.

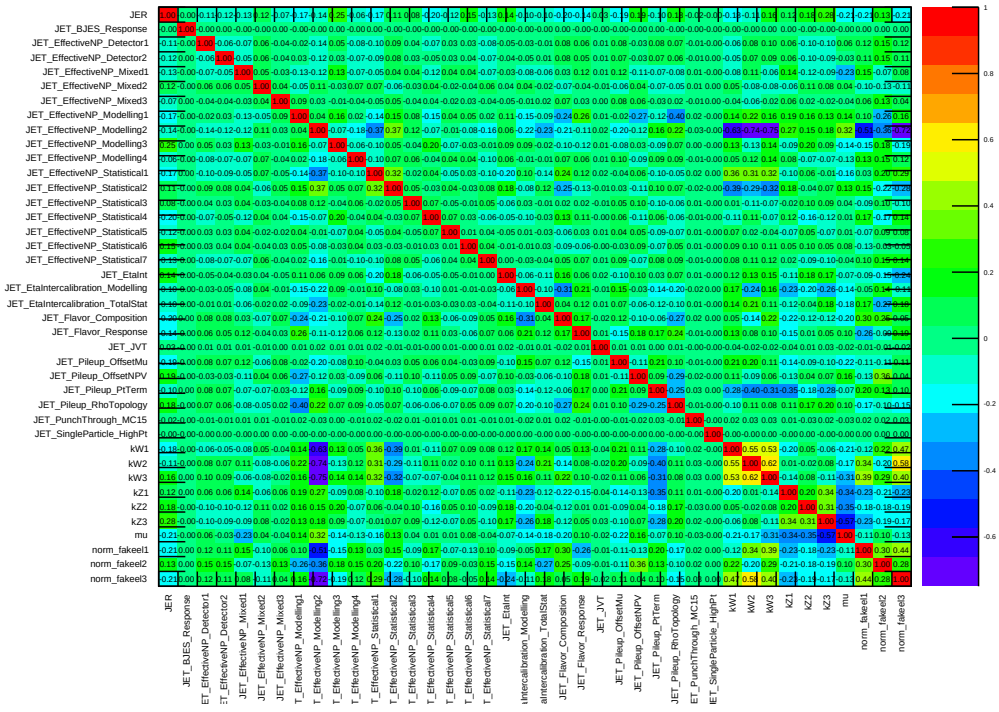

Figure 4.19: Correlation matrix among different nuisance parameter associated to the systematic uncertainties and the signal strength. The list was truncated to fit on a plot.

m_{jj}	k_W	k_Z	β
1.0 – 1.5 TeV	0.99 ± 0.27	1.07 ± 0.27	4.10 ± 1.84
1.5 – 2.0 TeV	0.99 ± 0.28	0.97 ± 0.24	4.24 ± 1.51
$>$ 2.0 TeV	1.22 ± 0.39	1.27 ± 0.31	7.74 ± 3.12
μ			
-3.83 x 10^{-2} ± 0.16			

Table 4.11: The best fit values for kW (kZ)-normalization factors for W (Z), $\beta^{ele,fake}$ as the normalization factors for fake electrons in high $E_{\mathrm{T}}^{\mathrm{miss}}$ sig-$W(\rightarrow e^{\pm}\nu)$+jets control regions of 3 binning in m_{jj}. This is done with the 36.1 fb^{-1} integrated luminosity using a simultaneous fit of the signal region and control region data. The best fit value of the signal strength, μ and the associated uncertainty is also shown.

Figures 4.17, 4.18 show the pull distributions and rankings of top nuisance parameters in the fit to data in the control regions/full signal and control regions respectively ordering by their impacts on the signal strength μ. The fit works well as the pull distributions show. Nuisance parameters include all the systematics uncertainties, statistics uncertainties and normalization factors (see details in Section 4.6). Figure 4.19 shows the correlation matrix of different parameters in the fit.

To evaluate the impacts of groups of systematics on our sensitivity, we remove groups of systematics from the limit calculation and redo the fit. The summary is shown in Table 4.12. This gives a sense of where improvements can be made that will benefit the analysis, and which groups of uncertainties make a significant impact. According to the table, one of the top constraints is MC statistics. It has been a constant challenge to generate enough MC samples due to the VBF topology. Moreover, random fluctuation due to low MC statistics can further inflate other systematics estimated using MC samples such as the jet systematics and CKKW systematics. Figure 4.20 show the distribution of the impact of jet systematics on the transfer factor (i.e. ratio between W/Z events in the CR and W/Z events in the SR), which shows signs of impact by random fluctuations. This means solving the MC statistics issues could have an even bigger impact on this analysis. It is also hard to optimize in precision when kinematic distribution and systematics are inflated by MC statistics.

Table 4.12: Variations in the expected limit as various groups of systematic uncertainties are turned off in the limit calculation. Note that experimental uncertainties and the uncertainty related to the size of the MC sample (MC stat.) are considered separate categories.

Group	Expected limit
Default	33%
No Signal's theory	30%
No MC stat.	28%
No experimental	26%
No theory	26%
No systematic	22%
No systematic & no MC stat.	18%

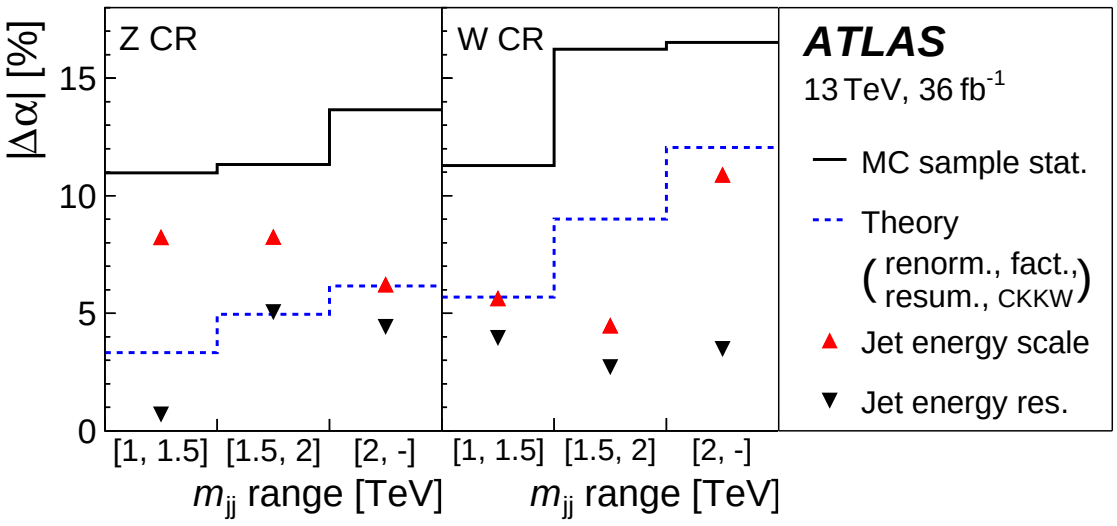

Figure 4.20: Contributions to the relative uncertainty in the transfer factors α_Z (left) and α_W (right) in the three m_{jj} bins of the SR. The theoretical uncertainties from the sources noted in the legend are combined in quadrature

Figure 4.21: WIMP-nucleon cross section vs. WIMP mass with comparison to direct Dark Matter searches.

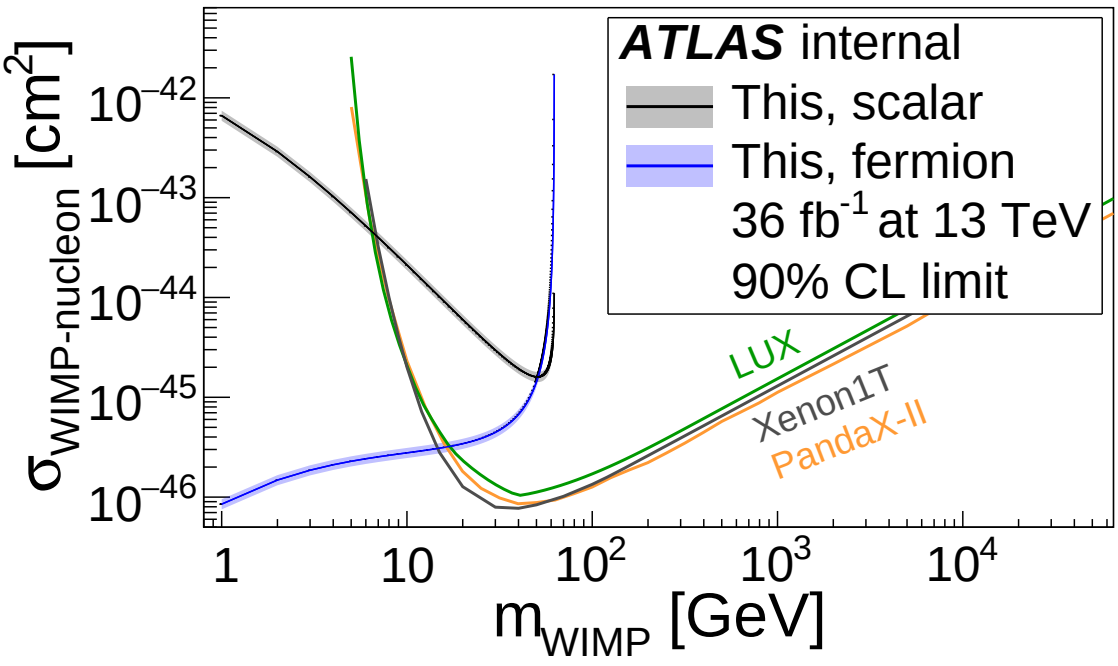

4.7.3 Interpretation

In the context of the Higgs Portal model (see Section 2.5 for details), the limits on the branching ratio can be interpreted in WIMP models and converted to limits on the WIMP-nucleon cross section. The correlation between $\mathcal{B}_{\text{inv}}$ and the WIMP-nucleon cross section is presented in the effective field theory framework, assuming that the new physics scale is $\mathcal{O}(1)$ TeV, well above the scale probed at m_H. Adding a renormalizable mechanism for generating the fermion and vector WIMP masses could modify the correlation between the WIMP-nucleon cross section and $\mathcal{B}_{\text{inv}}$ [27]. Figure 4.21 overlays our result at 90% CL with results from direct detection experiments [3, 5, 39]. Our result complements the direct searches by leading sensitivity in the low mass regime.

4.8 Conclusions

In conclusion, the analysis puts an upper limit on $\mathcal{B}_{\text{inv}}$ of 37% while expecting 28% at 95% CL. The result can be combined with searches of other productions modes to put a stronger constraint on the Higgs to invisible branching ratio. ATLAS produced an observed (expected) upper limit of 0.26 (0.17) using a combination of VBF and associated production of Higgs with a vector boson with integrated luminosities of 4.7, 20.3, and 36.1 fb^{-1} at 7, 8, and 13 TeV respectively. As a comparison, CMS recently produced an observed (expected) upper limit of 0.26 (0.20) on Higgs to invisible decays using a combination of VBF, ggF, and associated production of Higgs with a vector boson [36] with integrated luminosities of 36.1 fb^{-1} at1 3 TeV.

As the first published analysis for this search in Run 2 by ATLAS, this serves as a trial run in the much more challenging Run 2 condition. We learned a lot from this analysis and proceeded to use the knowledge to reoptimize for the full Run 2 dataset. Next chapter presents the reoptimized analysis using the same set of data.

CHAPTER 5

REOPTIMIZATION OF H $\rightarrow$ INVISIBLE

This chapter presents the reoptimized analysis of the VBF Higgs to invisible search using the same data as the published ATLAS result [38], shown in the previous chapter. As we proceeded to reoptimize the analysis for the full Run 2 dataset after the published result, we learned more ways to improve the sensitivity. The reoptimized analysis was first performed using the first 36.1 fb^{-1} of the Run 2 dataset, of which the results will be shown in this chapter. It will ultimately be used for publication with the full Run 2 dataset.

The chapter is organized as follows: Section 5.1 gives a brief summary of the changes in ATLAS software used to reconstruct kinematic variables. Section 5.2 describes the reoptimization procedure of object selection and binning scheme. Section 5.3 describes the updated background estimates used in the new results. Section 5.4 presents the reoptimized results.

5.1 Release Validation

5.1.1 Change in Release of Reconstruction Software

ATLAS software upgraded to new release since the with new recommendation and reconstruction for jet, lepton and $E_{\mathrm{T}}^{\mathrm{miss}}$. The changes in the release and validations can be summarized as following:

- The changes in the jet reconstruction and calibration resulted in fewer jets being reconstructed in release 21 above the 25 GeV p_T threshold. This results in roughly 11% more events being accepted in release 21 with the same selection criteria as release 20.7.

- In release 20.7, the inclusive NLO electroweak corrections computed from HAWK. However, the corrections are Higgs p_T dependent. This results in 10% less signal.

Region	Release 20.7	Release 21	Rel21 / 20.7
SR	2252	2499	1.11±0.02
ZCR	166	258	1.55±0.05
WCR	2209	2514	1.14±0.02

Table 5.1: The data yields in release 20.7 and 21 using the same kinematic selections as in release 20.7 in the signal region (SR), Z control region (ZCR), and the W control region (WCR). Note the data yield assumes the buggy MET trigger run numbers.

- The electron $p_T$in release 20.7 was roughly required to be larger than 18 GeV due to a skimming of the cluster properties. This resulted in 8% fewer events in release 20.7.

- The isolation selection from release 20.7 was not possible to reproduce. A looser and more efficient selection was used resulting in 9% more events in the Z control region.

- The wrong run number (e.g. 304008) was used for the transition of $E_{\mathrm{T}}^{\mathrm{miss}}$ trigger in release 20.7. This resulted in a 2.9% lower acceptance in the signal region, and this effect was not seen in the MC. Therefore the MET trigger SF's did not account for the differences. The control regions used lepton triggers, so they were unaffected.

5.1.2 Validation Using Analysis Selection in Release 20.7

The number of events in each region are compared in the two releases in Table 5.1. The ratio of the data yields in the signal region is consistent with a 11% increase due to the changes in the jet reconstruction. This is caused by changes in the jet reconstruction that results in fewer jets in release 21, so more events are accepted with the third jet veto requirement. The jet reconstruction also changes the $E_{\mathrm{T}}^{\mathrm{miss}}$ as jets are moved to the soft term. These increases in yield of around 11% are shown in release comparison distributions of data in Figure 5.1. Other distributions agree well in shape between the two releases. The W control region increases are consistent with the changes in the signal region.

The Z control region has a larger increase of 55%. This increase is explained by several changes and a feature in the release 20.7 derivations.

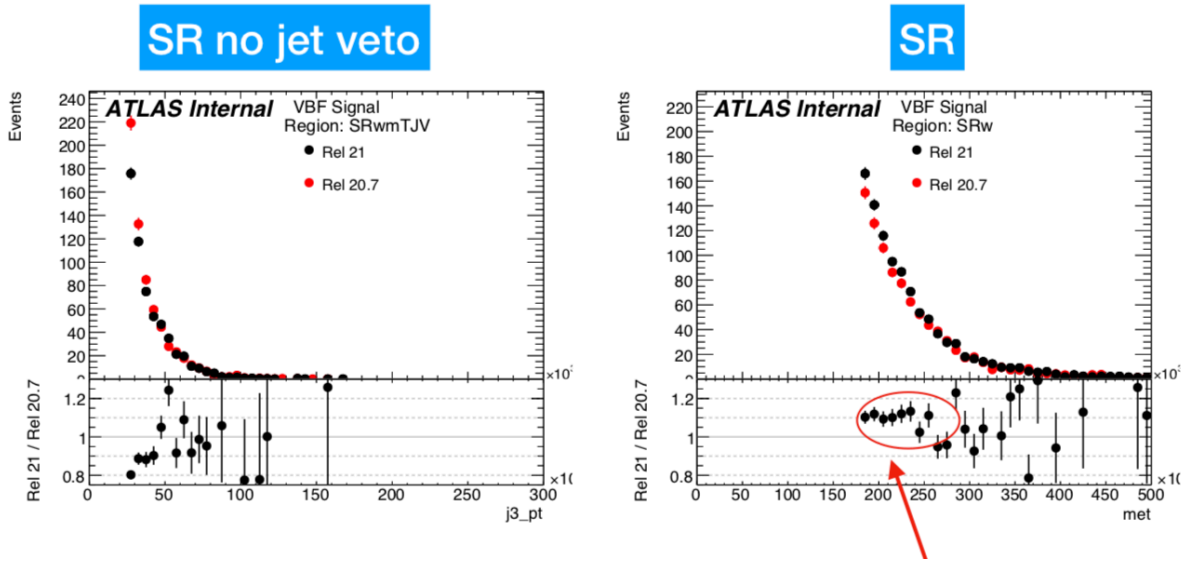

Figure 5.1: Comparison in the signal region of the third leading jet p_T distribution in release 21 and 20.7 (left) with the third jet veto removed. The $E_{\mathrm{T}}^{\mathrm{miss}}$ distribution is compared between release 21 and 20.7.

- The electron p_T in release 20.7 was increase to 18 GeV due to cluster skimming in the release 20.7.
- Changes in release 20.7 derivations result in 8% reduction in yields in the Z control region in release 21.
- The isolation definition "Gradient" used in release 20.7 is less efficient than in release 21 using the "FCLoose" operating point used for validation. The increase from combined performance changes indicates to expect around a 9% increase in release 21 yields.
- The η acceptance for muons was increased from 2.5 to 2.7, which is a 1% increase in release 21.

Selection	Fractional Overlap
SR	0.73
3rd jet $p_T < 35$GeV and $E_{\mathrm{T}}^{\mathrm{miss}} > 165$GeV	0.84
No lepton veto	0.88
$\Delta\eta_{\mathrm{jj}} > 3.8$	0.88
jet $p_T > 70, 40$GeV	0.91
$m_{\mathrm{jj}} > 200$GeV	0.91
$E_{\mathrm{T}}^{\mathrm{miss}} > 100$GeV	0.93
$N_{\mathrm{jet}} < 6$	0.940
$\Delta\Phi_{\mathrm{jj}} < 2$	0.943

Table 5.2: Starting in the signal region using the release 20.7 selections, the release 21 selection criteria are removed. Each line successive line has the above criteria also removed. The fraction of events from release 20.7 that are found in release 21 with the changed selection is shown.

- The electron crack veto was removed in release 21, and it increases the release 21 yield by 4%.

Collecting these changes in release 21 results in a ratio data yields in release 21 to 20.7 of 1.23 ± 0.05 in the Z control region. The events from the release 20.7 analysis that are also selected in release 21 is 73%. It is lower at 53% in the Z control region due to the changes described above. The primary reason for this relatively small overlap in events is the jet reconstruction changes. To demonstrate this, the release 21 selection criteria were loosened, and the overlapping fraction of events overlapping was recomputed. This is summarized in Table 5.2. The overlapping events were increased to 94%. The remaining events could be recovered if selection criteria were further loosened beyond our skimmed derivations. The 94% overlap was sufficient to state that we understand the changes in the release. The largest increases in overlap come from lepton changes (e.g. isolation and electron p_T) and jet changes.

Comparisons of the data to simulation agreement using the release 20.7 selection criteria are shown in the signal region, Z control region, and W control region in Figures 5.2, 5.3, and 5.4. The $E_{\mathrm{T}}^{\mathrm{miss}}$ and m_{jj} are shown. Similar agreement is shown in the two releases.

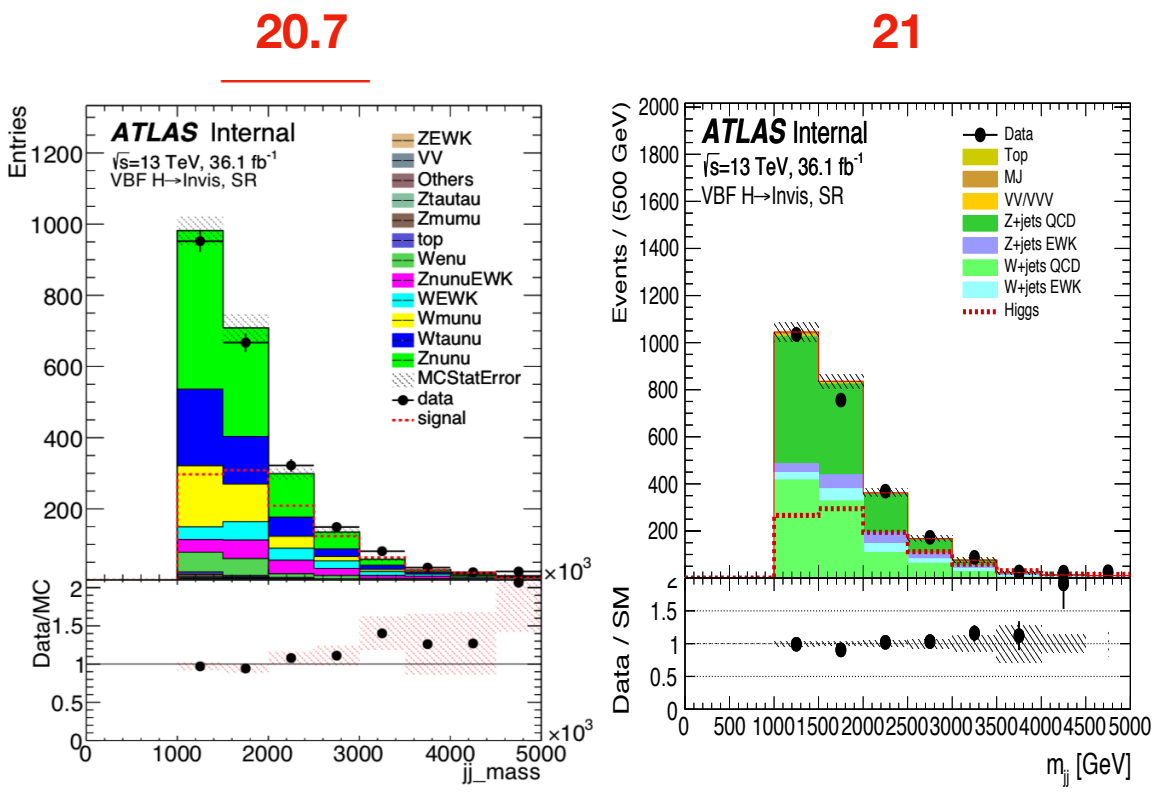

Figure 5.2: The signal region in release 20.7 (left) and release 21 (right). The invariant mass of the leading two jets is shown.

5.1.3 Resulting Changes in the Limits

Including all of the changes from the above section, the release 21 comparison was finalized with a comparison of the 95% CL limits as shown in Table 5.3. The statistical only limit is 10% worse due primarily to the 10% decrease in the signal yields from the NLO electroweak corrections. The expected limits with systematics are the same within rounding. The large change in the observed is believe to statistical and primarily from the Z control region, which went from a data/MC of 0.9XX in release 20.7 to 1.05±XX in release 21. This pulls the background up in the signal region. The difference in the observed limits using the 53% correlation of events from the Z control region, which is the dominant uncertainty in the analysis, is roughly $(0.37 - 0.26)/(0.15 * 0.53) = 1.5\sigma$.

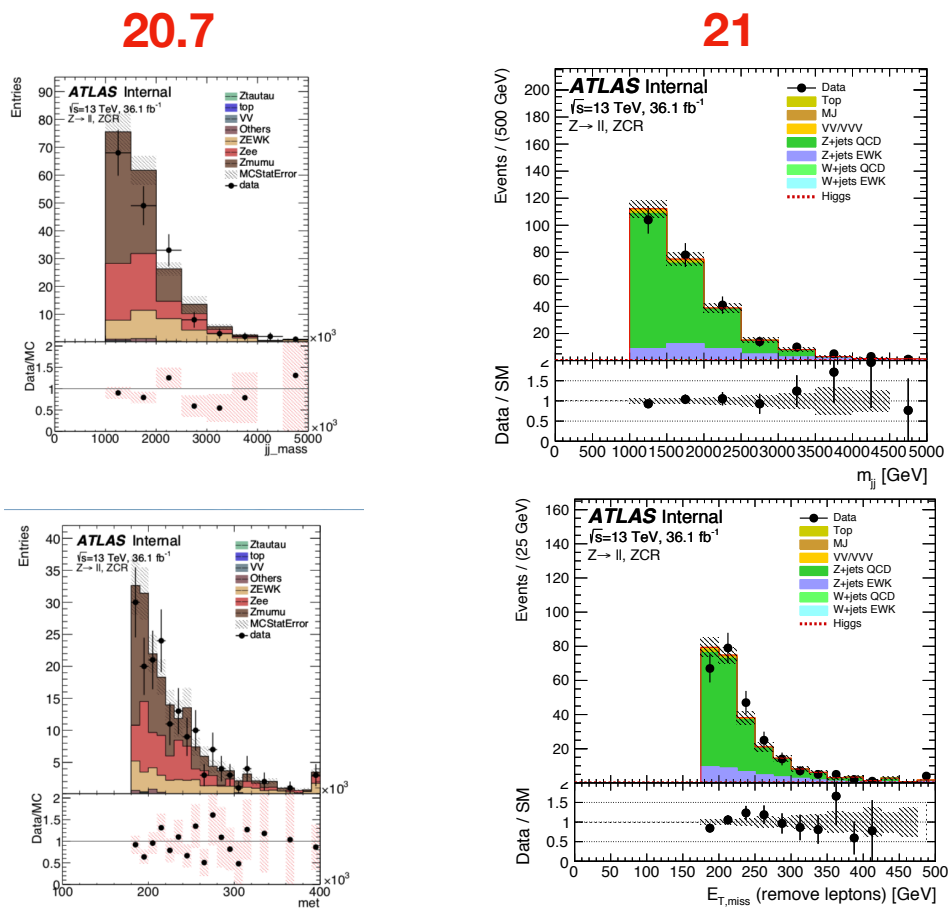

Figure 5.3: The Z control region in release 20.7 (left) and release 21 (right). The invariant mass of the leading two jets (upper) and $E_{\mathrm{T}}^{\mathrm{miss}}$ (lower) are shown.

5.2 Reoptimization

5.2.1 Object Selection

In order to pick out maximum signal and minimum background events we studied the distribution of kinematic variables of signal and background MC samples and looked at the S/B in the Signal Region. Since the Control Region statistics (ZCR) and systematics have a big impact on the sensitivity of this analysis, in order to take CR into consideration, we plotted an approximation σ_{μ}^{95} of the 95% CL limit on Higgs to invisible branching ratio where $\sigma_{\mu}^{95} = 2\sqrt{N_{\mathrm{background}} + (0.02N_W)^2 + (\sigma_Z N_Z)^2}/N_{\mathrm{signal}}$ serves as the approximated impact from ZCR statistics and a 2% systematic uncertainty from WCR. For maximum sensitivity

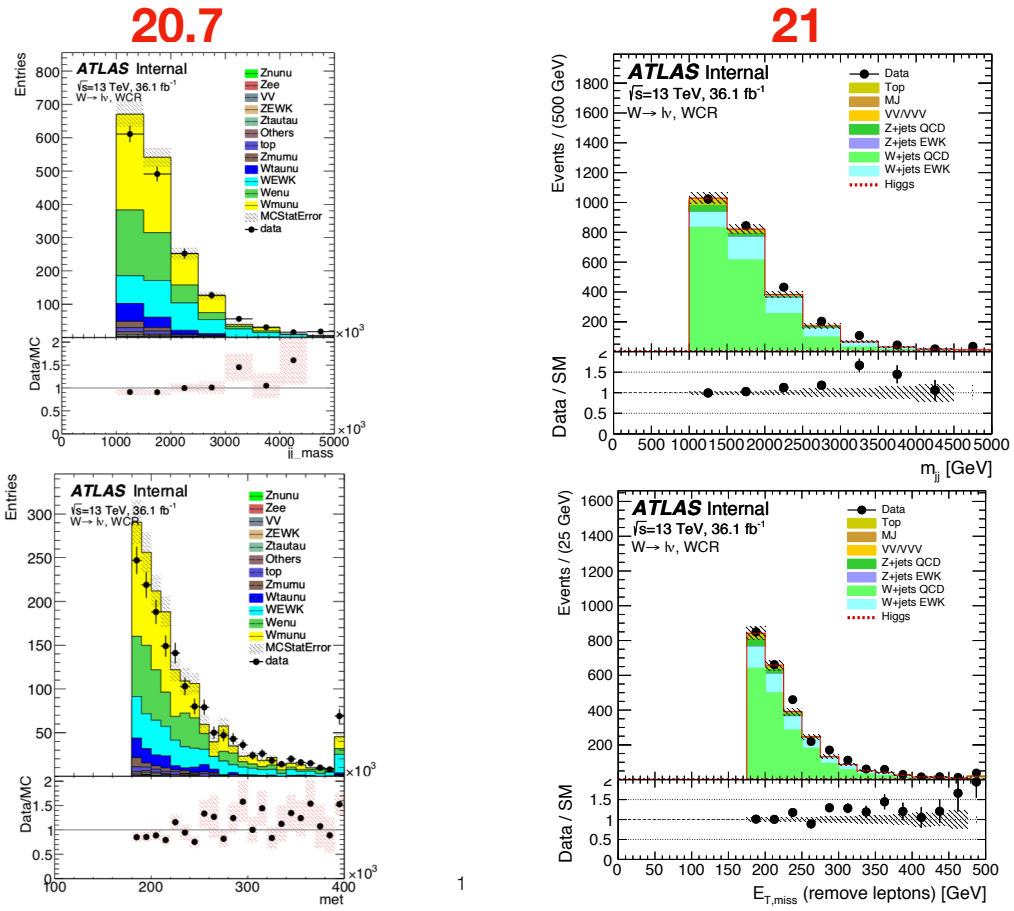

Figure 5.4: The W control region in release 20.7 (left) and release 21 (right). The invariant mass of the leading two jets (upper) and $E_{\mathrm{T}}^{\mathrm{miss}}$ (lower) are shown.

we would want a large S/B and small σ_{μ}^{95}. If S/B and σ_{μ}^{95} are pretty flat, we would want to go for looser selection to gain more signal as well as more statistics for both CR and MC except if the looser selection might bring us much larger QCD background as that is estimated separately and not taken into account in the S/B plotted here.

Looking at the S/B and σ_{μ}^{95} for $\Delta\eta_{\mathrm{jj}}$ Figure 5.5, we see that although S/B drops down as we go to lower $\Delta\eta_{\mathrm{jj}}$, σ_{μ}^{95} also goes down. Higher statistics in CR result in a more precise background estimate. In addition, things become quite flat as $\Delta\eta_{\mathrm{jj}}$ drops off. Since we always want more signal and statistics, we chose to lower the cut from $\Delta\eta_{\mathrm{jj}} > 4.8$ to $\Delta\eta_{\mathrm{jj}} > 3.8$. We did not go lower than that due to concerns about increasing QCD background and there is no improvement in sensitivity.

Release	Expected stat only	Expected w/systematics	Observed
20.7	0.20	0.28	0.37±0.15
21	0.22	0.28	0.26±0.12

Table 5.3: The 95% CL expected and observed limits are shown in release 20.7 and release 21 with the selection criteria from release 20.7.

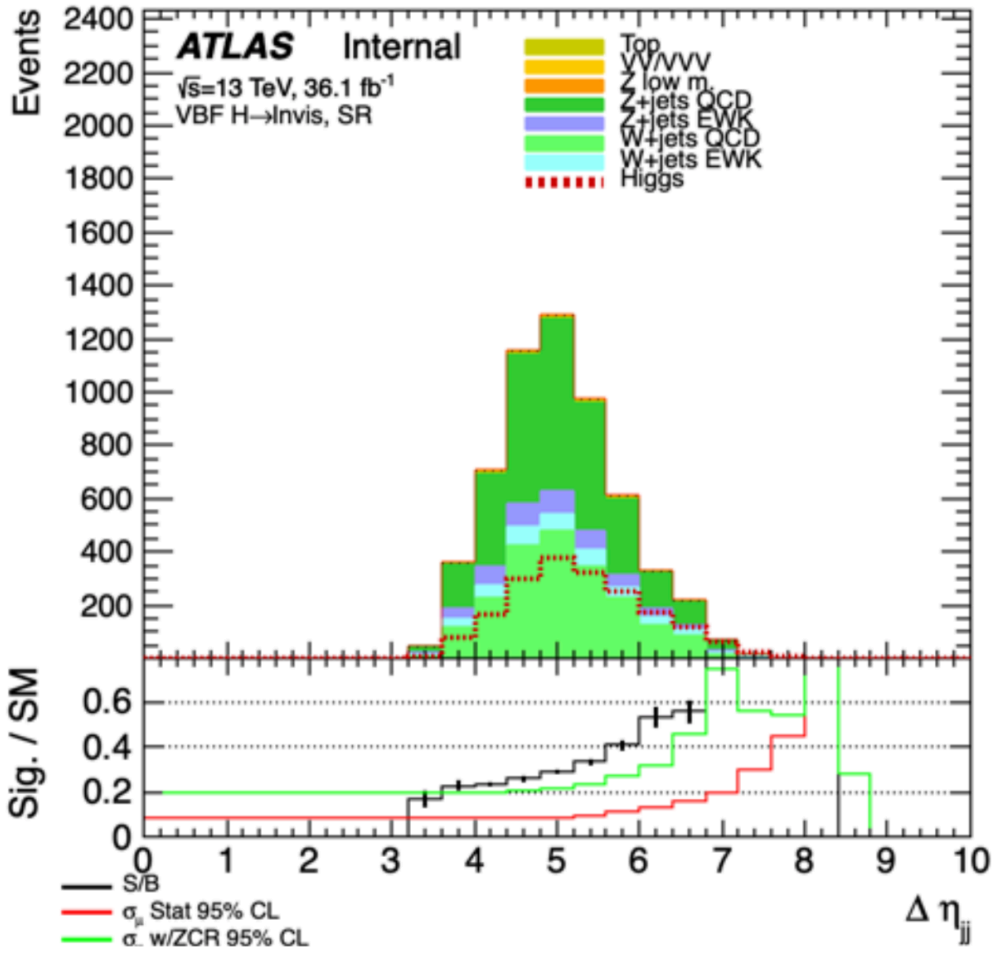

Figure 5.5: Distribution of $\Delta\eta_{\mathrm{jj}}$ with the original 36.1 fb^{-1} selection with a looser cut on $\Delta\eta_{\mathrm{jj}}$. Black curve on the bottom plot is the S/B and the green is σ_{μ}^{95}

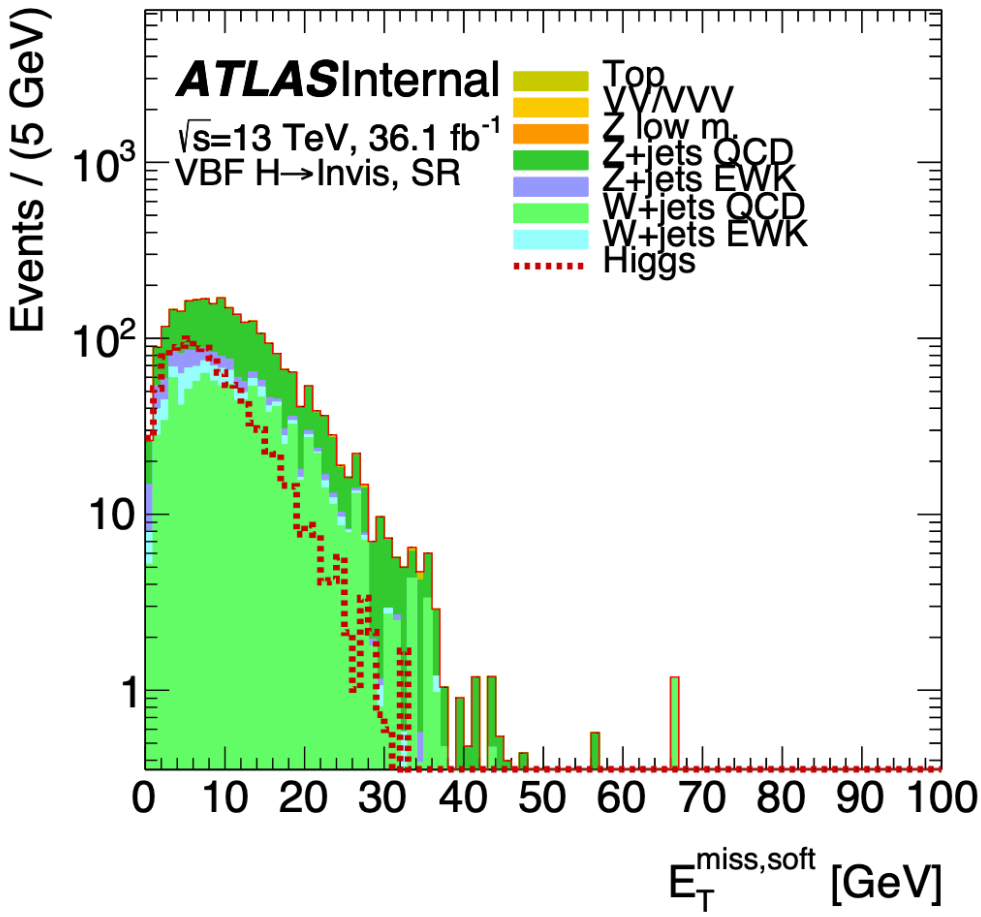

Figure 5.6: Distribution of $E_{\mathrm{T}}^{\mathrm{miss}}$ soft term with the original 36.1 fb^{-1} selection.

We investigated the possibility to use the $E_{\mathrm{T}}^{\mathrm{miss}}$ soft term to further reject background in SR. $E_{\mathrm{T}}^{\mathrm{miss}}$ soft term is calculated by adding all the PV tracks not associated to hard objects together. It is sensitive to extra leptons and extra charged particles through the tracks. The signal does not have any color flow; therefore very small radiation is expected between the two tagged jets. On the contrary, QCD processes have large radiation. The $E_{\mathrm{T}}^{\mathrm{miss}}$ soft term requires that central charged activity is small. The distribution Figure 5.6 shows that there is indeed a difference between our signal and background and cutting at 20 GeV rejects about 10% background and only 1% signal.

Increasing the lepton acceptance and reconstruction efficiency used for lepton veto can reduce W/Z background in the SR. This is the only way to reduce the EWK component of W/Z background. The Working Point for the original 36.1 fb^{-1} selection is Tight for electrons and Medium for muons. We investigated the possibility to loosen the Working Point to Loose for both electrons and muons. One concern for looser lepton selection is possible fakes from jets reducing our signal efficiency; therefore we plotted the lepton p_{T} for both truth and reconstructed leptons with loose Working Point from the W samples in the SR Figure 5.7. Since the truth and reconstructed leptons agree well for both electrons and muons, we can safely use the loose Working Point. Also as there are more events as we go to lower lepton p_{T}, we decided to lower the p_{T} of the lepton veto from 7 GeV to 4.5 GeV for electrons and from 7 GeV to 4 GeV for muons. While the relative uncertainty is larger for the measured inefficiency systematic, the background yield is smaller. The total non-relative uncertainty is therefore reduced.

Jet vertex fraction (JVT) is a multivariate technique that compares the contributions of track momenta from the primary vertex to those from pileup vertices. In the original 36.1 fb^{-1} analysis we faced a challenging QCD issue with JVT where JVT removed a central QCD jet but its counterpart in the forward region remained. While a forward JVT tag would be useful, fJVT at that time was only recommended to be applied to jets with p_{T} between 20 GeV and 60 GeV, which was shown not to be useful to us because it would mostly apply to our

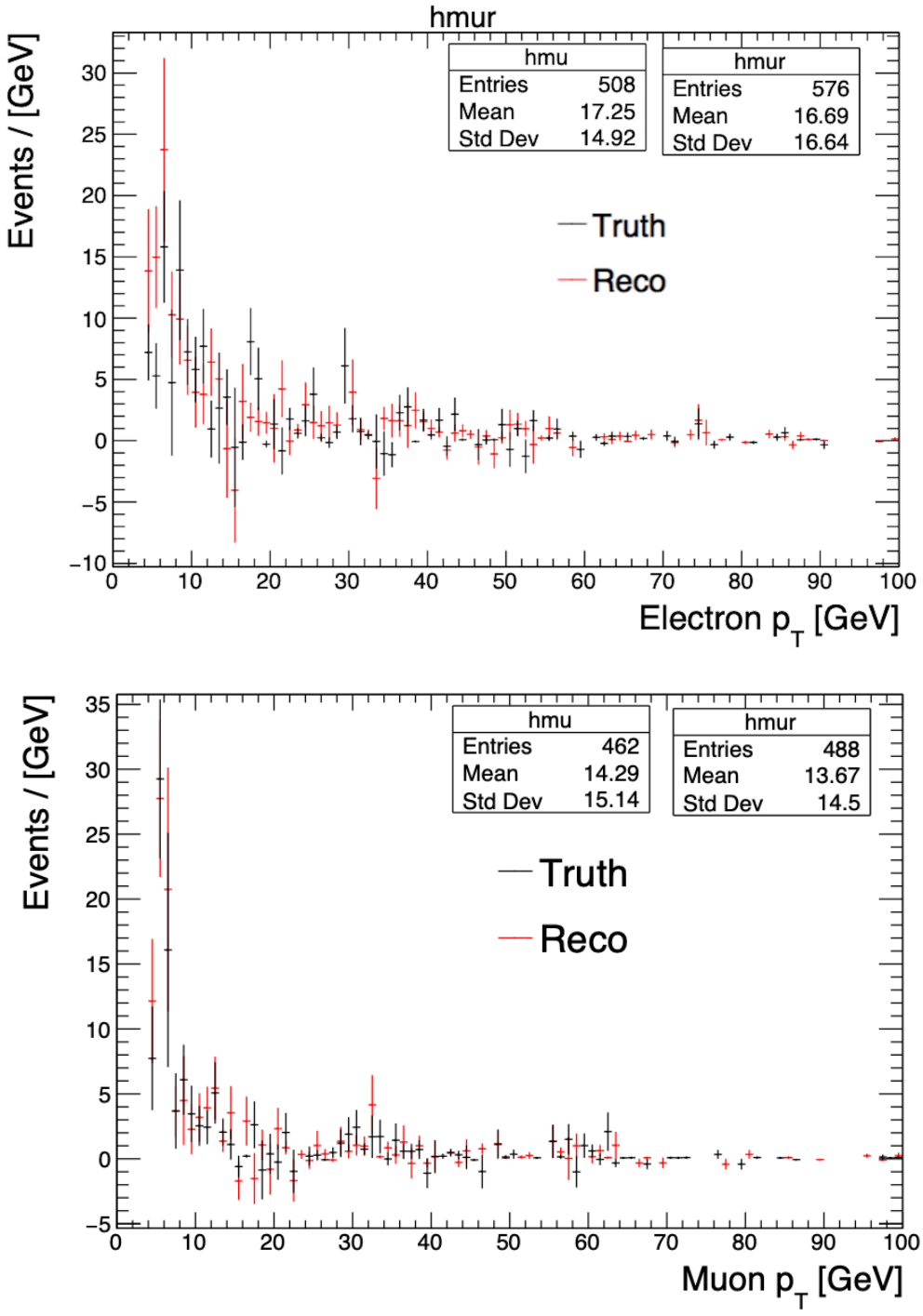

Figure 5.7: Distribution of electron and muon p_{T} with the release original 36.1 fb^{-1} selection.

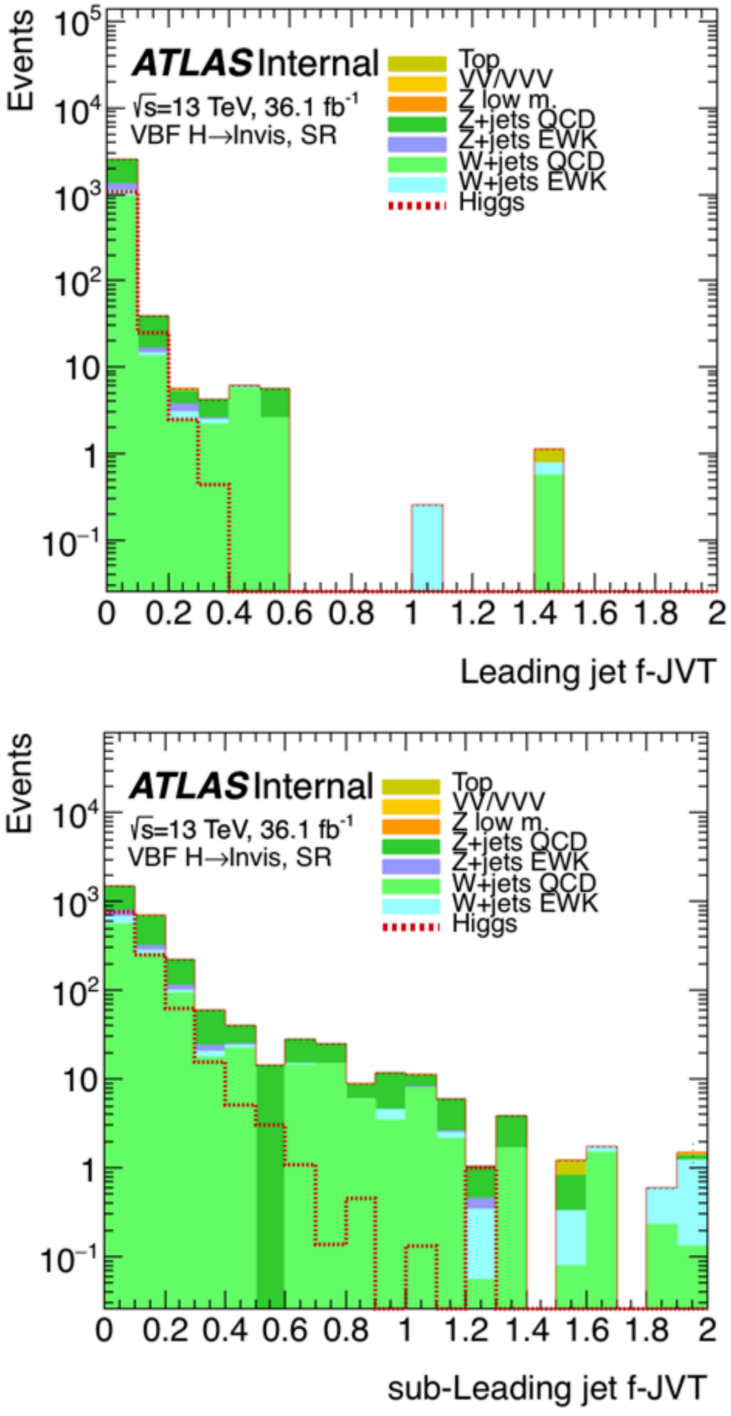

Figure 5.8: Distribution of fJVT of leading and subleading jets with the original 36.1 fb^{-1} selection.

Table 5.4: Yields of signal and major backgrounds and S/B with different $E_{\mathrm{T}}^{\mathrm{miss}}$ Working Point in SR using original 36.1 fb^{-1} selection

	Signal	Top	W strong	W EWK	Z strong	Z EWK	Total Background	S/B
Loose	1571	22.3	1422	194	1744	254	3642	0.431
Tight	1554	23.4	1333	192	1700	253	3505	0.443
Tighter	1554	23.4	1333	192	1700	253	3505	0.443
Tenacious	1547	22.9	1286	191	1694	253	3451	0.448

third jet veto and not solve the issue with pileup jets faking tagged jets. The fJVT algorithm assigns a score of 0 for hard scatter jets and 2 for pileup. It considers whether adding the jet to another vertex would reduce the $E_{\mathrm{T}}^{\mathrm{miss}}$ of that vertex. This uses the assumption that momentum is conserved in the transverse plan of the beamline and that soft interactions that lead to pileup vertices do not produce high p_{T} neutrinos. Recent development of fJVT made it possible for us to apply it to higher p_{T} jets and therefore became useful in selecting the two tagged jets. We plotted signal and background distribution with the fJVT for both tagged jets Figure 5.8 and saw a clear signal and background distinction. A cut of fJVT< 0.5 proved to reduce W/Z strong backgrounds with negligible signal loss.

We explored all the new $E_{\mathrm{T}}^{\mathrm{miss}}$ Working Points to find the optimal setting for our analysis by looking at the background compositions and S/B in SR. It seemed that while all the Working Points performed similarly in terms of S/B the Tenacious Working Point performed slightly better. Since QCD background was estimated later using data driven method, to check on the contamination of QCD background with different $E_{\mathrm{T}}^{\mathrm{miss}}$ Working Point, we checked on data in a QCD enriched validation region where we required the events to have at least 5 jets with the two leading jets satisfying $m_{\mathrm{jj}} > 200\mathrm{GeV}, \Delta\eta_{\mathrm{jj}} > 2.5$ and a 180 GeV cut on the Tight $E_{\mathrm{T}}^{\mathrm{miss}}$ Working Point Figure 5.9. With the same selection $E_{\mathrm{T}}^{\mathrm{miss}}$ tenacious had much fewer events.

Because there is no color flow in our signal, we expect very little radiation between the two tagged jets. The third jet veto was hence a very efficient cut to reject QCD and W/Z strong background which usually have lots of central radiation. However, additional jets outside or nearby the two tagged jets can be perfectly good signal. We plotted the N_{jet}

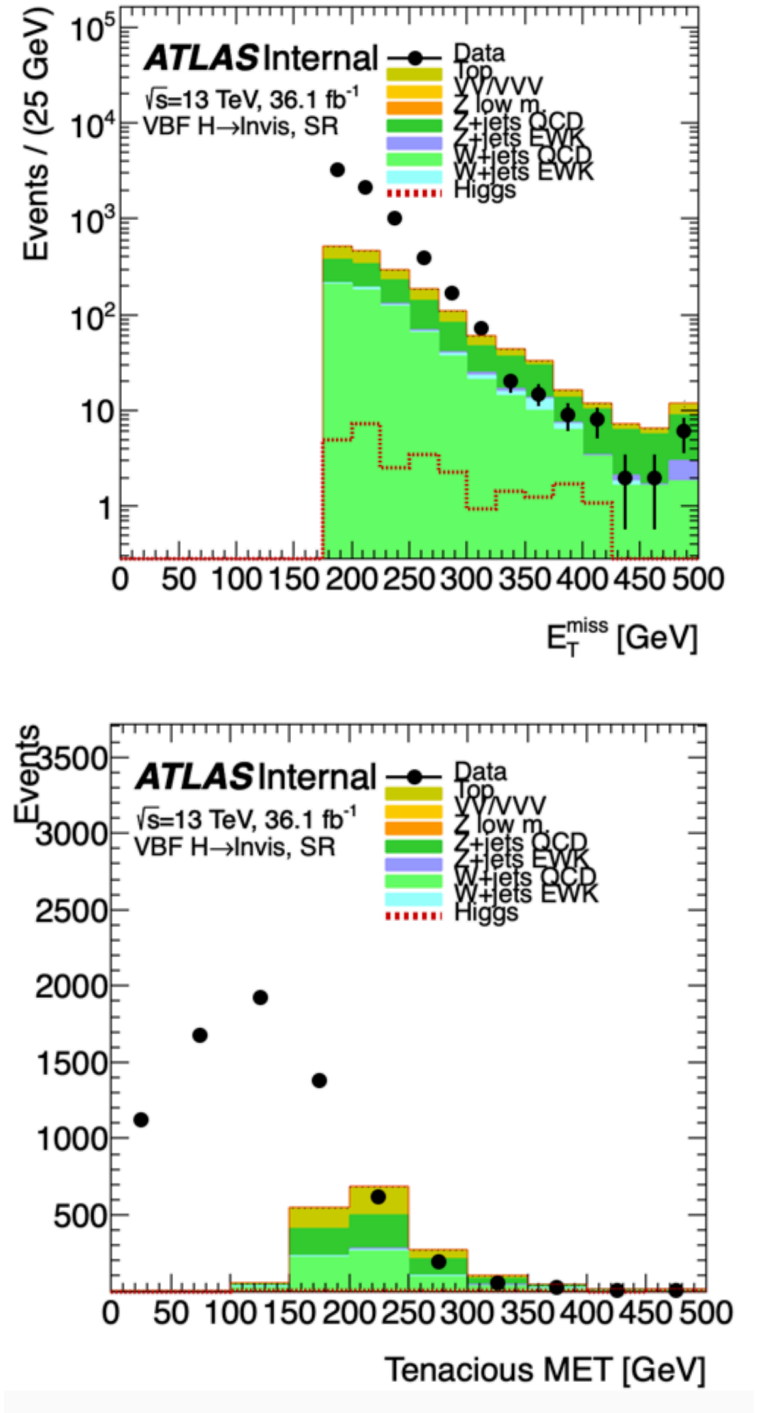

Figure 5.9: Data and MC distribution of $E_{\mathrm{T}}^{\mathrm{miss}}$ Tight and Tenacious Working Points in the QCD enriched validation region.

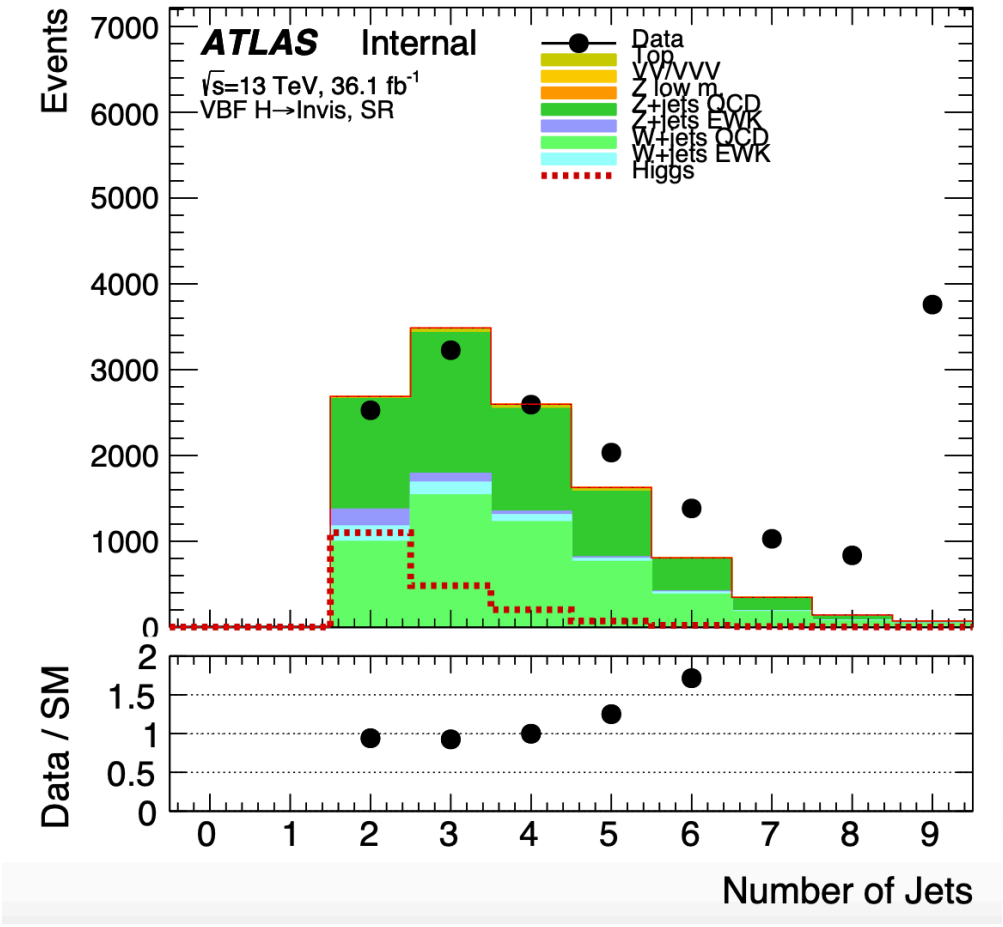

Figure 5.10: Distribution of number of jets with dijet mass > 200 GeV

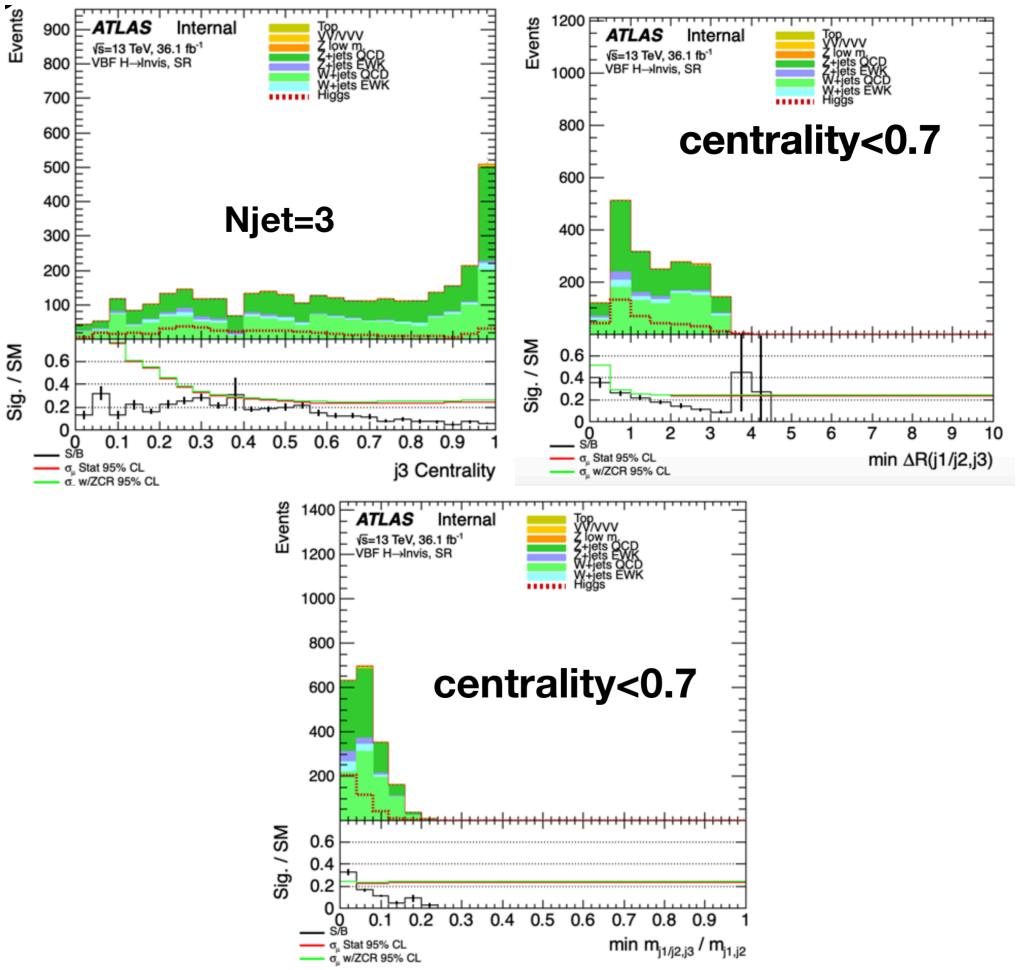

Figure 5.11: Distribution of Centrality and the ratio of the minimum dijet mass between the third jet and the two tagged jets, minimum of ΔR between the third jet and tagged jets, and the dijet mass of the two tagged jets in the $N_{\text{jet}} = 3$ bin with the rest of the original 36.1 fb^{-1} SR selection.

distribution with an inclusive selection to check on signal strength and QCD contamination in Figure 5.10. There seems to be sizeable amount of signal in the $N_{\text{jet}} = 3$ and 4 bins and a larger QCD background when $N_{\text{jet}} > 4$. Therefore, we explored the possibility of having an additional bin with more than two jets to gain sensitivity through the additional statistics. In order to reject W/Z strong background in this additional Njet bin, we studied the variable called Centrality C_3 [19]:

$$C_3 = \exp(-\frac{4}{(\eta_1 - \eta_2)^2}(\eta_3 - \frac{\eta_1 + \eta_2}{2})^2). \tag{5.1}$$

As shown in Figure 5.11, there is a big difference in S/B when we plotted C_3 in additional bin where we keep all the other cuts the same as original SR except the additional third jet. $C_3 < 0.7$ seemed to be a good choice based on the S/B and σ_μ^{95} distribution. On top of the $C_3 < 0.7$ requirement we explored other kinematic variables such as ΔR between the third jet and a tagged jet and the dijet mass of the third jet and a tagged jet. Dijet mass seemed to have a steeper S/B drop off, In the end, we concluded with an additional Njet region with up to two additional jets ($N_{\text{jet}} < 5$) with $\max(C_3, C_4) < 0.6$ and $\max(m_{\text{j3j}}/m_{\text{jj}}, m_{\text{j4j}}/m_{\text{jj}}) < 0.05$. Low masses indicate that the jet is more likely a Final State Radiation (FSR). We cut on the ratio of dijet mass to be less dependent of the dijet mass of the two tagged jets. One can potentially gain more sensitivity using multivariate techniques on more variables.

We proceeded to further optimize the CR selection. Since Z CR was statistics limited, we explored the possibility to loosen the lepton definition in Z CR. While the lepton Working Points were limited by the single lepton trigger, we could switch to Loose Working Point for the subleading lepton in Z CR by including dilepton triggers. Switching to Loose WP brought the expected limit with statistics uncertainties only from 0.1785 to 0.1734 (3 % improvement).

Table 5.5 summarizes all the changes on kinematic cuts for SR after the reoptimization studies. We will explore different binning schemes in Section 5.2.2. With all the stated

Table 5.5: Table of the original 36.1 fb^{-1} inclusive selection and the updated inclusive selection for SR. Changes are highlighted in red.

Requirement	Original	Reoptimized
$e(\mu)$ Veto	$< 7(7)$ GeV Tight (Medium)	$< 4.5(4)$ GeV Loose (Very Loose)
Jet p_{T}	$> 80(50)$ GeV	$> 80(50)$GeV
fJVT	–	< 0.5 if $E_{\mathrm{T}}^{\mathrm{miss}} > 180$ GeV else 0.2
$E_{\mathrm{T}}^{\mathrm{miss}}$	> 180 GeV Loose	> 150 GeV Tenacious
MHT	> 150 GeV	> 120 GeV
$E_{\mathrm{T}}^{\mathrm{miss}}$ soft term	–	< 20 GeV
$\Delta\Phi_{\mathrm{j}E_{\mathrm{T}}^{\mathrm{miss}}}$	> 1.0	> 1.0
$\Delta\eta_{\mathrm{jj}}$	> 4.8	> 3.8
Njets	$= 2$ (3rd < 25 GeV)	< 5 (5th < 25 GeV)
Max centrality	–	< 0.6
$\max(m_{\mathrm{j3,4j}}/m_{\mathrm{jj}})$	–	< 0.05
$\Delta\Phi_{\mathrm{jj}}$	< 1.8	< 1.8
m_{jj}	> 1 TeV	> 1 TeV

changes in SR and 3 m_{jj} bins same as the original 36.1 fb^{-1} analysis, we got an expected upper limit on the Higgs to invisible branching ratio at 0.2493 using Asimov only fit. For detailed description of the fitting strategy see Section 4.6. Using the same updated release of reconstruction software, with the original 36.1 fb^{-1} selection we got 0.2639.

5.2.2 Binnings

With the reoptimized selection, the signal acceptance increased doubled, but background also increased. We would like to explore different binning schemes using the reoptimized selection on top of the 3 m_{jj} bins used in the original analysis. While having more m_{jj} bins and using a shape fit could have potential benefit, it was hard to show when lots of systematics were calculated with limited MC statistics. It is in our interest to bin in variables with non-flat S/B distribution so that we could benefit from a higher S/B in one bin and gain signal acceptance from another bin. In order to find the best binning, we did Asimov

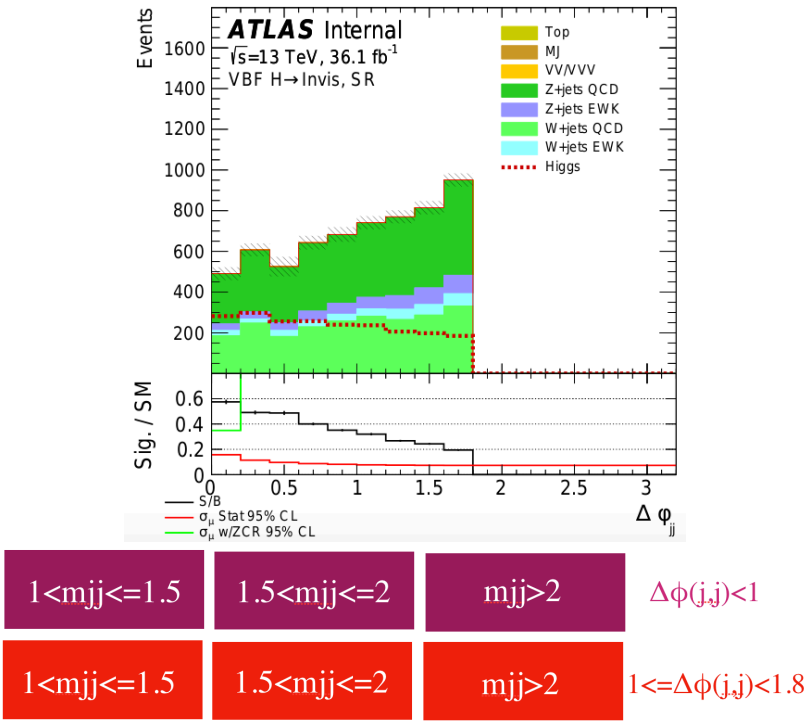

Figure 5.12: Signal and background distribution of $\Delta\Phi_{jj}$ and the 6-bin binning scheme illustration.

only fit (see Section 4.6) with different binning schemes including statistics uncertainty only and compared to the expected limit using just the 3 m_{jj} bins, i.e. 0.1785.

$\Delta\Phi_{jj}$ is a good candidate to bin in as the S/B drops down sharply as $\Delta\Phi_{jj}$ goes up as shown in Figure 5.12. We tried the 6-bin binning scheme illustrated in Figure 5.12 where we split the SR into two parts with $\Delta\Phi_{jj} < 1$ and $1 \leq \Delta\Phi_{jj} < 1.8$ and each part into 3 m_{jj} bins. Using Asimov only fit with statistics uncertainty only, we got an expected limit at 0.1674 (6% improvement compared to 0.1785). This is a significant improvement.

While loosening the number of jets requirement gives us more statistics, it is natural to bin in the number of jets as the S/B is very different between $N_{jet} = 2$ and $N_{jet} = 3, 4$ as shown in Figure 5.14. We ran two binning schemes in the fit demonstrated in Figure 5.14. On top of the three original m_{jj} bins with $N_{jet} = 2$, we either added one $N_{jet} > 2$ bin inclusive in m_{jj}, or $N_{jet} > 2$ split in three m_{jj} bins. The expected limit was 0.1700 (5% improvement) with one $N_{jet} > 2$ bin and 0.1760 (1% improvement) with three $N_{jet} > 2$

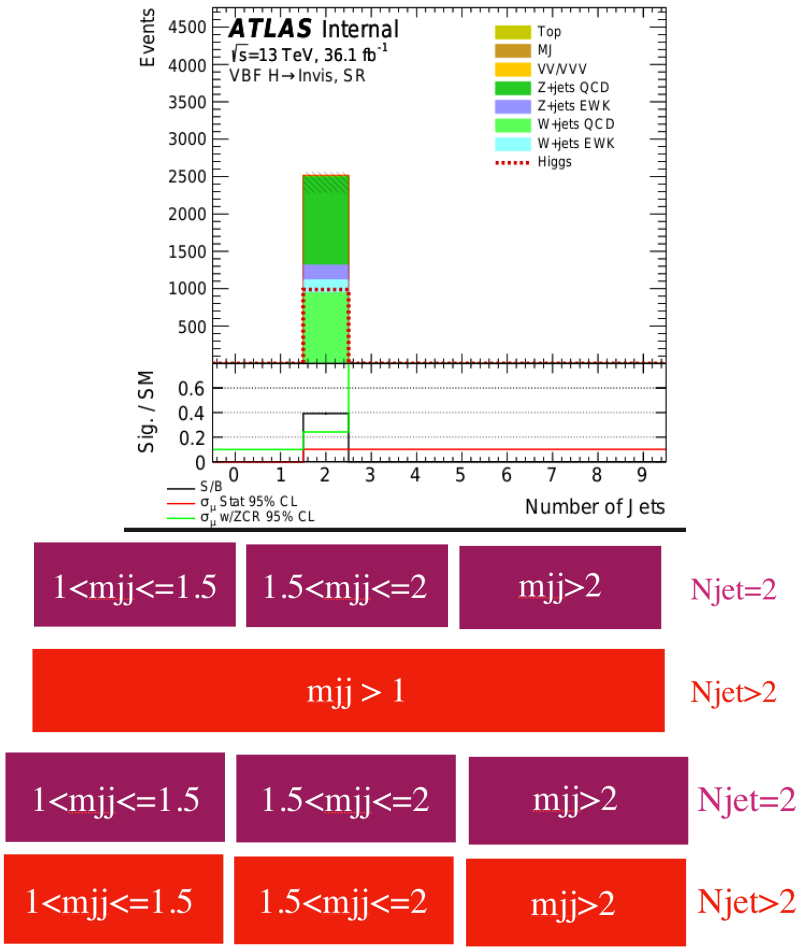

Figure 5.13: Signal and background distribution of number of jets and the illustration of the two binning schemes explored.

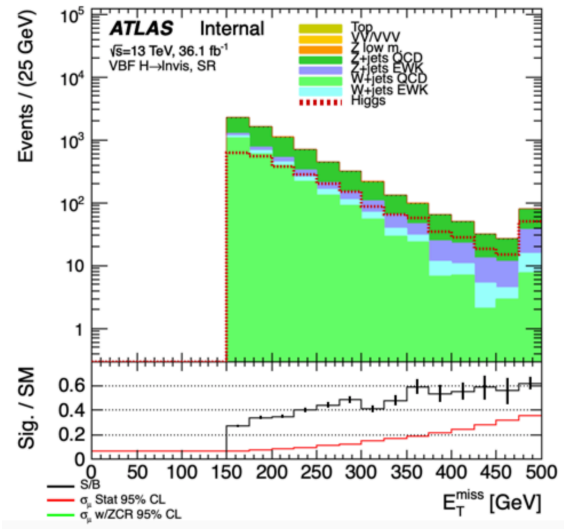

Figure 5.14: Signal and background distribution of $E_{\mathrm{T}}^{\mathrm{miss}}$.

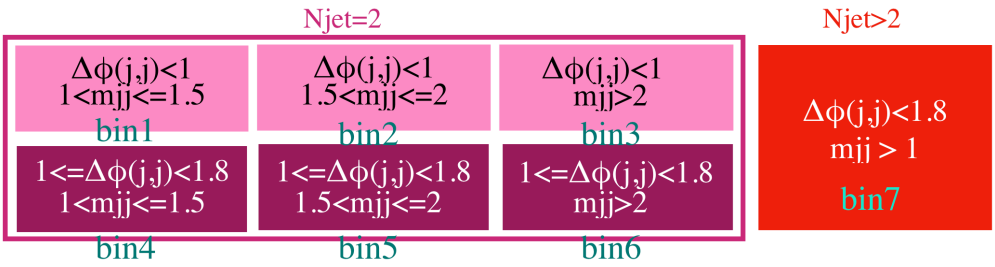

Figure 5.15: Final 7-bin binning scheme.

split in m_{jj} bins. It is expected that splitting the $N_{\mathrm{jet}} > 2$ bin into three m_{jj} bins does not improve sensitivity because data sample is small in $N_{\mathrm{jet}} > 2$ bin.

With the improved fJVT and new $E_{\mathrm{T}}^{\mathrm{miss}}$ Working Point, we were able to greatly reduce the QCD background and thus lowered the $E_{\mathrm{T}}^{\mathrm{miss}}$ cut to 150 GeV. Since the S/B is lower in the lower $E_{\mathrm{T}}^{\mathrm{miss}}$ region, we could gain by binning in $E_{\mathrm{T}}^{\mathrm{miss}}$. Similar to the binnings for N_{jet}, on top of the three original m_{jj} bins with $E_{\mathrm{T}}^{\mathrm{miss}} > 180$ GeV, we tried to add either one low $E_{\mathrm{T}}^{\mathrm{miss}}$ bin inclusive in m_{jj} or low $E_{\mathrm{T}}^{\mathrm{miss}}$ split in three m_{jj} bins. The expected limit was 0.1750 (2% improvement) with one low $E_{\mathrm{T}}^{\mathrm{miss}}$ bin and 0.1730 (3% improvement) with three low $E_{\mathrm{T}}^{\mathrm{miss}}$ bin split in m_{jj} bins. While there was a gain in sensitivity, compared to other binning schemes it seemed to be smaller. It was deemed not worth pursuing on top of other binning schemes because too many bins make the fitting procedure more time consuming.

Table 5.6: Summary of expected limit of all the binning schemes tried. Note all the limit except the last row was done without the reoptimized ZCR selection.

Binning Scheme	Expected Limit (Asimov, Stats Only)
Original 3 m_{jj} bins	0.1758
N_{jet} bin	0.1700
$N_{\mathrm{jet}} \times 3m_{\mathrm{jj}}$ bins	0.1760
Low $E_{\mathrm{T}}^{\mathrm{miss}}$ bin	0.1750
Low $E_{\mathrm{T}}^{\mathrm{miss}} \times 3m_{\mathrm{jj}}$ bins	0.1730
$\Delta\Phi_{\mathrm{jj}} \times 3m_{\mathrm{jj}}$ bins	0.1674
N_{jet} bin+$\Delta\Phi_{\mathrm{jj}} \times 3m_{\mathrm{jj}}$ bins+reoptimized ZCR	0.1594

Table 5.7: Table of the original 36.1 fb^{-1} selection and the updated selection for both SR and CR.

Requirement	Original	Reoptimized	
$e(\mu)$ Veto	$< 7(7)$ GeV	$< 4.5(4)$ GeV	
	Tight (Medium)	Loose (Very Loose)	
$e(\mu)$ CR	$> 30, 18$ GeV ($> 30, 7$ GeV)	$> 30, 7$ GeV	
	Tight (Medium)	Tight (Medium)	
	Single lepton trigger	Single, double lepton triggers	
Jet p_{T}	$> 80(50)$ GeV	$> 80(50)$GeV	
fJVT	–	< 0.5 if $E_{\mathrm{T}}^{\mathrm{miss}} > 180$ GeV else < 0.2	
$E_{\mathrm{T}}^{\mathrm{miss}}$	> 180 GeV	> 150 GeV	
	Loose	Tenacious	
MHT	> 150 GeV	> 120 GeV	
$E_{\mathrm{T}}^{\mathrm{miss}}$ soft term	–	< 20 GeV	
$\Delta\Phi_{\mathrm{j}E_{\mathrm{T}}^{\mathrm{miss}}}$	> 1.0	> 1.0	
$\Delta\eta_{\mathrm{jj}}$	> 4.8	> 3.8	
Njets	$= 2$ (3rd < 25 GeV)	$= 2$ (3rd < 25 GeV)	$2 - 4$ (5th < 25 GeV)
Max centrality	–	–	< 0.6
$\max(m_{\mathrm{j3,4j}}/m_{\mathrm{jj}})$	–	–	< 0.05
$\Delta\Phi_{\mathrm{jj}}$	< 1.8	< 1	$1 - 1.8$
m_{jj}	$1 - 1.15, 1.5 - 2, > 2$ TeV	$1 - 1.15, 1.5 - 2, > 2$ TeV	

Table 5.6 lists the expect limits of all the binning schemes we attempted. The best combination is a 7-bin configuration with 6 bins split into 3 regions in m_{jj} and 2 regions in $\Delta\Phi_{\mathrm{jj}}$ plus a $N_{\mathrm{jet}} > 2$ bin as shown in Figure 5.15. With the final 7-bin configuration and the reoptimized ZCR, we got an expected limit at 0.1594. This is 9% improvement to the original binning scheme. Including all the systematics, we got an 95% CL expected limit at 0.1985 with an Asimov only fit described in Section 4.6. Comparing to the Asimov only expected limit using the original 36.1 fb^{-1} selection in the new release (0.2639), we improved

Table 5.8: Table of the estimated multijet in each SR bin.

	bin 1	bin 2	bin 3	bin 4	bin 5	bin 6	bin 7
multijet events	30.0	13.5	12.0	23.0	12.0	12.0	5.0

Table 5.9: Table of the estimated multijet in each low $E_{\mathrm{T}}^{\mathrm{miss}}$ significance $W \to e\nu$ CR bin.

	bin 1	bin 2	bin 3	bin 4	bin 5	bin 6	bin 7
fake lepton events	10.4± 1.2	10.0± 1.9	5.25± 1.0	34.5± 8.3	14.2± 3.7	6.2± 1.5	5.3± 0.6

the result by 25%. Table 5.7 summarizes the final selection criteria.

5.3 Updates on Multijet and Fake Lepton Estimation

5.3.1 Multijet Background

We continued to use the rebalance and smear method to estimate the multijet background in the SR. Since proper rigorous treatment of the fJVT is still ongoing work, we estimate the number of multijet events before the fJVT requirement in SR and multiply the number with the fJVT efficiency. The fJVT efficiency is measured to be about 50% in a low $E_{\mathrm{T}}^{\mathrm{miss}}$ validation region which has the same jet selections as the SR with lower $E_{\mathrm{T}}^{\mathrm{miss}}$ values to measure the fJVT efficiency. The number of multijet events in each SR bin is listed in Table 5.8.

5.3.2 Fake Lepton

We use the same method to estimate the fake lepton background in the $W \to e\nu$ CR by dividing the $W \to e\nu$ CR into two parts based on $E_{\mathrm{T}}^{\mathrm{miss}}$ significance and estimate the fake events using loose but not tight electrons in MC.Table 5.9 shows the updated prefit values with the new selection.

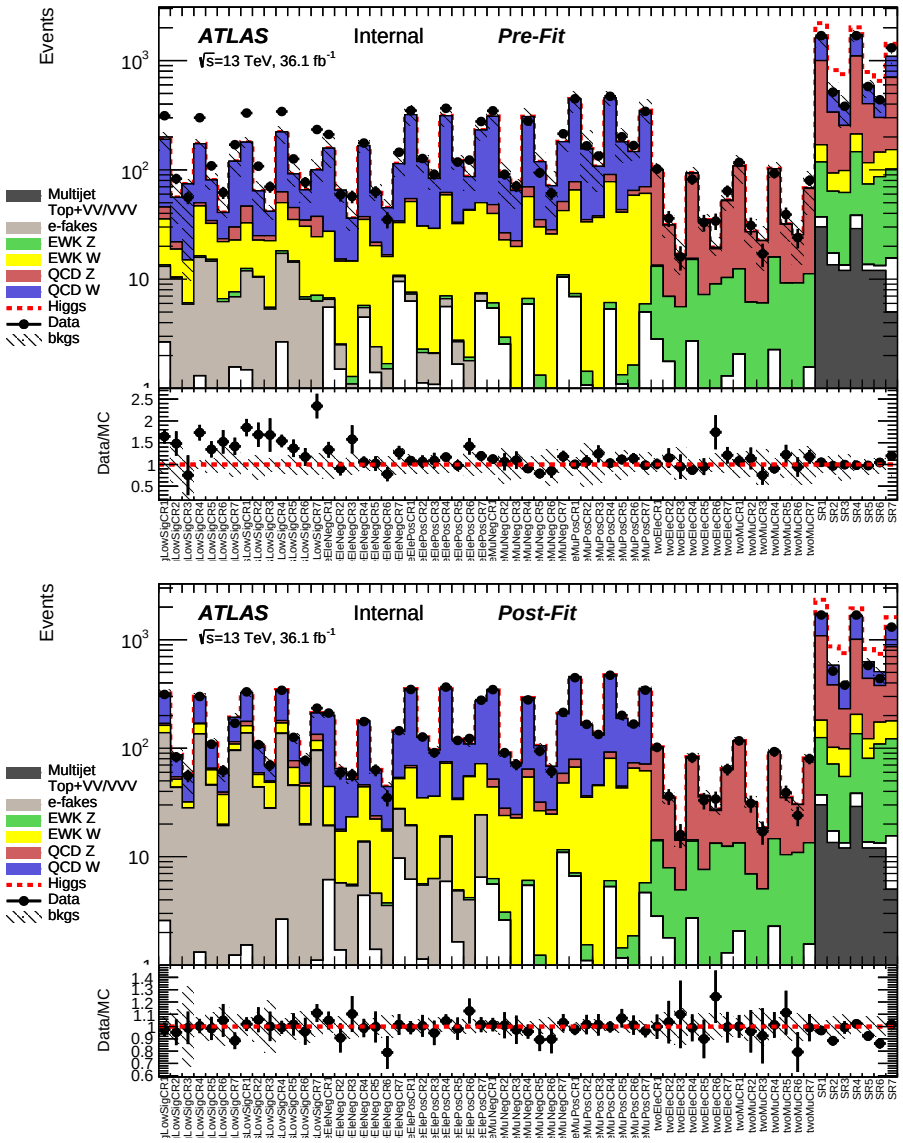

Figure 5.16: Prefit and postfit yields of each CR and SR with all systematics.

5.4 Results

Figure 5.16 shows the distribution of yields in each control region and signal region prefit and postfit. The fit model works as expected and no data excess is observed in the signal region.

Table 5.10: Expected and observed limits, calculated at the 95% C.L.

Expected	Observed	+1 σ	-1 σ	+2 σ	-2 σ
0.20	0.20	0.28	0.14	0.40	0.07

	bin 1	bin 2	bin 3	bin 4	bin 5	bin 6	bin 7
k_W	1.17 ± 0.24	1.09 ± 0.21	1.20 ± 0.24	1.08 ± 0.24	0.98 ± 0.21	1.19 ± 0.23	1.07 ± 0.31
k_Z	1.02 ± 0.24	0.88 ± 0.21	0.58 ± 0.17	0.94 ± 0.22	0.94 ± 0.23	0.97 ± 0.20	0.40 ± 0.10
β	10.55 ± 2.45	4.06 ± 1.13	4.31 ± 2.66	9.35 ± 1.52	3.03 ± 0.83	2.89 ± 1.43	17.78 ± 3.13

Table 5.11: The best fit values for kW (kZ)-normalization factors for W (Z), $\beta^{ele,fake}$ as the normalization factors for fake electrons in high $E_{\mathrm{T}}^{\mathrm{miss}}$ sig-$W(\rightarrow e^{\pm}\nu)$+jets control regions of 7 bins. This is done with the 36.1 fb^{-1} integrated luminosity using a simultaneous fit of the signal region and control region data.

As the result of the fit, the reoptimized analysis places an upper limit on the Higgs to invisible decays at 0.20 observed (0.20 expected). Table 5.10 shows the uncertainties of the fit. Table 5.11 shows the best fit values of the normalization factors for W and Z in the fit results.

To evaluate the impact of each category of systematic uncertainty, we make pull distribution and rankings of the nuisance parameters entering the fit to the Asimov data/real data in control regions and signal regions in Figure 5.17 and Figure 5.18. The nuisance parameters include the systematics uncertainties, statistics uncertainties and the transfer factors. Details of them and how they enter the fit can be found in Section 4.5 and Section 4.6. In this reoptimized analysis, we have 249 nuisance parameters in total. The distributions look reasonable and the rankings are very similar in both tables as expected.

In order to see the impact of certain group nuisance parameters, we remove groups of systematics from the limit calculation and recalculate the limit. The summary is shown in

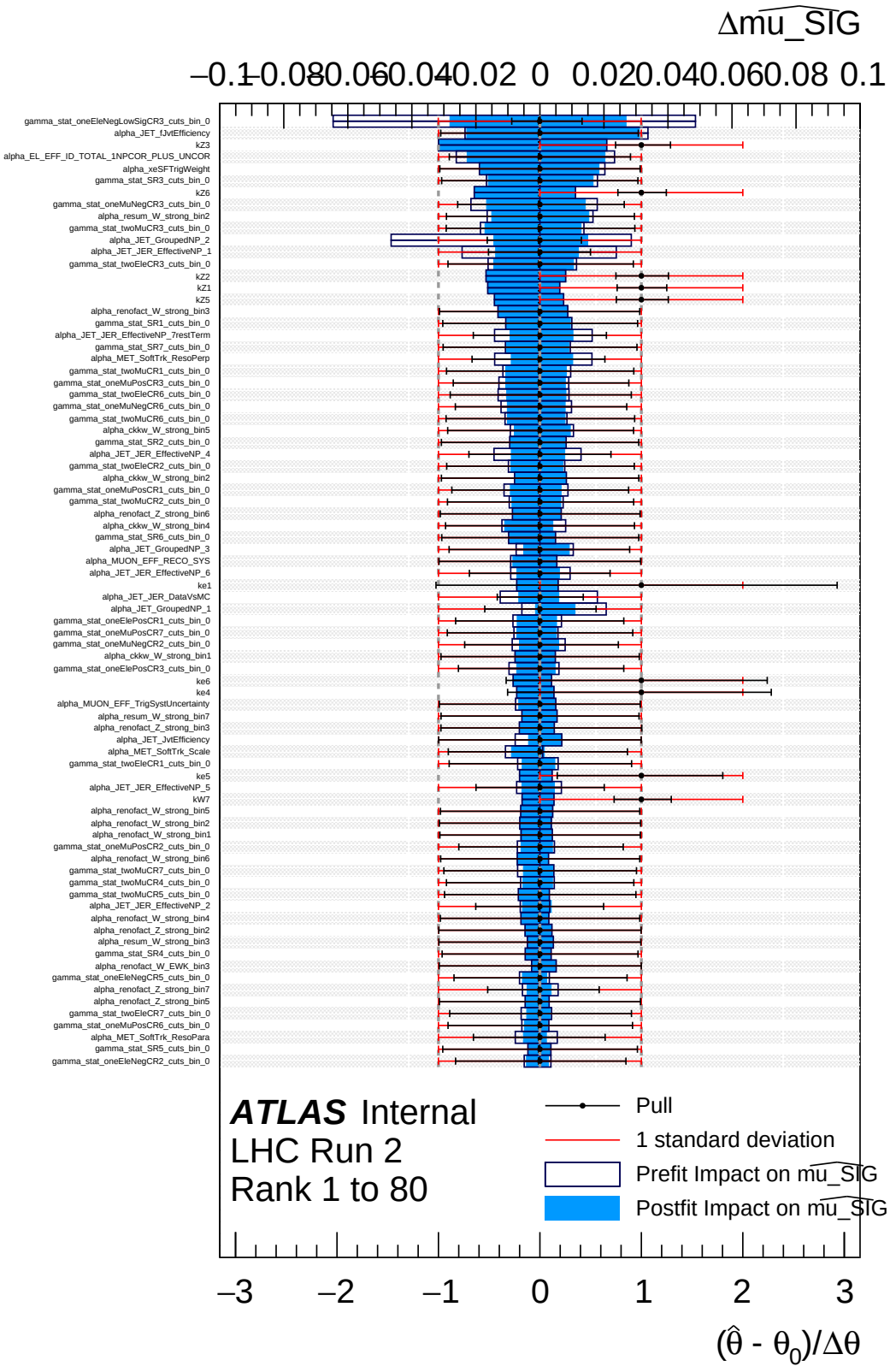

Figure 5.17: Pull distributions and rankings of nuisance parameters with Asimov only fit. Only the top 80 most impactful nuisance parameters are shown.

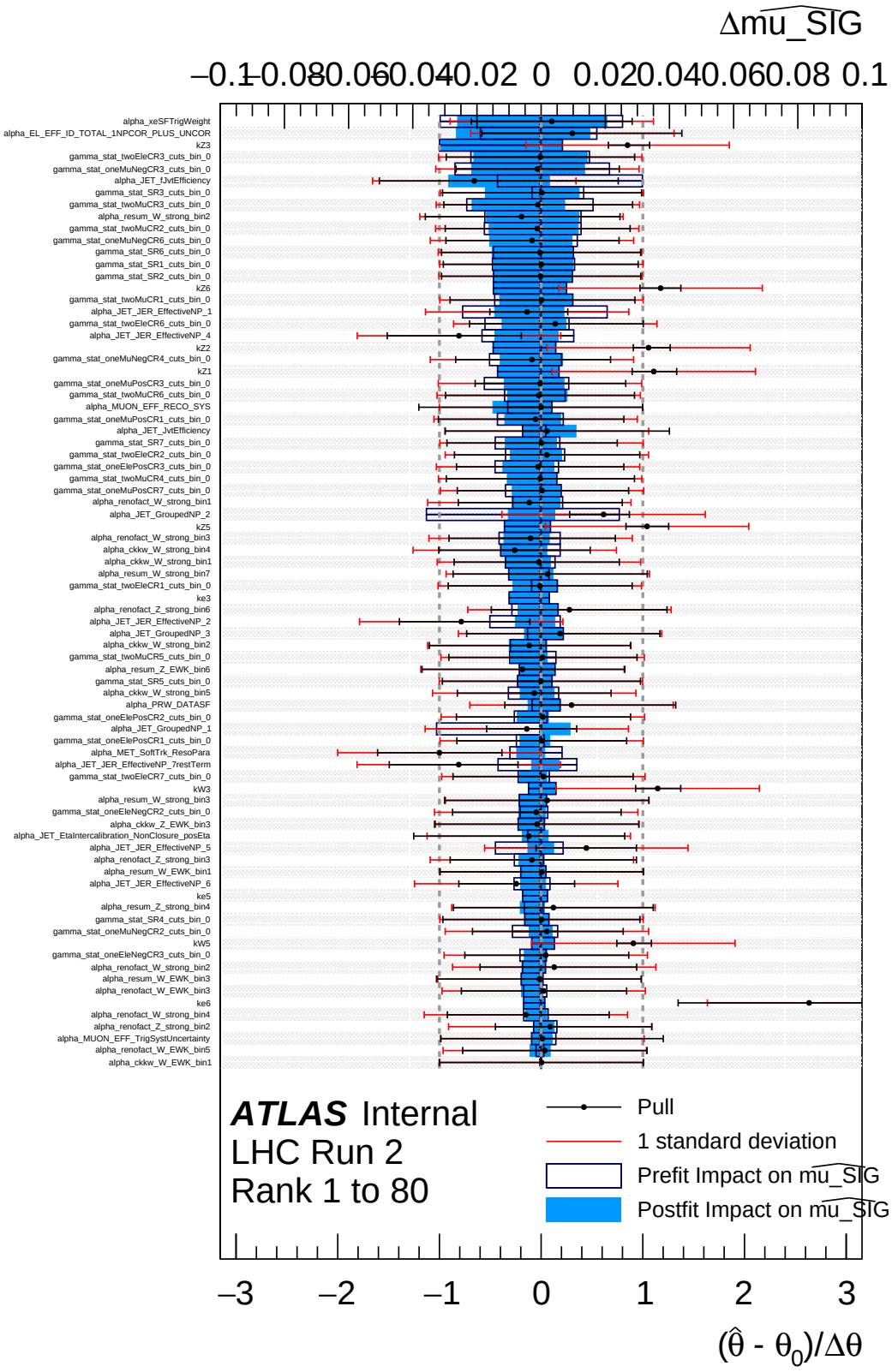

Figure 5.18: Pull distributions and rankings of nuisance parameters with the final unblinded fit. Only the top 80 most impactful nuisance parameters are shown.

Table 5.12: Variations in the expected limit as various groups of systematic uncertainties are turned off in the limit calculation. Note that experimental uncertainties and the uncertainty related to the size of the MC sample (MC stat.) are considered separate categories.

Group	Expected limit
Default	20.00%
No MC stat.	17.96%
No experimental	16.83%
No JES+JER	18.33%
No JER	19.84%
No (f)JVT	18.85%
No $E_{\mathrm{T}}^{\mathrm{miss}}$ SF	19.15%
No theory	18.27%
No systematic	15.27%
No systematic & no MC stat.	12.36%

Table 5.12. This gives a sense of where improvements can be made that will benefit the analysis, and which groups of uncertainties make a significant impact. Based on the table, it looks like experimental systematics and MC statistics are the leading constraints while improving theory systematics can also make a difference. Among experimental systematics, JVT systematics are now the leading constraint.

CHAPTER 6

CONCLUSIONS

The discovery of Higgs boson in 2012 confirmed a key piece of the Standard Model yet many questions remain unanswered such as the hierarchy problem why Higgs mass is found to be at 125 GeV, orders of magnitudes lower than the Plank mass. To answer such questions the second run of the LHC continued with a broad range of searches and precision measurements. VBF Higgs to invisible analysis continues to play a key role as it directly explores the relationship between the Higgs boson and Dark Matter particles.

This thesis gives an elaborate account of the original VBF Higgs to invisible analysis using the first part of the Run 2 dataset and a reoptimized analysis that improves the analysis by using the same set of data. While the original analysis served as a trial run following the standard analysis done in Run 1 with a few modifications to cope with the increasingly challenging LHC run conditions, the reoptimized analysis addressed many of the issues with higher pileup conditions. The original analysis set an upper limit on the Higgs to invisible branching ratio at 37% observed (28% expected), while the reoptimized analysis set a limit at 20% observed (20% expected).

As the sensitivity of this search starts to reach 20%, more theories start to become relevant. While there are plenty of opportunities for improvement for this search after data is taken, such as better vertex identification for VBF topology, improved fit method, detector improvements such as tracking in the forward region and a better trigger can also have a big impact. Tracking in the trigger often has a big impact on vertex finding, particle identification and background rejection but it is very CPU expensive to do on the full detector in software. A $E_{\mathrm{T}}^{\mathrm{miss}}$ trigger with full detector tracking, which can be enabled by the HLT tracking and vertex reconstruction, can further improve the sensitivity in Run 3 and beyond.

APPENDIX A

POSTFIT DISTRIBUTIONS

This chapter shows the postfit distribution in each control region and signal region in the analysis described in Chapter 4.

The dijet invariant mass (m_{jj}) and $E_{\mathrm{T}}^{\mathrm{miss}}$ (corrected by adding vectorially the lepton p_T) postfit distributions in each control region are shown in Figure A.1-A.6. The fake lepton estimates in $W \to e\nu$ control regions can't be shown since we only fit the yield and not the shape, which accounts for the excess in $W \to e\nu$ control regions.

The m_{jj} and $E_{\mathrm{T}}^{\mathrm{miss}}$ postfit distributions in each signal region is shown in Figure A.7.

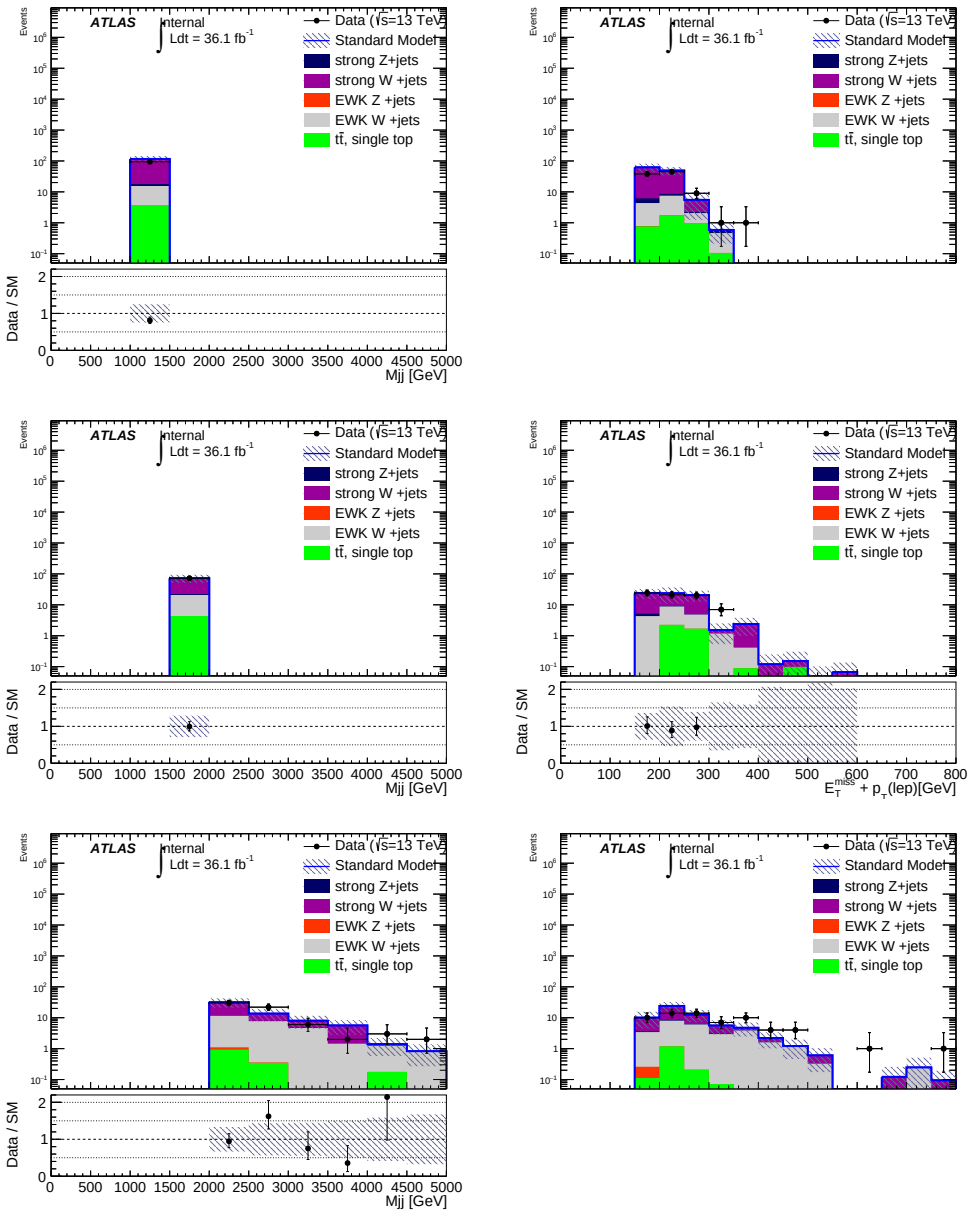

Figure A.1: Dijet invariant mass (m_{jj}) and $E_{\mathrm{T}}^{\mathrm{miss}}$ (corrected by adding vectorially the lepton p_T) post fit distributions for data and simulated events in the $W^- \to e^-\nu$ CRs. From the top to the bottom: the distributions from the first m_{jj} bin to the highest m_{jj} bin are shown.

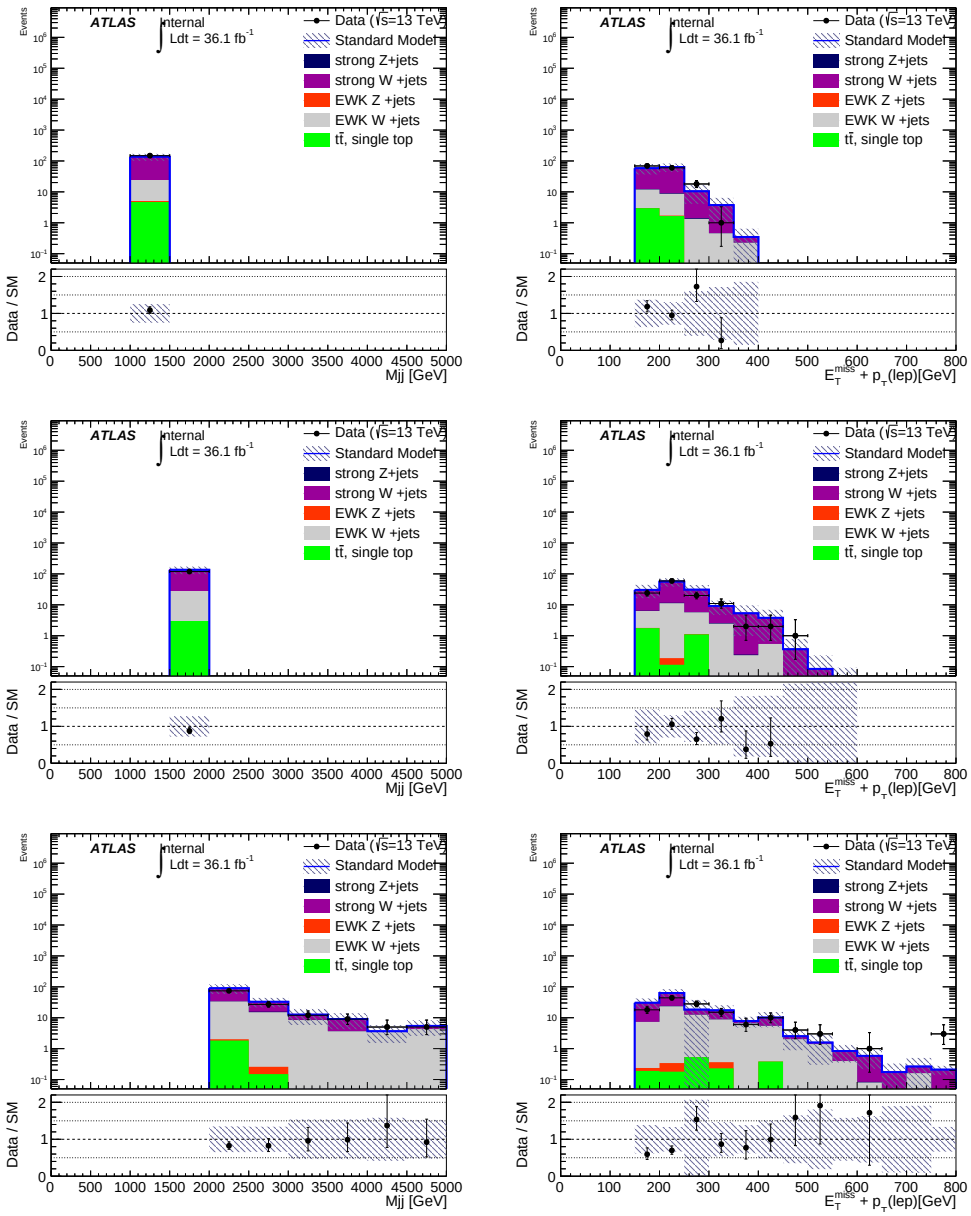

Figure A.2: Dijet invariant mass (m_{jj}) and $E_{\mathrm{T}}^{\mathrm{miss}}$ (corrected by adding vectorially the lepton p_T) post fit distributions for data and simulated events in the $W^+ \to e^+\nu$ CRs. From the top to the bottom: the distributions from the first m_{jj} bin to the highest m_{jj} bin are shown.

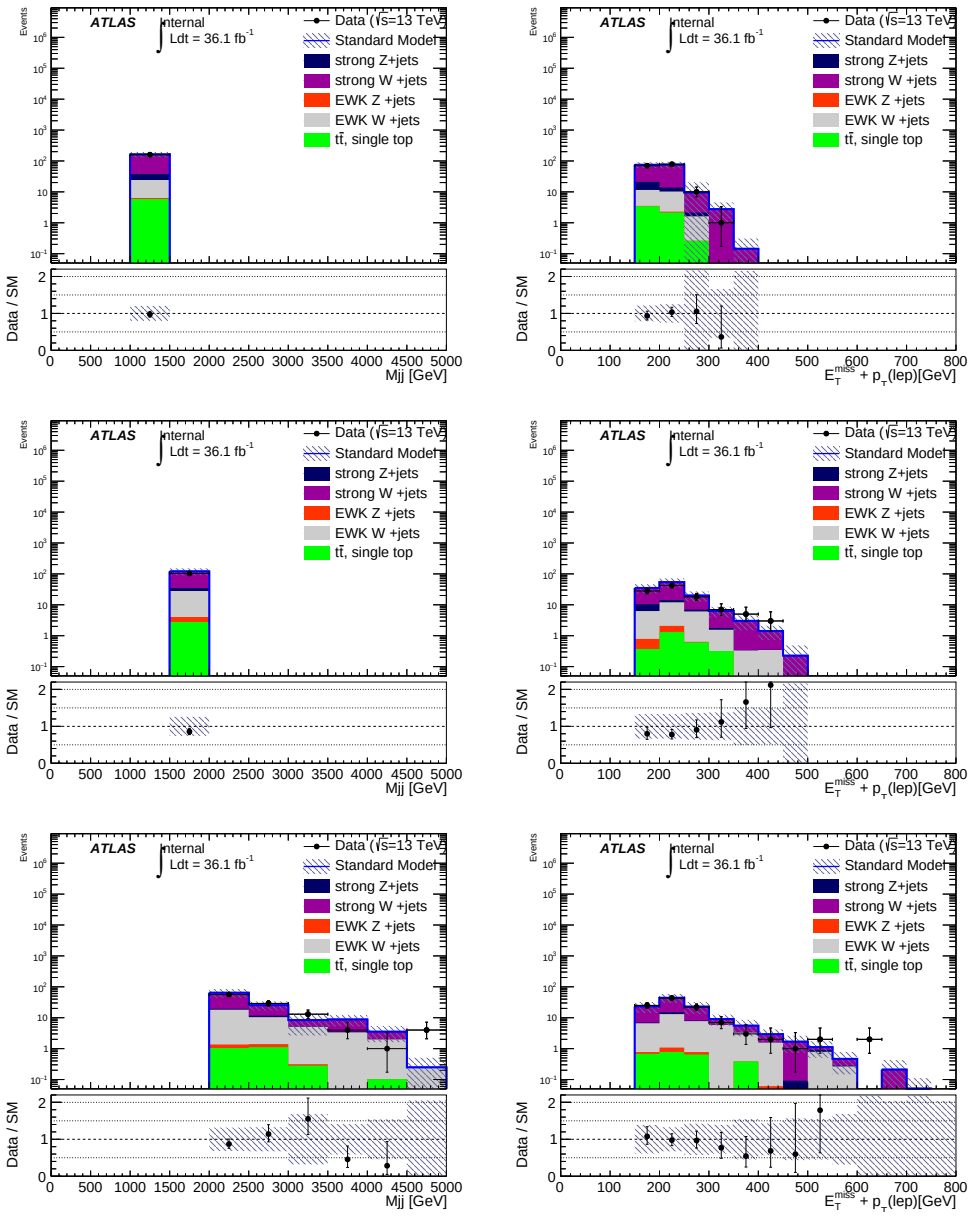

Figure A.3: Dijet invariant mass (m_{jj}) and $E_{\mathrm{T}}^{\mathrm{miss}}$ (corrected by adding vectorially the lepton p_T) post fit distributions for data and simulated events in the $W^- \to \mu^-\nu$ CRs. From the top to the bottom: the distributions from the first m_{jj} bin to the highest m_{jj} bin are shown.

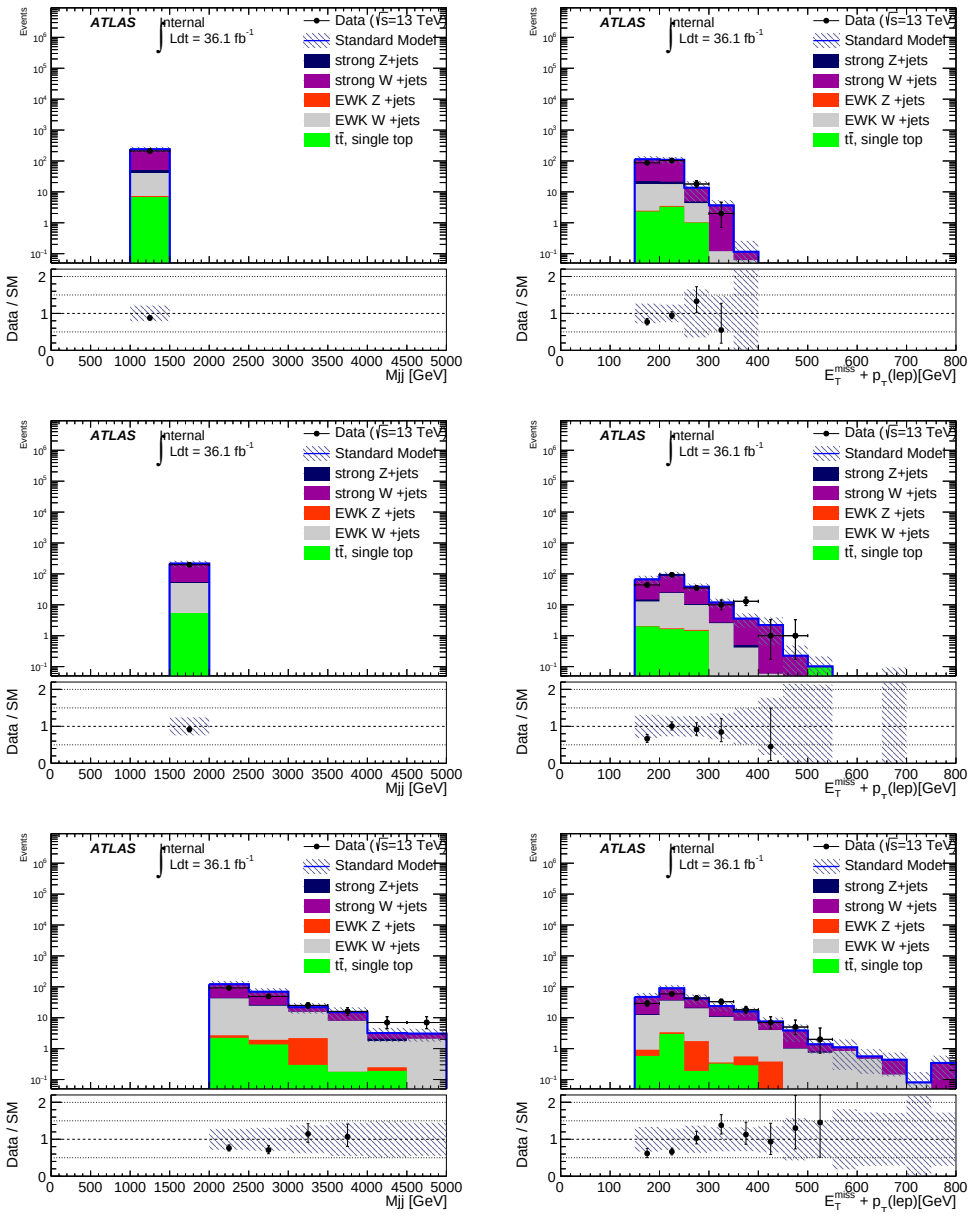

Figure A.4: Dijet invariant mass (m_{jj}) and $E_{\mathrm{T}}^{\mathrm{miss}}$ (corrected by adding vectorially the lepton p_T) post fit distributions for data and simulated events in the $W^+ \to \mu^+\nu$ CRs. From the top to the bottom: the distributions from the first m_{jj} bin to the highest m_{jj} bin are shown.

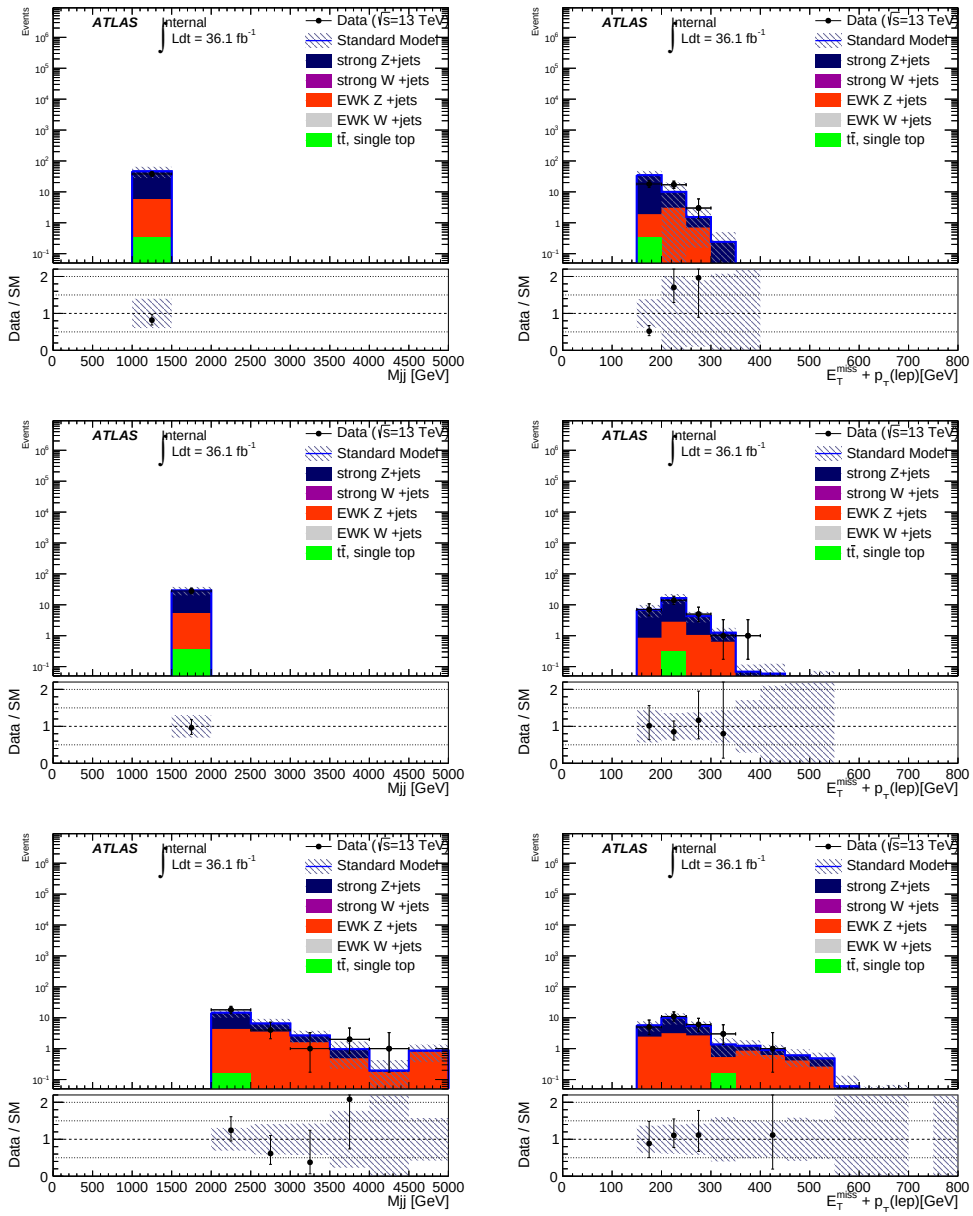

Figure A.5: Dijet invariant mass (m_{jj}) and $E_{\mathrm{T}}^{\mathrm{miss}}$ (corrected by adding vectorially the lepton p_T) post fit distributions for data and simulated events in the $Z \to \mu^+\mu^-$ CRs. From the top to the bottom: the distributions from the first m_{jj} bin to the highest m_{jj} bin are shown.

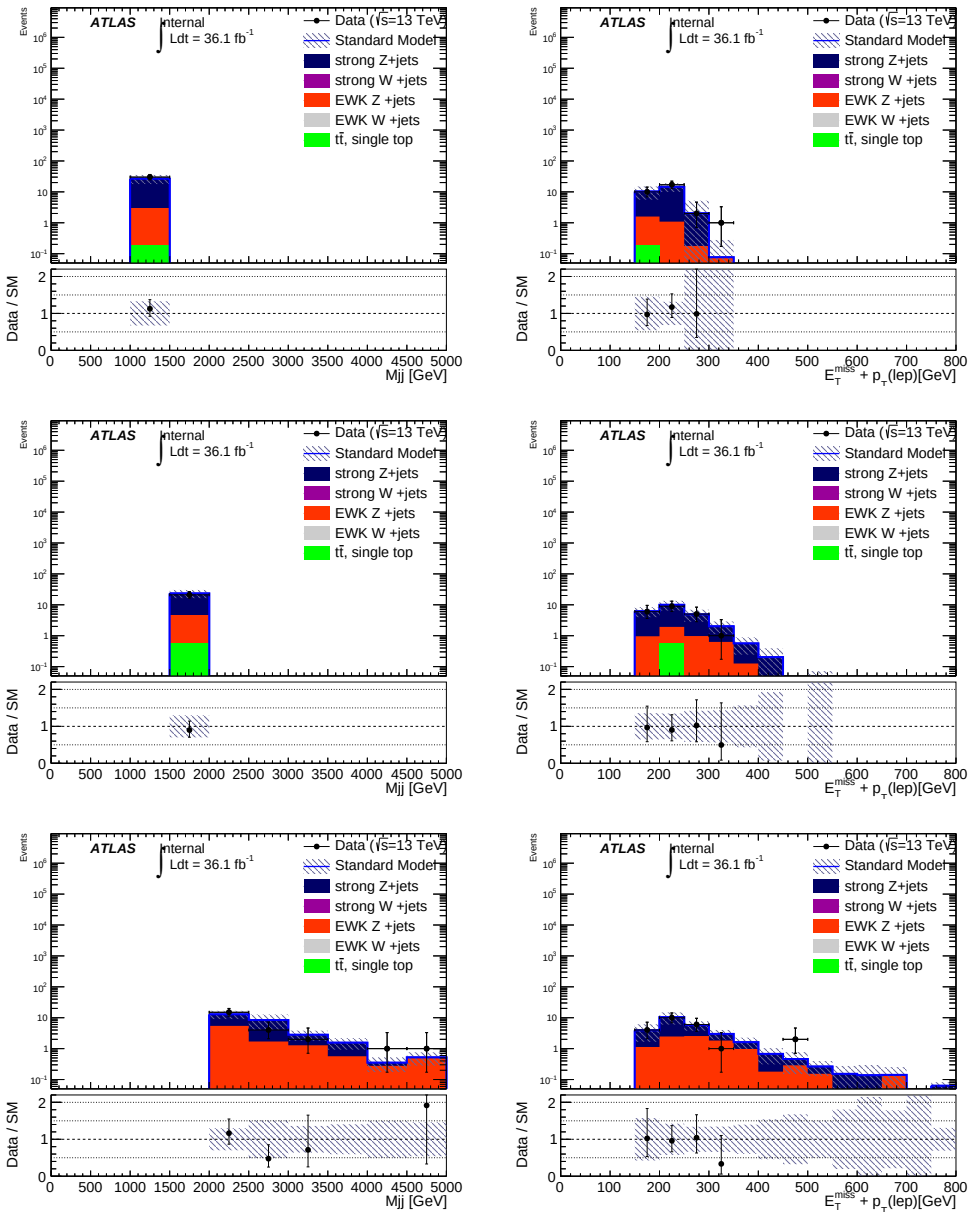

Figure A.6: Dijet invariant mass (m_{jj}) and $E_{\mathrm{T}}^{\mathrm{miss}}$ (corrected by adding vectorially the lepton p_T) post fit distributions for data and simulated events in the $Z \to e^+e^-$ CRs. From the top to the bottom: the distributions from the first m_{jj} bin to the highest m_{jj} bin are shown.

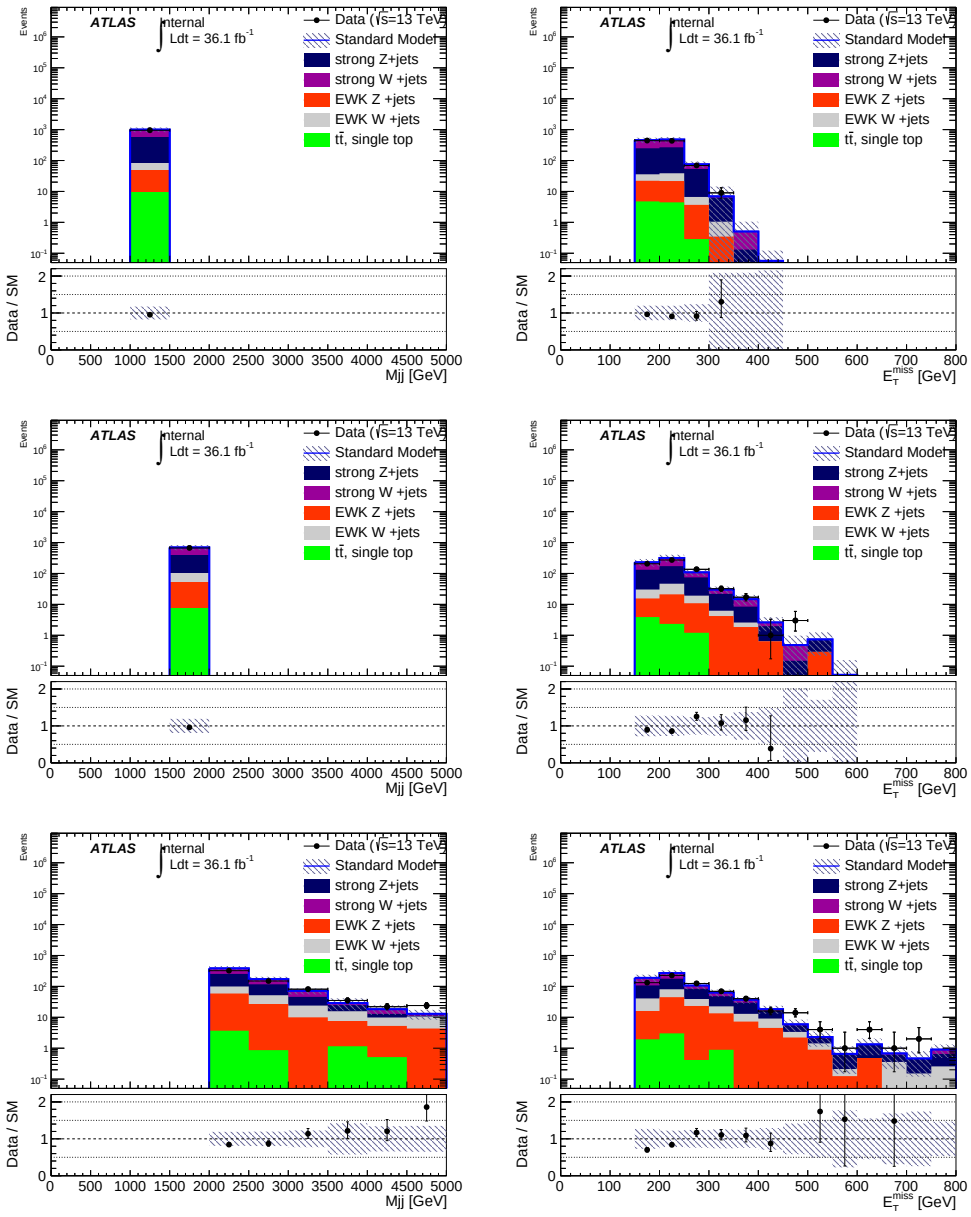

Figure A.7: Dijet invariant mass (m_{jj}) and $E_{\mathrm{T}}^{\mathrm{miss}}$ post fit distributions for data and simulated events in the signal region. From the top to the bottom: the distributions from the first m_{jj} bin to the highest m_{jj} bin are shown.

BIBLIOGRAPHY

[1] M. Aaboud et al. "Measurement of the Inelastic Proton-Proton Cross Section at $\sqrt{s} =$ 13 TeV with the ATLAS Detector at the LHC". In: *Phys. Rev. Lett.* 117.18 (2016), p. 182002. DOI: 10.1103/PhysRevLett.117.182002. arXiv: 1606.02625 [hep-ex].

[2] Georges Aad et al. "Muon reconstruction performance of the ATLAS detector in proton-proton collision data at $\sqrt{s}$ =13 TeV". In: *Eur. Phys. J.* C76.5 (2016), p. 292. DOI: 10.1140/epjc/s10052-016-4120-y. arXiv: 1603.05598 [hep-ex].

[3] D. S. Akerib et al. "Results from a search for dark matter in the complete LUX exposure". In: *Phys. Rev. Lett.* 118.2 (2017), p. 021303. DOI: 10.1103/PhysRevLett.118.021303. arXiv: 1608.07648 [astro-ph.CO].

[4] J. Alwall et al. "The automated computation of tree-level and next-to-leading order differential cross sections, and their matching to parton shower simulations". In: *JHEP* 07 (2014), p. 079. DOI: 10.1007/JHEP07(2014)079. arXiv: 1405.0301 [hep-ph].

[5] E. Aprile et al. "First Dark Matter Search Results from the XENON1T Experiment". In: *Phys. Rev. Lett.* 119.18 (2017), p. 181301. DOI: 10.1103/PhysRevLett.119.181301. arXiv: 1705.06655 [astro-ph.CO].

[6] ATLAS. "ATLAS Interal Twiki: signal systematic uncertainties". In: (). https://twiki.cern.ch/twiki/bin/view/AtlasProtected/PmgSystematicUncertaintyRecipes.

[7] ATLAS. "ATLAS Internal TWiki: Electron ID". In: (). https://twiki.cern.ch/twiki/bin/view/AtlasProtected/LatestRecommendationsElectronIDRun2.

[8] ATLAS. "ATLAS Internal TWiki: Jet calibration". In: (). https://twiki.cern.ch/twiki/bin/view/AtlasProtected/ApplyJetCalibration2016.

[9] ATLAS. "ATLAS Internal TWiki: Jet uncertainties". In: (). https://twiki.cern.ch/twiki/bin/view/AtlasProtected/JetUncertainties20152016Data20p7.

[10] ATLAS. "ATLAS Internal TWiki: Jet uncertainties". In: (). https://twiki.cern.ch/twiki/bin/viewauth/AtlasProtected/EtmissRecommendationsRel20p7.

[11] ATLAS. "ATLAS Internal TWiki: JVT". In: (). https://twiki.cern.ch/twiki/bin/view/AtlasProtected/JVTCalibration.

[12] ATLAS. "ATLAS Internal TWiki: MCPAnalysisGuidelines". In: (). http://cern.ch/go/k6lR.

[13] ATLAS. "ATLAS Internal TWiki: PRW". In: (). https://twiki.cern.ch/twiki/bin/view/AtlasProtected/ExtendedPileupReweighting.

[14] ATLAS. "HowToCleanJets2016". In: (). https://twiki.cern.ch/twiki/bin/view/AtlasProtected/HowToCleanJets2016.

[15] ATLAS. "NCB". In: (). https://twiki.cern.ch/twiki/bin/view/AtlasPublic/NonCollisionBackgroundPublicResults.

[16] ATLAS Collaboration. "Combined measurements of Higgs boson production and decay using up to 80 fb^{-1} of proton-proton collision data at $\sqrt{s} = 13$ TeV collected with the ATLAS experiment". In: *arXiv e-prints*, arXiv:1909.02845 (2019), arXiv:1909.02845. arXiv: 1909.02845 [hep-ex].

[17] ATLAS Collaboration. "Jet energy measurement and its systematic uncertainty in proton–proton collisions at $\sqrt{s} = 7$ TeV with the ATLAS detector". In: *Eur. Phys. J. C* 75 (2015), p. 17. DOI: 10.1140/epjc/s10052-014-3190-y. arXiv: 1406.0076 [hep-ex].

[18] ATLAS Collaboration. "Jet energy measurement with the ATLAS detector in proton–proton collisions at $\sqrt{s} = 7$ TeV". In: *Eur. Phys. J. C* 73 (2013), p. 2304. DOI: 10.1140/epjc/s10052-013-2304-2. arXiv: 1112.6426 [hep-ex].

[19] ATLAS Collaboration. "Observation and measurement of Higgs boson decays to WW^* with the ATLAS detector". In: *Phys. Rev.* D92.1 (2015), p. 012006. DOI: 10.1103/PhysRevD.92.012006. arXiv: 1412.2641 [hep-ex].

[20] ATLAS Collaboration. "Search for invisible decays of a Higgs boson using vector-boson fusion in *pp* collisions at $\sqrt{s} = 8$ TeV with the ATLAS detector". In: *JHEP* 01 (2016), p. 172. DOI: 10.1007/JHEP01(2016)172. arXiv: 1508.07869 [hep-ex].

[21] ATLAS Collaboration. "The ATLAS Experiment at the CERN Large Hadron Collider". In: *JINST* 3 (2008), S08003. DOI: 10.1088/1748-0221/3/08/S08003.

[22] *ATLAS inner detector: Technical Design Report, 1*. Technical Design Report ATLAS. Geneva: CERN, 1997. URL: https://cds.cern.ch/record/331063.

[23] "ATLAS inner detector: Technical design report. Vol. 2". In: (1997).

[24] *ATLAS liquid-argon calorimeter: Technical Design Report*. Technical Design Report ATLAS. Geneva: CERN, 1996. URL: https://cds.cern.ch/record/331061.

[25] "ATLAS muon spectrometer: Technical design report". In: (1997).

[26] *ATLAS tile calorimeter: Technical Design Report*. Technical Design Report ATLAS. Geneva: CERN, 1996. URL: https://cds.cern.ch/record/331062.

[27] Seungwon Baek, P. Ko, and Wan-Il Park. "Invisible Higgs Decay Width vs. Dark Matter Direct Detection Cross Section in Higgs Portal Dark Matter Models". In: *Phys. Rev.* D90.5 (2014), p. 055014. DOI: 10.1103/PhysRevD.90.055014. arXiv: 1405.3530 [hep-ph].

[28] R. D. Ball et al. "Parton distributions for the LHC Run II". In: *JHEP* 04 (2015), p. 040. DOI: 10.1007/JHEP04(2015)040. arXiv: 1410.8849 [hep-ph].

[29] Johannes Balz et al. *Search for new physics in final states with jets and missing transverse momentum using pp collision data collected in 2015 and 2016 by ATLAS*. Tech. rep. ATL-COM-PHYS-2016-1487. Geneva: CERN, 2016. URL: https://cds.cern.ch/record/2225958.

[30] William Buttinger. "Using Event Weights to account for differences in Instantaneous Luminosity and Trigger Prescale in Monte Carlo and Data". In: ATL-COM-SOFT-2015-119 (2015). URL: https://cds.cern.ch/record/2014726.

[31] M. Cacciari, G. P. Salam, and G. Soyez. "The anti-k_t jet clustering algorithm". In: *JHEP* 04 (2008), p. 063. DOI: 10.1088/1126-6708/2008/04/063. arXiv: 0802.1189 [hep-ph].

[32] J. M. Campbell, R. K. Ellis, and C. Williams. "Vector boson pair production at the LHC". In: *JHEP* 07 (2011), p. 018. DOI: 10.1007/JHEP07(2011)018. arXiv: 1105.0020 [hep-ph].

[33] Fabio Cascioli, Philipp Maierhofer, and Stefano Pozzorini. "Scattering Amplitudes with Open Loops". In: *Phys. Rev. Lett.* 108 (2012), p. 111601. DOI: 10.1103/PhysRevLett.108.111601. arXiv: 1111.5206 [hep-ph].

[34] Serguei Chatrchyan et al. "Search for invisible decays of Higgs bosons in the vector boson fusion and associated ZH production modes". In: *Eur. Phys. J.* C74 (2014), p. 2980. DOI: 10.1140/epjc/s10052-014-2980-6. arXiv: 1404.1344 [hep-ex].

[35] Douglas Clowe et al. "A Direct Empirical Proof of the Existence of Dark Matter". In: 648.2 (2006), pp. L109–L113. DOI: 10.1086/508162. arXiv: astro-ph/0608407 [astro-ph].

[36] CMS Collaboration. "Searches for invisible decays of the Higgs boson in pp collisions at $\sqrt{s} = 7$, 8, and 13 TeV". In: (2016). arXiv: 1610.09218 [hep-ex].

[37] ATLAS Collaboration. "Search for Invisible Decays of a Higgs Boson Produced in Association with a Z Boson in ATLAS". In: 112.20, 201802 (2014), p. 201802. DOI: 10.1103/PhysRevLett.112.201802. arXiv: 1402.3244 [hep-ex].

[38] ATLAS collaboration. "Search for invisible Higgs boson decays in vector boson fusion at $\sqrt{\{ \text{ s } \}} = 13$TeV with the ATLAS detector". In: *Physics Letters B* 793 (2019), pp. 499–519. DOI: 10.1016/j.physletb.2019.04.024. arXiv: 1809.06682 [hep-ex].

[39] Xiangyi Cui et al. “Dark Matter Results From 54-Ton-Day Exposure of PandaX-II Experiment”. In: *Phys. Rev. Lett.* 119.18 (2017), p. 181302. DOI: 10.1103/PhysRevLett.119.181302. arXiv: 1708.06917 [astro-ph.CO].

[40] D. de Florian et al. “Handbook of LHC Higgs Cross Sections: 4. Deciphering the Nature of the Higgs Sector”. In: (2016). arXiv: 1610.07922 [hep-ph].

[41] A. Denner et al. “HAWK 2.0: A Monte Carlo program for Higgs production in vector-boson fusion and Higgs strahlung at hadron colliders”. In: *Comput. Phys. Commun.* 195 (2015), pp. 161–171. DOI: 10.1016/j.cpc.2015.04.021. arXiv: 1412.5390 [hep-ph].

[42] Abdelhak Djouadi et al. “Implications of LHC searches for Higgs-portal dark matter”. In: *Physics Letters B* 709.1 (2012), pp. 65–69. DOI: 10.1016/j.physletb.2012.01.062. arXiv: 1112.3299 [hep-ph].

[43] F. Englert and R. Brout. “Broken Symmetry and the Mass of Gauge Vector Mesons”. In: *Phys. Rev. Lett.* 13 (9 1964), pp. 321–323. DOI: 10.1103/PhysRevLett.13.321. URL: https://link.aps.org/doi/10.1103/PhysRevLett.13.321.

[44] Lyndon Evans and Philip Bryant. “LHC Machine”. In: *Journal of Instrumentation* 3.08 (2008), S08001–S08001. DOI: 10.1088/1748-0221/3/08/s08001. URL: https://doi.org/10.1088%2F1748-0221%2F3%2F08%2Fs08001.

[45] T. Gleisberg et al. “Event generation with SHERPA 1.1”. In: *JHEP* 02 (2009), p. 007. DOI: 10.1088/1126-6708/2009/02/007. arXiv: 0811.4622 [hep-ph].

[46] Tanju Gleisberg and Stefan Höche. “Comix, a new matrix element generator”. In: *JHEP* 12 (2008), p. 039. DOI: 10.1088/1126-6708/2008/12/039. arXiv: 0808.3674 [hep-ph].

[47] P.W. Higgs. “Broken symmetries, massless particles and gauge fields”. In: *Physics Letters* 12.2 (1964), pp. 132 –133. ISSN: 0031-9163. DOI: https://doi.org/10.1016/

0031-9163(64)91136-9. URL: http://www.sciencedirect.com/science/article/pii/0031916364911369.

[48] Stefan Höche et al. "QCD matrix elements + parton showers: The NLO case". In: *JHEP* 04 (2013), p. 027. DOI: 10.1007/JHEP04(2013)027. arXiv: 1207.5030 [hep-ph].

[49] Peter Langacker. *The Standard Model and Beyond*. Taylor & Francis, Boca Raton, 2010.

[50] *LEP design report*. Copies shelved as reports in LEP, PS and SPS libraries. Geneva: CERN, 1984. URL: http://cds.cern.ch/record/102083.

[51] T Linnecar et al. *Hardware and Initial Beam Commissioning of the LHC RF Systems*. Tech. rep. LHC-PROJECT-Report-1172. CERN-LHC-PROJECT-Report-1172. Geneva: CERN, 2008. URL: https://cds.cern.ch/record/1176380.

[52] Priyamvada Natarajan et al. "Mapping substructure in the HST Frontier Fields cluster lenses and in cosmological simulations". In: 468.2 (2017), pp. 1962–1980. DOI: 10.1093/mnras/stw3385. arXiv: 1702.04348 [astro-ph.GA].

[53] Massimo Persic, Paolo Salucci, and Fulvio Stel. "The universal rotation curve of spiral galaxies - I. The dark matter connection". In: 281.1 (1996), pp. 27–47. DOI: 10.1093/mnras/281.1.27. arXiv: astro-ph/9506004 [astro-ph].

[54] Michael Edward Peskin. *An Introduction to Quantum Field Theory*. Avalon Publishing, 1995. ISBN: 978-0813350196.

[55] Thomas Sven Pettersson and P Lef vre. *The Large Hadron Collider: conceptual design*. Tech. rep. CERN-AC-95-05-LHC. 1995. URL: https://cds.cern.ch/record/291782.

[56] LHC Yellow report. "SM Higgs production cross sections at 13 TeV, Report 4". In: (). https://twiki.cern.ch/twiki/bin/view/LHCPhysics/CERNYellowReportPageAt13TeV.

[57] Steffen Schumann and Frank Krauss. "A Parton shower algorithm based on Catani-Seymour dipole factorisation". In: *JHEP* 03 (2008), p. 038. DOI: 10.1088/1126-6708/2008/03/038. arXiv: 0709.1027 [hep-ph].

[58] "Selection of jets produced in 13TeV proton-proton collisions with the ATLAS detector". In: ATLAS-CONF-2015-029 (2015). URL: https://cds.cern.ch/record/2037702.

[59] Torbjorn Sjöstrand, Stephen Mrenna, and Peter Z. Skands. "A Brief Introduction to PYTHIA 8.1". In: *Comput. Phys. Commun.* 178 (2008), p. 852. DOI: 10.1016/j.cpc.2008.01.036. arXiv: 0710.3820 [hep-ph].

[60] Iain W. Stewart and Frank J. Tackmann. "Theory uncertainties for Higgs mass and other searches using jet bins". In: 85.3, 034011 (2012), p. 034011. DOI: 10.1103/PhysRevD.85.034011. arXiv: 1107.2117 [hep-ph].

[61] Xiang-Ping Wu et al. "A comparison of different cluster mass estimates: consistency or discrepancy?" In: 301.3 (1998), pp. 861–871. DOI: 10.1046/j.1365-8711.1998.02055.x. arXiv: astro-ph/9808179 [astro-ph].